

Light Trapping in Monocrystalline Silicon Solar Cells Using Random Upright Pyramids

by

Salman Manzoor

A Thesis Presented in Partial Fulfillment  
of the Requirements for the Degree  
Master of Science

Approved July 2014 by the  
Graduate Supervisory Committee:

Zachary Holman, Chair  
Stephen Goodnick  
Stuart Bowden

ARIZONA STATE UNIVERSITY

August 2014

## ABSTRACT

Crystalline silicon has a relatively low absorption coefficient, and therefore, in thin silicon solar cells surface texturization plays a vital role in enhancing light absorption. Texturization is needed to increase the path length of light through the active absorbing layer. The most popular choice for surface texturization of crystalline silicon is the anisotropic wet-etching that yields pyramid-like structures. These structures have shown to be both simple to fabricate and efficient in increasing the path length; they outperform most competing surface texture. Recent studies have also shown these pyramid-like structures are not truly square-based  $54.7^\circ$  pyramids but have variable base angles and shapes. In addition, their distribution is not regular -- as is often assumed in optical models -- but random. For accurate prediction of performance of silicon solar cells, it is important to investigate the true nature of the surface texture that is achieved using anisotropic wet-etching, and its impact on light trapping. We have used atomic force microscopy (AFM) to characterize the surface topology by obtaining actual height maps that serve as input to ray tracing software. The height map also yields the base angle distribution, which is compared to the base angle distribution obtained by analyzing the angular reflectance distribution measured by spectrophotometer to validate the shape of the structures. Further validation of the measured AFM maps is done by performing pyramid density comparison with SEM micrograph of the texture. Last method employed for validation is Focused Ion Beam (FIB) that is used to mill the long section of pyramids to reveal their profile and so from that the base angle distribution is measured. After that the measured map is modified and the maps are generated keeping the positional randomness (the positions of pyramids) and height of the pyramids the same, but changing their base angles. In the end a ray tracing software is used to compare the actual measured AFM map and also the modified

maps using their reflectance, transmittance, angular scattering and most importantly path length enhancement, absorbance and short circuit current with lambertian scatterer.

## DEDICATION

I dedicate my work to my parents, Manzoor Masih and Mussarat and to my sisters Mahwash, Sheryl and Faryal. I thank them for their continued support and encouragement throughout my life. I also dedicate my work to my late grandmother whose hard work and persistence has enabled me today to be in this position.

## ACKNOWLEDGMENTS

I would like to acknowledge and thank Dr. Holman for his support and helpful discussions. He has always been very patient and encouraging. I am also grateful to my thesis committee members for their help. I also want to acknowledge the help from Kenneth Mossman for teaching me how to use AFM and FIB. Next I would like to thank Dr. Miha Filipic who has been very kind to do the optical simulation for this work. Furthermore, I would thank Justin Smith for his helpful discussion on how to modify the measured AFM map.

## TABLE OF CONTENTS

	Page
LIST OF TABLES.....	vii
LIST OF FIGURES.....	viii
CHAPTER	
1 INTRODUCTION .....	1
1.1 Energy Landscape and Photovoltaic .....	1
1.2 Silicon As Material for Solar Cell Applications .....	6
1.3 Aim of Thesis .....	12
2 CHARACTERIZATION OF FRONT SURFACE LIGHT TRAPPING .....	15
2.1 Benefits of Light Trapping .....	15
2.2 Lambertian Surface and Yablonovitch limit .....	17
2.3 Modelling and Simulation.....	19
2.3.1 Path Length Enhancement Simulation .....	21
2.3.2 Front Surface Reflectance Simulation .....	23
2.4 Experimental Front Surface Reflectance Characterization .....	27
2.4.1 Angular Resolved Scattering using Spectrophotometer	28
2.4.2 2D Reflection Distribution using Photographic Film.....	30
3 ATOMIC FORCE MICROSCOPY (AFM).....	33
3.1 Main Components of AFM Machine .....	33
3.2 Modes of Operation .....	36
3.2.1 Static Mode .....	37
3.2.1 Dynamic Mode .....	38
3.3 Comparison of Contact, Tapping and Non-Contact Mode .....	39
3.4 Mode selection for topographical imaging of Silicon .....	41
3.5 Common Artefacts in AFM Scans .....	43

CHAPTER	Page
3.5.1 Probe/Tip Artefacts.....	43
3.6 Types of Probes .....	46
4 EXPERIMENTATION AND RESULTS.....	47
4.1 Probe/Tip Selection .....	47
4.2 Calibration of AFM.....	48
4.2.1 Height Calibration .....	49
4.2.2 Large Angle Measurement.....	51
4.3 AFM Measurement of Actual Textured Silicon Wafer .....	52
4.3.1 Validation of Measured AFM Map .....	58
4.4 Manipulation of Measured AFM Map .....	68
4.4.1 Roughness Comparison of the Maps .....	77
4.5 Optical Simulations .....	79
4.5.1 Effect of Map Area on Front Surface Reflectance .....	79
4.5.2 Effect of Changing Base Angles on Reflectance, Transmittance and Absorbance of the Maps .....	80
4.5.3 Front Surface Reflectance Comparison – CROWM Versus OPAL2 .....	84
4.5.4 Angular Transmittance Scattering Results .....	86
4.5.5 Comparison With Lamertian Scatterer .....	88
5 CONCLUSION.....	98
5.1 Summary.....	98
5.2 Future Work .....	100
REFERENCES.....	101
APPENDIX	
A MAPS USED IN THIS WORK .....	105

## LIST OF TABLES

Table	Page
1. Comparison of Contact, Tapping and Non-Contact Modes .....	39
2. Validation of AFM Maps by Calculating Density of Peaks .....	57
3. List and Description of Maps.....	68
4. Evaluation of Roughness of the Maps. ....	77
5. Difference in Reflectance values at 900nm, CROWM Versus OPAL2. ....	84
6. Path Length Enhancement Results from CROWM... ..	91
7. Short Circuit Current Values .....	97

## LIST OF FIGURES

Figure		Page
1.	World Energy Consumption Trend [1] .....	1
2.	Growth Trend Within Renewable Energy Sources [2] .....	2
3.	PV Production Development by Technology in Germany [4].....	3
4.	Electricity Generation by Fuel [2] .....	4
5.	Cost of PV Module by its Elements [5].....	5
6.	Solar Spectrum [6] .....	7
7.	Plot of Detailed Balance Equation .....	8
8.	Indirect Transition with Phonon Absorption and Phonon Emission .....	9
9.	Absorption Curves of Popular Solar Cell Materials .....	11
10.	Illustration Showing Base Angle of Pyramid .....	13
11.	Effect of Texturing Si Wafer .....	15
12.	Lambertian Surface .....	17
13.	Example of Ray Tracing using Monte Carlo Simulation .....	20
14.	Setup for Path Length Enhancement Simulations .....	21
15.	Percentage of Rays Remaining Versus the Passes Through Cell [10]..	22
16.	Shows Path Length Enhancement Versus Facet Angle (right) Shows Standard Deviation in Path Length Enhancement Versus Facet Angle	23
17.	Random Upright Pyramidal Texture Creation [16] .....	25
18.	Preferential Paths for Regular Upright and Inverted Pyramids [16] ....	26
19.	A Layout of Spectrophotometer with Integrating Sphere .....	27
20.	Angular Resolved Scattering Measurement Arrangement.....	28
21.	(a) ARS Measurement for Random Upright Pyramids Textured with Two Different Chemicals .....	30
22.	Optical Setup for Obtaining 2D Reflection Distribution [23].....	31

Figure	Page
23. 2D Reflection Distribution from Front Surface for Inverted Pyramid .	31
24. Typical AFM Machine [25] .....	34
25. Light Lever Method for Cantilever Deflection Detection [26] .....	35
26. Forces Between Tip and Surface with Respect to Distance and Different Modes [27] .....	36
27. Amplitude and Frequency Modulation [26] .....	39
28. Contact and Tapping Mode Images for the Same (100) Silicon Epitaxial Wafer [29] .....	42
29. A) Shows That Features Dilate when Tip is not Sharp B) Shows That Features Appear Small When Tip Doesn't have High Aspect Ratio [30]	44
30. Effect of Aspect-Ratio and Radius of Curvature on the Profile [31]....	45
31. AFM Scan of a DBA Showing Repetition of each Feature [30].....	46
32. AR10T-NCHR High Aspect Ratio Tip used in this Work [32].....	48
33. Z-Height Calibration Standards [34] .....	49
34. Section of TGZ4 Showing the Step Height = 1395 .....	49
35. Section of TGZ3 Showing Step Height = 553 .....	50
36. Section of TGZ4 Showing Angle of the side of the Step .....	51
37. SEM Image of the Textured Silicon Wafer used in this Work .....	52
38. (top) Shows a Small Area Scan, (bottom) Shows Large Area Scan of a Different Location .....	54
39. Measured AFM Maps (top) is Map 1 with Area of 10-by-10 Square Microns, (bottom) is Map 2 and its Area is 20-by-20 Square Microns	55
40. (top) Graph Shows the Comparison of Height Distribution, (bottom) Graph Shows the Comparison of Base Angle Distribution .....	56

Figure	Page
41. Angle Comparison of Pyramid Facets .....	57
42. Density of Peaks Comparison .....	59
43. Angular Resolved Scattering Distribution from Front Surface .....	60
44. Eucentric Tilting .....	62
45. FIB Ion Image, Platinum Deposition and Milling .....	62
46. SEM Micrograph after Milling .....	63
47. SEM Micrograph of the Cross Section at High Magnification .....	64
48. Detected Profiles in the SEM Micrographs shown in Fig. 46 .....	65
49. Dominant Angle shown as an Example from Profiles from Fig. 47 ...	66
50. Shows Base Angle Distribution Calculated with FIB Versus AFM .....	67
51. Process for Making Bigger Maps Starting from Small Map .....	71
52. Angular Distribution of Base Angle for Fixed Angle Maps .....	72
53. Angular Distribution of Base Angle for All the Big Maps .....	73
54. Measured AFM Map and Modified Fixed Angle Maps .....	74
55. Modified Fixed Angle Maps with Increased Area .....	75
56. Modified Maps with Normally Distributed Base Angle Distribution ...	76
57. Total Reflection Calculated using CROWM to Investigate Area Effect	80
58. Reflection Distribution for Map1, Map 5 – Map 10 .....	81
59. Transmittance and Absorbance of the Maps .....	83
60. CROWM Versus OPAL2 Reflectance Comparison .....	84
61. Reflectance from Spectrophotometer Compared with CROWM .....	85
62. Structure used for Angular Transmittance Simulation .....	86
63. Angular Transmittance of Maps and Lambertian Scatterer .....	87
64. Structure for Comparison of Flat Case and the Maps .....	89
65. Illustrates the Effect of Positional Randomness of Pyramids .....	90

Figure		Page
66.	Comparison of Absorbance of Flat Case, Lambertian, Measured AFM Map and Modified Map .....	94
67.	Absorbance for All the Maps .....	95

# CHAPTER 1

## INTRODUCTION

### 1.1 Energy Landscape and Photovoltaic

The demand for energy is growing globally worldwide. With improving economies around the world and especially in Asia the purchasing power of individual user is increasing and so is the energy needs. It is predicted by US. Energy Information Administration (EIA) in [1] that the world energy consumption would grow by 56% from 2010 to 2040. In this scenario there is a strong emphasis to find renewable sources of energy to meet the increased demand. It is also expected the contribution of renewables would grow 2.5% each year as shown in Fig.1.

Figure 16. World energy consumption by fuel type, 1990-2040

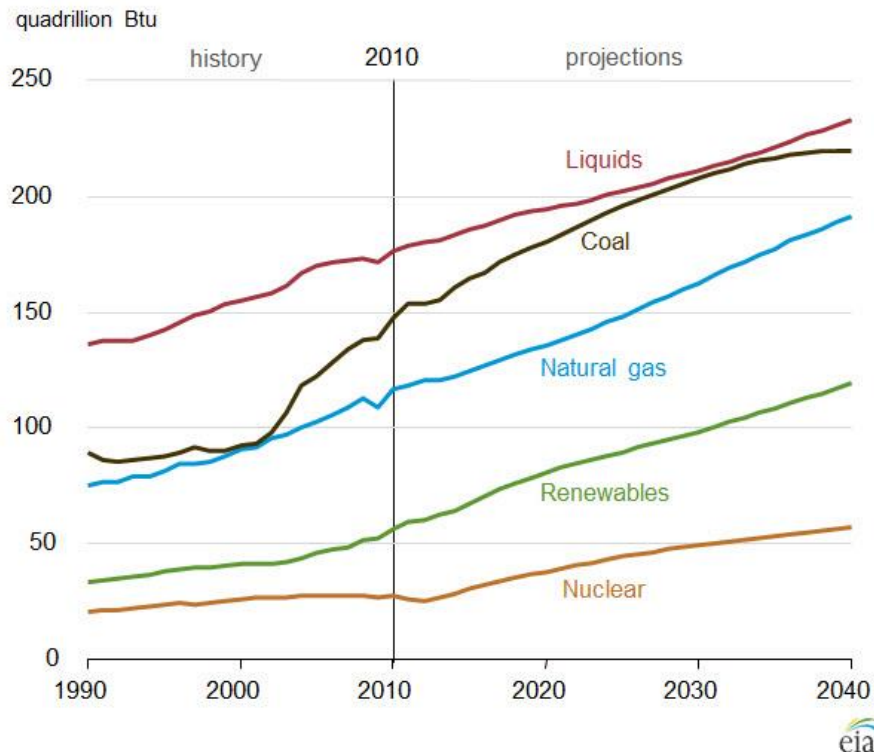


Figure 1 World Energy Consumption Trend [1]

In an Annual Energy Outlook 2014 [2] published by EIA it is estimated that total renewable generation (solar, wind, biomass, geothermal, hydropower etc) capacity would grow by 52% from 2010 to 2040. And just the wind and solar would approximately double during that time and almost all growth in generation capacity can be attributed to just these two. It is worth mentioning that solar electricity generation capacity would increase from 8GW in 2012 to 48GW in 2040 as shown in Fig.2.

Figure MT-36. Renewable electricity generating capacity by energy source, including end-use capacity in the Reference case, 2012-40

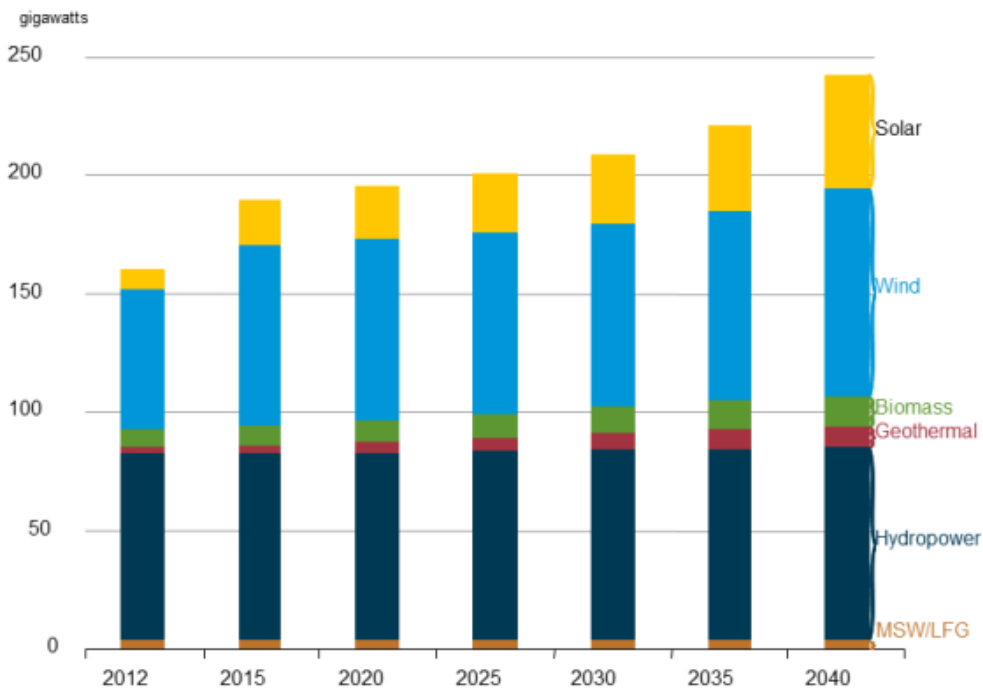


Figure 2 Growth Trend within Renewable Energy Sources [2].

Thus within renewables, Photovoltaic (PV) have important role to play. PV are devices that convert sunlight into electricity. PV are becoming increasingly popular throughout the world as an alternative source to produce electricity and thus energy.

They are being adopted by the society not just at factory or utility scale but also at household level. The reason for their rising demand is partly because of the increasing cost of fuels derived from fossil fuel and also because of the declining costs of PV. The reduction in cost of PV could be attributed to low-cost manufacturing of high quality materials necessary for making solar cells. This coupled with better solar cell device designs has bumped the efficiency of solar cells. Increase in efficiency essentially means use of less materials for the same amount of power thus further bringing down the cost.

If we further look at mix of technologies within the field of PV it easily becomes evident that the market is dominated by a single material known as Silicon (Si) as shown in Fig.3.

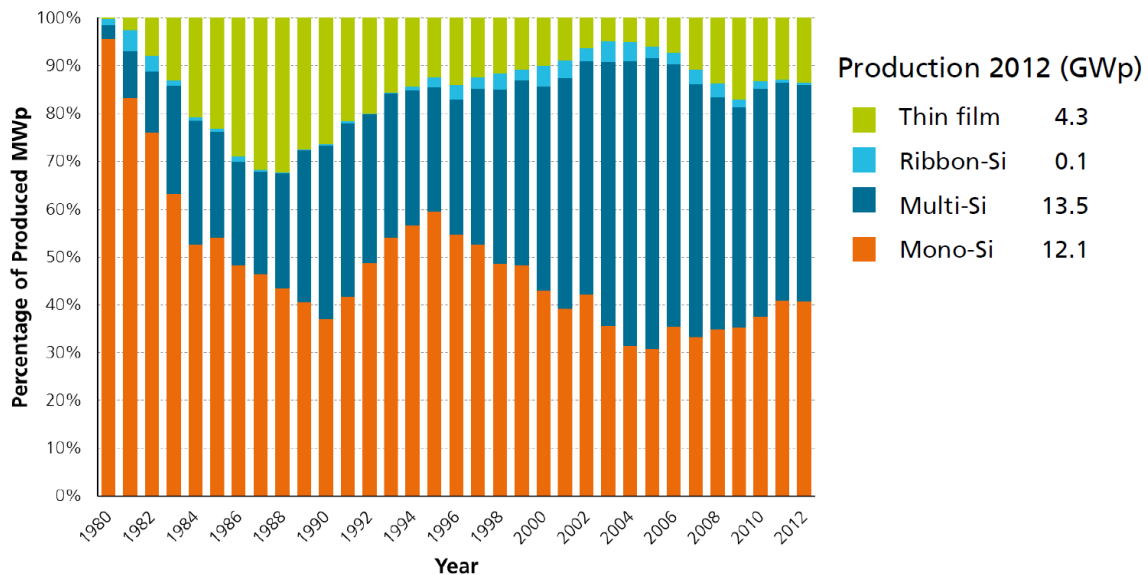


Figure 3 PV Production Development by Technology in Germany [4]

One of the most convincing reason for this is that Si is a material which is used a lot in Integrated Circuit (IC) industry which is quite older than PV industry. So it makes sense to use a material for which we already have developed great deal of knowledge and have infrastructure already setup for manufacturing. Besides this the

most cogent reason comes from Shockley-Quiesser in [3] who showed through detailed balance analysis that Si's bandgap (1.1 eV) being closest to the best bandgap needed to achieve highest efficiency with single junction solar cell (more discussion follows in coming sections).

Figure 4 shows the contribution in electricity generation of renewables is still behind coal and gas and looking at the trend in future it is clear renewables would still not be the main source of electricity generation.

**Figure MT-30. Electricity generation by fuel in the Reference case, 1990-2040 (trillion kilowatthours)**

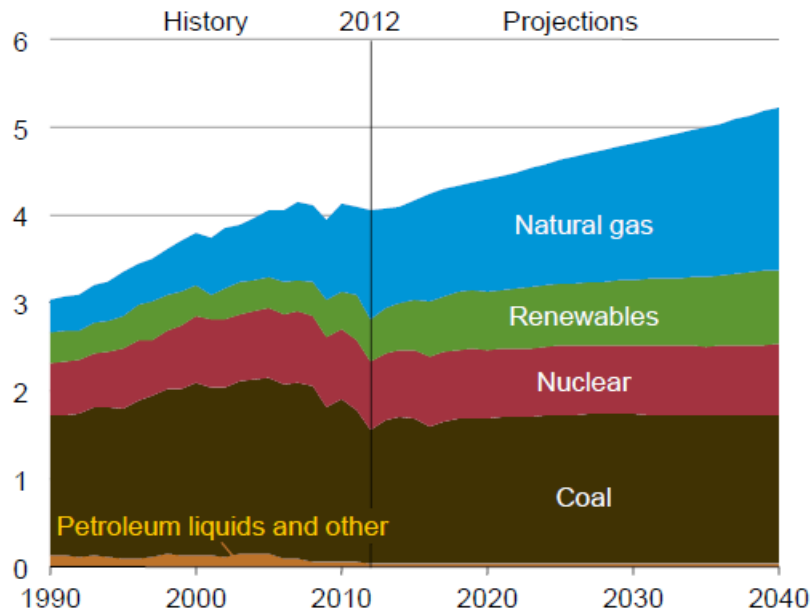


Figure 4 Electricity Generation by Fuel [2].

And from Fig. 2 it can be seen within renewables, solar is still behind wind and hydro power. The main limiting factor for solar technology from becoming the chief source of electricity generation is the cost. Thus it is imperative to reduce the cost of PV either by bringing down cost of manufacturing the PV modules or increasing the efficiency of solar cells. Fig. 5 shows the trend of cost of individual

materials that go into the making of whole Si solar cell PV module. It can be seen the cost of materials other than Si almost stays constant and the cost of Si is also stabilizing. That leaves only one way of reducing the cost and that is to increase efficiency of individual solar cells thereby producing same or more power with the lesser amount of materials. Using lesser material means thinning the Si wafer that poses new challenges as would be discussed in further sections.

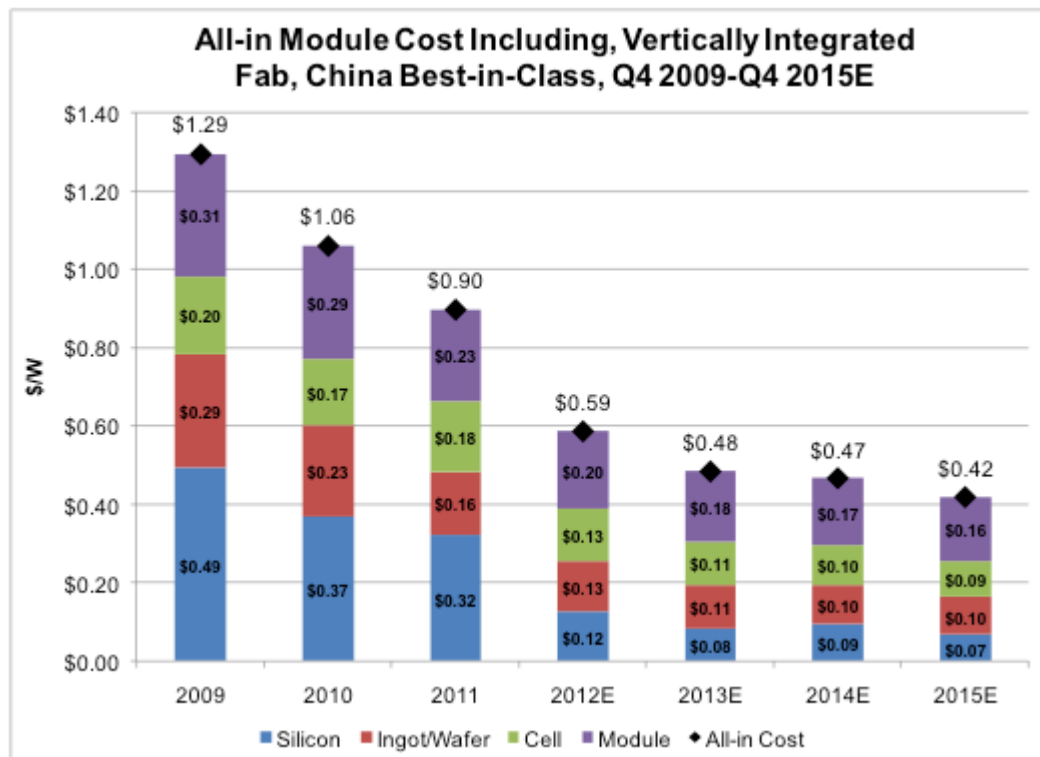


Figure 5 Cost of PV Module by it Elements [5].

## 1.2 Silicon as a Material for Solar Cell Applications

Silicon is a predominant material used in PV industry. One major reason for that is it is also the most used material in IC industry which is much older than PV industry. That means we inherit the vast knowledge about this material from IC industry as well as the manufacturing science and infrastructure from them to make solar cells. But this is a part of the reason, among other factors that place Si at the position of most favorite for solar cell application is that it is abundant on earth and non-toxic, two of the most important conditions for mass production to meet the world's energy demand.

More evidence in favor of Si comes from Shockley-Queisser [3] based on its bandgap. The suitability of a material can't be judged without discussing its bandgap for any application related to light absorption or emission. Before I discuss the analysis done in [3] it is important to mention sun's light is not monochromatic. But instead Sun puts out energy in form of a spectrum called solar spectrum which is sometimes approximated with black body spectrum. The property of solar spectrum is that it contains different amount of energy at different wavelengths as shown in Fig. 6. It can be seen most of the energy lies between the range of 400 nm to 800 nm wavelength. Any given material can only absorb light of energy greater than its bandgap which initially suggests that one should select a material having a bandgap of 0 eV to absorb all the energy in the spectrum. But it must be noted that the job of solar cell is to produce power which means maximizing the product of voltage (V) and current (I). When light is absorbed in a material it excites carriers from valence band to conduction band which leads to the splitting of quasi-fermi levels (splitting can never be more than the bandgap of a material) and their difference is a generated voltage and generated carriers contribute to current. So, if we choose a

# Solar Radiation Spectrum

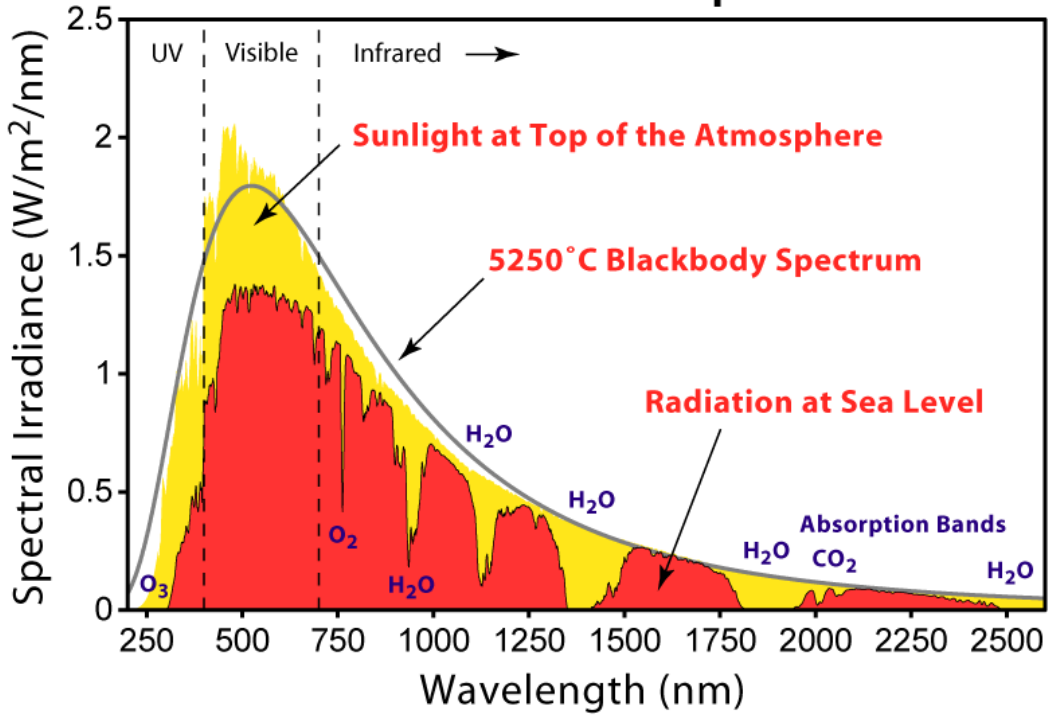


Figure 6 Solar Spectrum [6]

bandgap of 0 eV we would collect all the photons in the spectrum but it essentially means generated voltage would be 0 V and thus no power. Therefore, we must choose a material with a suitable bandgap that would lead to a decent voltage while also maximizing the absorption of photons. We don't want to choose a bandgap so high that we lose most of the photons because a given material can't absorb photons below its bandgap. Hence, this clearly is an optimization problem which Shockley and Queisser solved in 1961 [3]. Eq.1.1 is the detailed balance equation [7] for single junction solar cell needed to find the optimum bandgap.

$$J = qN = q \left( \frac{2\pi}{h^3 c^2} \right) \left[ fC \int_{E_G}^{\infty} \frac{E^2 dE}{\exp\left(\frac{E}{KT_{SUN}}\right) - 1} + (1 - fC) \int_{E_G}^{\infty} \frac{E^2 dE}{\exp\left(\frac{E}{KT}\right) - 1} - \int_{E_G}^{\infty} \frac{E^2 dE}{\exp\left(\frac{E - qV}{KT}\right) - 1} \right] \quad \text{Eq. 1.1}$$

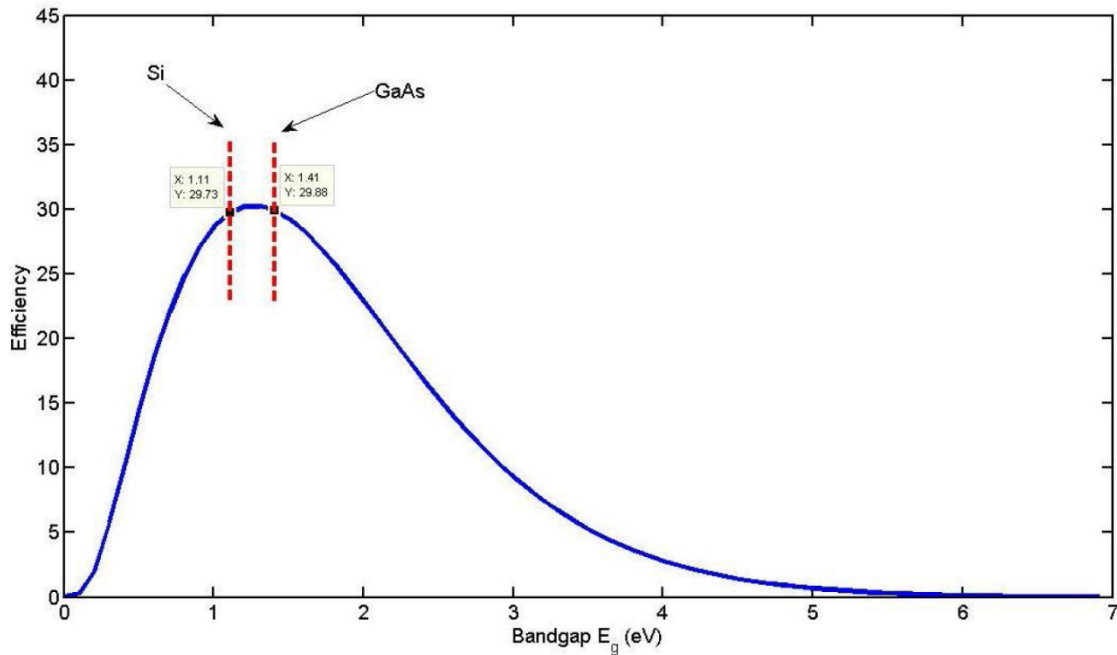


Figure 7 Plot of Detailed Balance Equation [8]

Fig. 7 shows a plot of Eq. 1.1 and it is shown that two most suitable materials for single junction solar cells are Si and Gallium Arsenide (GaAs) with bandgaps of 1.11 eV and 1.41 eV respectively. GaAs is expensive to produce and is only used in very high efficiency solar cells in space applications. For terrestrial applications Si is the most popular choice.

Another important feature of any material is its absorption ( $\alpha_a$ ) coefficient which reveals the material's ability to absorb light of certain wavelength. Although Si is quite near to the best according to its bandgap but it has relatively low absorption coefficient which means it doesn't absorb light very well in general. Si belongs to class of materials called indirect bandgap materials. These materials don't absorb light very well and the reason is that they don't allow direct transition of electrons from valence band to conduction band in an event of photon absorption. When electrons do get excited in Si it involves either absorption of phonon or emission of phonon. The involvement of phonon decreases the probability of excitation and

hence the overall absorption of photons. Fig. 8 shows the phenomenon of excitation in indirect bandgap materials.

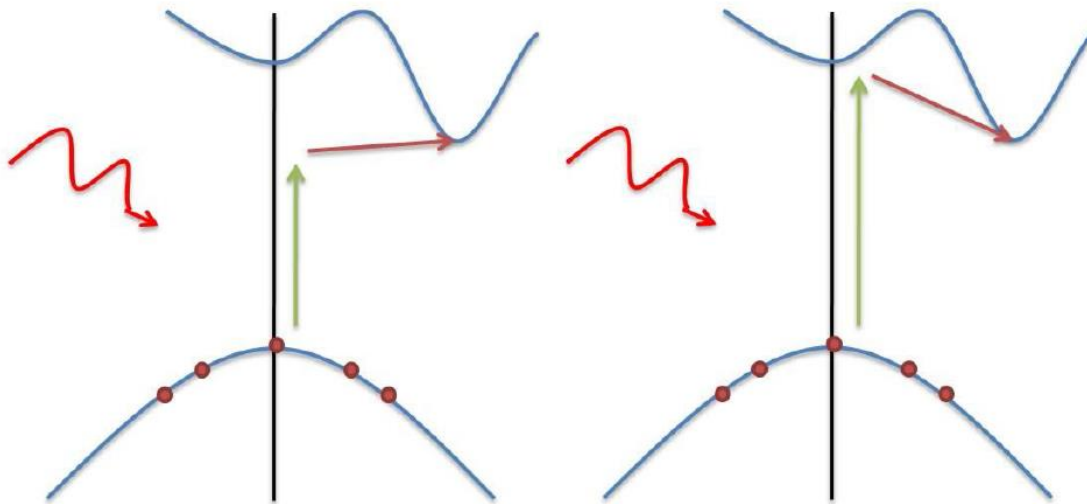


Figure 8 (Left) Indirect Transition with Phonon Absorption (Right) with Phonon Emission

Absorption coefficient ( $\alpha$ ) defines how far light of a particular wavelength can travel into the material before getting absorbed or how much of light intensity would diminish as it travels through the material [8]. It is given by Beer-Lambert law as:

$$I = I_0 e^{-\alpha_a x} \quad \text{Eq. 1.2}$$

where  $I_0$  = incident light intensity       $I$  = measured light intensity  
 $\alpha_a$  = absorption coefficient       $x$  = thickness of a material

Looking at the absorption curve of Si and comparing it to the other materials as shown in Fig. 9, it is evident Si have relatively low absorption coefficient. Especially in the region of 400 nm to 800 nm where most of the energy lies in solar spectrum, it is significantly lower than other solar cell materials. It means to absorb light in this

range Si has to be significantly thicker than other materials. And with a pressure to reduce the usage of material and reduce the thickness of Si wafer used in manufacturing solar cells forces to employ light trapping enhancement techniques. These are methods by which reflection from the top surface of Si is reduced by having light to bounce on the front surface more than once thus increasing the chances to transmit more light into the Si. Furthermore, such techniques make light to take a longer path inside the Si and thus allowing weakly absorbed light more distance to get absorbed. Various methods have been used in the past and are currently being used to enhance light trapping and thus enhancing efficiency. The goal of such methods is to roughen the front surface of Si. Sometimes it is also referred to as 'Texturing'. Most popular choice for doing so includes alkaline etching of Si wafer which produces random upright pyramids, acidic etch has also been tried, another important texture is regular inverted pyramids, regular upright pyramids etc. But to-date the most widely used in the industry is alkaline etching of Si that results in random upright pyramids. The reason for its popularity is the ease with which it can be produced. But troubling thing about this texture is the control of features and investigation of its light trapping properties. The light scattering properties of random upright pyramids has been the focus of research for so many years. The reason for this is that in 1981 Yablonovitch [9] showed if light rays can be scattered randomly like a Lambertian surface then the average path light rays take through Si wafer is  $4n^2$  times the thickness of the wafer (where  $n$  is the refractive index of Si = 3.5). This is known as path length enhancement. It is based on the principle of total internal reflection. Thus even when the wafer is thin the weakly absorbed light can be totally internally reflected many times between front and back surface to have better chance of absorbing it in Si rather than escaping from Si.

Thus the performance of modern Si based solar cells greatly depends on good light trapping and light management schemes which is the focus of this thesis.

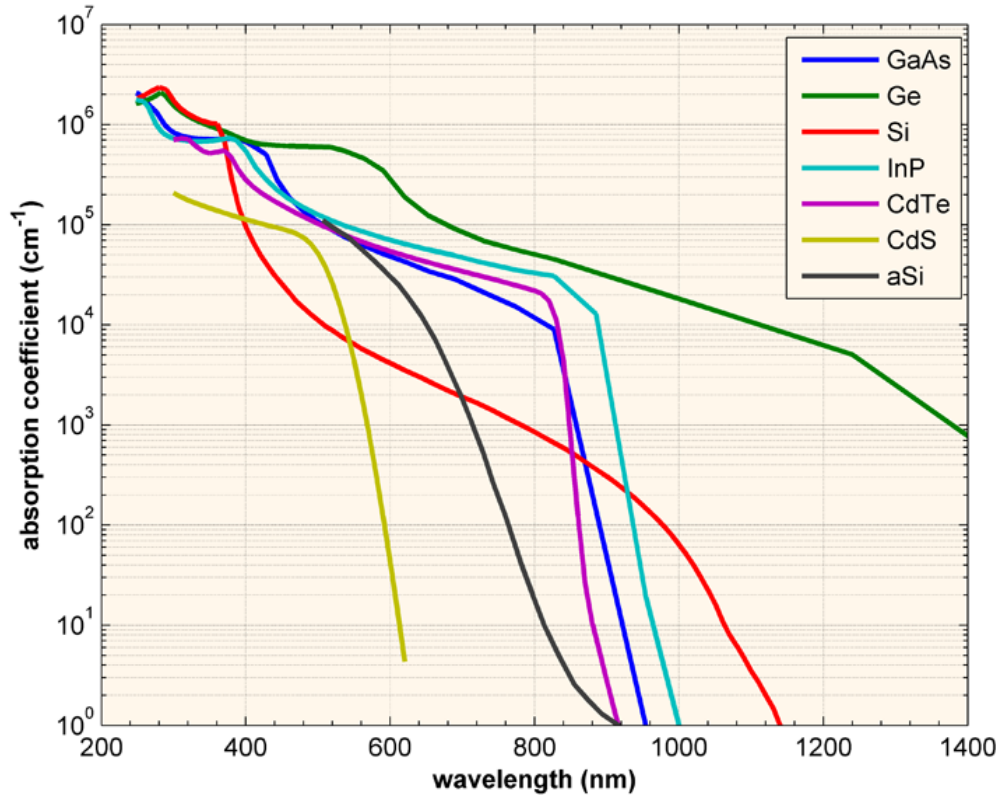


Figure 9 Absorption Curves of Popular Solar Cell Materials [8]

### 1.3 Aim of Thesis

In this thesis the main aim is to realistically investigate the true light trapping capabilities of randomly textured upright pyramids on front surface of Si solar cell. Such a texture is a result of alkaline etching of Si wafer. In 1981 Yablonovitch using statistical ray optics showed the theoretical maximum limit on path length enhancement for weakly absorbed light is  $4n^2$  [9] for a texture that could scatter light randomly like a lambertian surface. Later, it was generalized for intermediately absorbed light as well for lambertian scatterer. Therefore, the goal is to investigate is random upright pyramid texture the lambertian scatterer? So the approach is to scan the surface with AFM to capture the randomness in position of peaks of pyramids and as well as their randomness in z-height. It would be for the first time that any study on light trapping of randomly textured Si is presented that captures true randomness of the structure and not pseudo-randomness generated with computer. Such a map would facilitate numerous studies. In literature pyramid base angles between  $49^\circ$  –  $53^\circ$  degrees have been reported before. In this thesis therefore the focus would be to investigate the effect of distribution of base angle ( $\alpha_b$ ) (shown in Fig. 10) on the light trapping ability of the texture. For this I have created a code in Matlab that finds the positions of peaks and their heights in the map and creates a new map with arbitrary base angles.

Previously, most of the researchers have used single pyramid with different characteristics over and over again to simulate the random surface. It is for the first time that a true map of sufficient size that represents overall variation in the texture of front surface is investigated with a ray tracer all in one go.

Such study could facilitate investigation of many aspects of this texture but currently the focus is to vary the base angle distribution and measure the change in total reflection, transmittance, absorbance and also change in short circuit current.

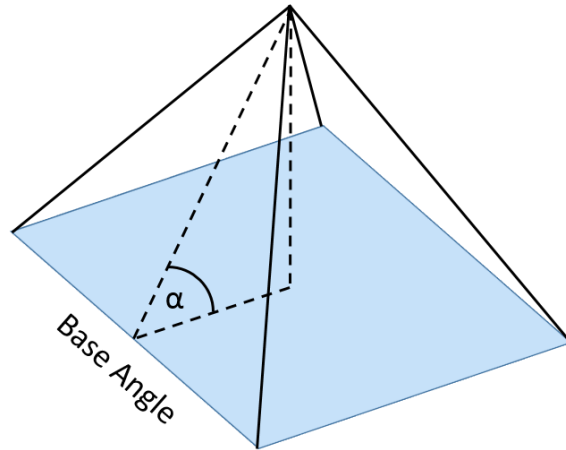


Figure 10 Illustration showing Base Angle of Pyramid.

Another novel outcome of the study is that scattering pattern of light entering the Si from front surface can be recorded. Scattering pattern is probed with changing base angle of pyramids. This not only reveals the knowledge about path length enhancement but also could greatly help in the design of back reflector. Based on the scattering pattern the back reflector design could be chosen such that it totally internally reflects all of the light.

Rest of the thesis is organized as following: Chapter 2 presents the main benefits and goals of light trapping with randomly textured upright pyramids. It also reviews the simulation and experimental characterization methods for front side texture.

Chapter 3 presents the Atomic Force Microscopy as a tool to scan the dynamic surface of textured Si wafer and the challenges for correctly capturing the randomness of the surface.

Chapter 4 presents the overall process of obtaining maps with AFM, validation of measured map, modification of measured map using Matlab and results of optical simulation using CROWM ray tracer.

In Chapter 5, presents the conclusion and summary of the work and also future work.

## CHAPTER 2

### CHARACTERIZATION OF FRONT SURFACE LIGHT TRAPPING

In this chapter I review the principles and goals and design strategies of light trapping for Si solar cells. The focus is on randomly textured upright pyramids. Later in the chapter the modelling and characterization techniques associated with this texture are presented.

#### 2.1 Benefits of Light Trapping

The overarching goal of any light trapping scheme for Si solar cells is to reduce reflection from front surface. This is achieved by texturing the front surface with random upright pyramids that forces light to bounce more than once on the front surface and thus giving multiple chances to light rays to enter the Si wafer as shown in Fig. 11.

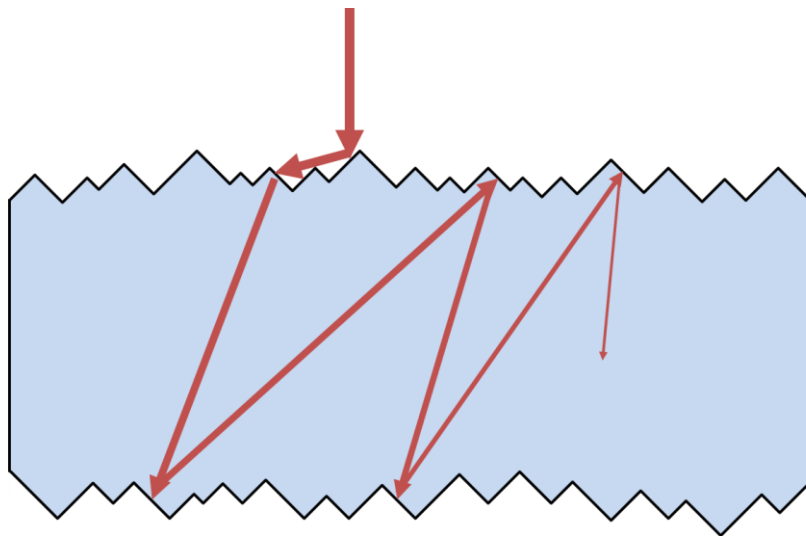


Figure 11 Effect of Texturing the Surface of Si Wafer.

Another important consequence of texturing the front surface is that when light rays strike the front surface at oblique angle they take a longer path through the Si wafer. This phenomenon is often referred to as Path Length Enhancement. It is an important feature by which we can gauge the performance of a texture as it allows weakly absorbed light close to the band edge take an angled path through the wafer and so have more time to be absorbed. This ability to obliquely transmit light into the Si could also be used to fine tune the location of absorption of light inside the wafer such that the generated carriers are within the diffusion length to the collection points.

Third benefit of employing such a texture is that it allows thinning of Si wafer. It is beneficial because it reduces the cost by saving Si but more importantly it relaxes the constraint of having high purity of Si wafer as thinning makes collection of generated carriers easy by reducing the distance that generated carriers would have to travel before getting collected.

## 2.2 Lambertian Surface and Yablonovitch Limit

Lambertian surface is the one that reflects light randomly in all directions and thus appears to have same luminance in all directions. Light from such a surface gets scattered in half-space adjacent to the surface at all possible angles randomly. This type of reflectance is often time called diffuse reflectance. It is shown in Fig. 12.

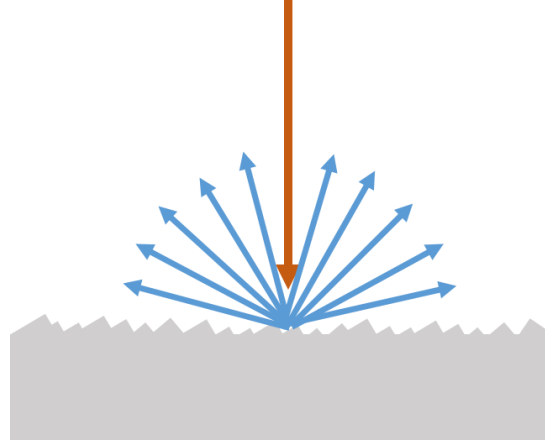


Figure 12 Lambertian Surface.

In [8] authors showed using statistical ray optics that the intensity enhancement of electromagnetic energy (black body radiation) inside an optical medium with respect to its outside is  $n^2$ , where  $n$  is a refractive index of the material. The intensity enhancement occurs due to higher density of states available for electromagnetic modes to occupy which is proportional to  $n^2$ . It is further derived that even for arbitrary illumination (whether isotropic like black body radiation or non-isotropic) condition the intensity enhancement factor is the same. This enhancement could further be increased for one-sided illumination by having a white surface on the other side to  $2n^2$  (in other words a perfect reflector). It is pointed out that it is true for situation when light entering the medium loses all its connection to its initial incident angle. This means the medium should be able to randomize the light within the medium to a good degree. Intensity enhancement with respect to a vacuum is given by Eq. 2.1.

$$I = \frac{h\omega}{\exp\left(\frac{h\omega}{kT}\right) - 1} \frac{2d\Omega n^2 \omega}{(2\pi)^3 c^2} d\omega \quad \text{Eq. 2.1}$$

The factor of  $n^2$  appearing in the equation above is the intensity enhancement factor. It is further shown it translates into an absorption enhancement in absorbing

mediums. Absorption enhancement is imperative for solar cells. It is especially important for wavelength that are weakly absorbed in silicon due to its relatively low absorption coefficient. Using detailed balance of incident photons and escaped photons the absorption enhancement due to angular randomization of light inside the medium is calculated and shown that absorption is enhanced by  $4n^2$ .

Later, in [10] Campbell et al, showed absorption enhancement due to lambertian scattering could also be understood as path length enhancement of weakly absorbed light. The proof begins by showing that probability or fraction of light escaping at each bounce at the boundary for a randomizing surface is given by Eq. 2.3.

$$f = \frac{\int_0^{\theta_c} B \cos \theta \sin \theta d\theta}{\int_0^{\pi/2} B \cos \theta \sin \theta d\theta} = \frac{1}{n^2} \quad \text{Eq. 2.2}$$

Next, by assuming a randomizing surface at the top and a rear surface of reflectivity  $R$ , a sum series is formed of the path lengths of weakly absorbed rays that escape from the front surface. It is given by Eq

$$\begin{aligned} P &= W[2(1-R) + 4fR + 6R(1-f)(1-R) + 8f(1-f)R^2 + \dots] \quad \text{Eq. 2.4} \\ &= 2W \left( \sum_{N=0}^{\infty} [(2N+1)(1-R) + (2N+2)fR][R(1-f)]^N \right) \end{aligned}$$

Using power series it is reduced to

$$P = \frac{2W(1+R)}{[1-R(1-f)]} \quad \text{Eq. 2.5}$$

Putting values for  $f$  equal to  $1/n^2$  and in case of unit transmittance of top surface and perfect back reflector having  $R=1$ , results in an average path length of

$$P = 4n^2W \quad \text{Eq. 2.6}$$

for weakly absorbed light, where  $W$  is the thickness of the wafer. This enhancement of  $4n^2$  initially pointed out as absorption enhancement is also known as Lambertian limit or Yablonovitch limit for weakly absorbed light.

Later, more general expression for limit of absorption enhancement for lambertian scatterer was developed by Deckman et al. in [41][42] that applies to intermediately absorbed light as well as to weakly absorbed light. Neglecting the parasitic absorption in the contacts of the solar cell, the expression for absorption is given by Eq. 2.7.

$$A = \frac{1 - e^{-4\alpha_a W}}{1 - e^{-4\alpha_a l} + \frac{e^{-4\alpha_a W}}{n^2}} \quad \text{Eq. 2.7}$$

Where  $\alpha_a$  is the absorption coefficient and  $W$  is the wafer thickness.

### 2.3 Modelling and Simulation

To-date among the popular choices for texturing the front surface of silicon wafer for light trapping includes regular upright pyramids, inverted pyramids, V-grooves, random upright pyramids etc. There are more textures that have been discussed in literature but they are generally based on one of the textures mentioned before. The kind of simulations that have been conducted to evaluate the performance of these textures base the comparison on different metrics, such as, path length enhancement, number of rays remaining trapped after each pass within the substrate, reflection from front surface, short-circuit current etc.

Generally, comparison is done with the help of tracing a ray within the substrate and programs are based on Monte-Carlo simulation. Number of such programs are available, such as, RaySim6.0 [11], Texture [12]. SunRays [13] etc. The governing principle of these simulation programs is first to define a unit cell. A ray enters the unit cell and reflects from the front surface and/or couple into the substrate where it gets reflected from the back surface or leaves the unit cell from the side wall. If so, then another unit cell is created where the ray enters at the corresponding point where it had left the previous unit cell. And that's how the simulation is continued. The process is depicted below in Fig. 13.

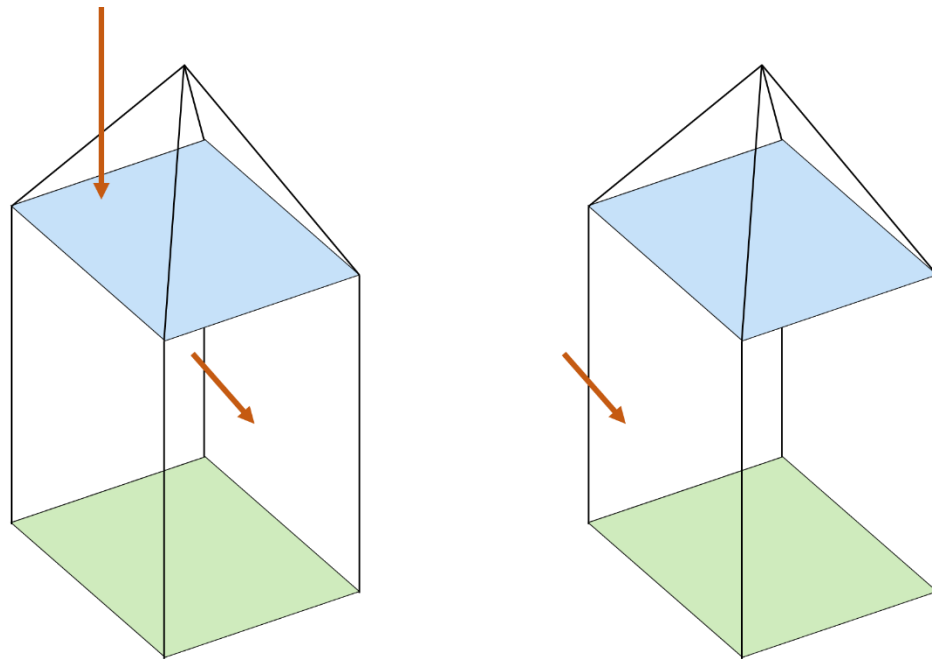


Figure 13 Example of Ray Tracing using Monte Carlo Simulation. (Left) Unit Cell A, Ray Leaves from the Side Wall (Right) Unit Cell B, Ray Enters at Corresponding Point.

This method of simulation is simple but limited in its application. It can be used to simulate textures which are periodic and have simple unit cell. Therefore,

simple textures like regular upright pyramid, tilted pyramid, slat structure, inverted pyramids etc could be simulated. For example, for regular upright pyramid texture all pyramids are considered to be of the same height and they touch each other with centers of pyramids aligned. The base angle of each pyramid is generally considered to be  $54.74^\circ$ . To simulate it, such a texture is applied to the top surface and the back surface is assumed to be flat with perfect reflectance, that is,  $R=1$ .

### 2.3.1 Simulation Results Comparing Textures Using Path Length Enhancement

To conduct ray tracing study to investigate the path length enhancement of any texture, usually a weakly absorbed light is considered. The assumption is the light ray incident on the texture, once coupled in to the substrate doesn't get absorbed and just bounces around until it falls within the escape cone and leaves the substrate through the front surface. It is important to mention the back surface is assumed to be flat and acts as a perfect reflector. The situation is shown in Fig. 14.

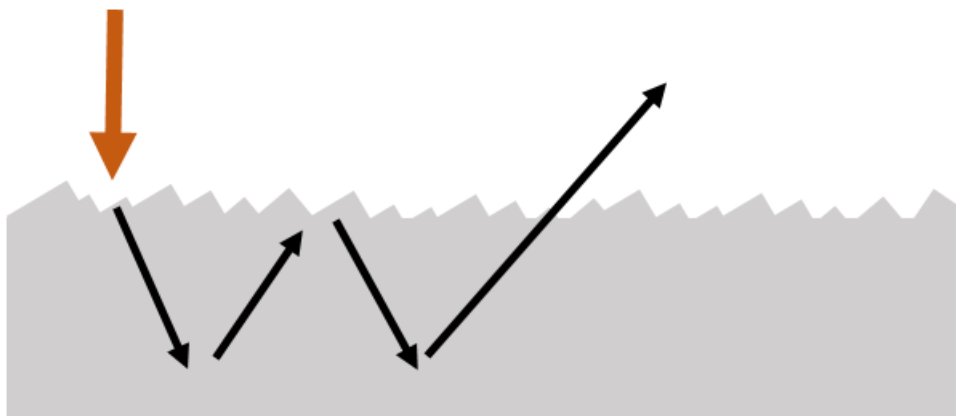


Figure 14 The Setup for Path Length Enhancement Simulations.

In [10] Campbell et al, compared different textures using ray tracing for path length enhancement, but more importantly compared them for the number of rays remaining inside the substrate versus the passes. Results are shown in Fig. 15.

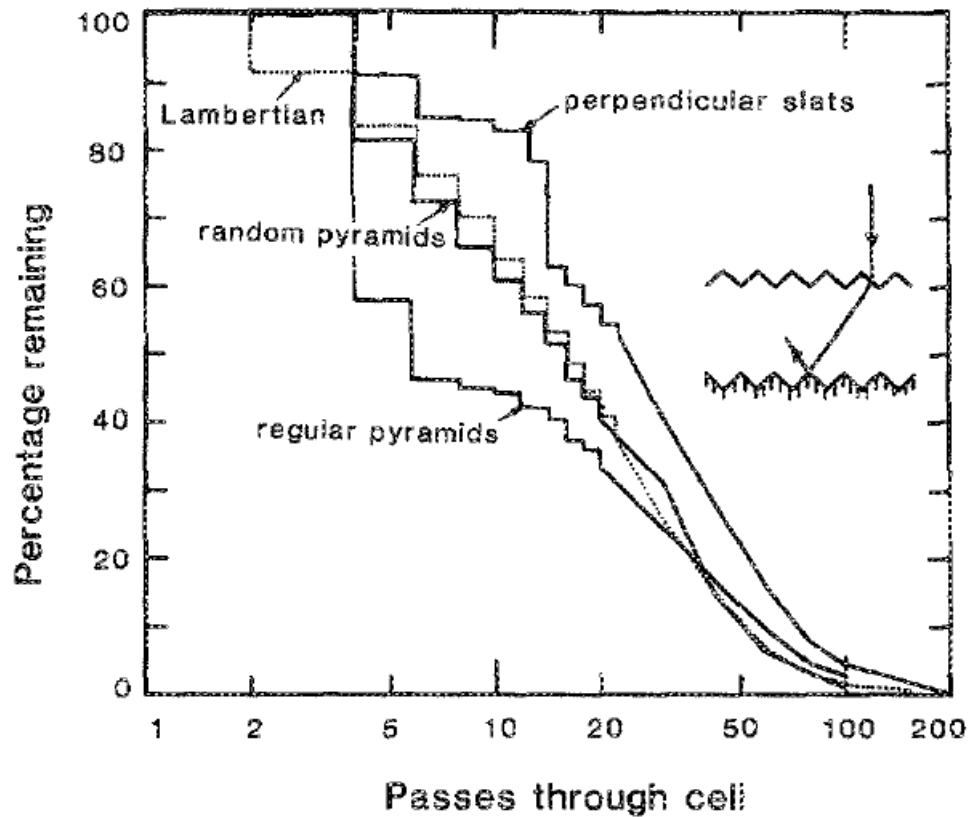


Figure 15 Percentage of Rays Remaining Versus The Passes Through Cell [10].

Fig. 15 shows lambertian surface performs really well in trapping the rays for smaller number of passes as well as for large number of passes. In [10] a new type of texture is proposed called the slat, which shows superior performance in trapping the rays than lambertian. It is also shown random pyramids perform quite close to the lambertian surface.

Later in [14] Brendel et al., showed the effect of standard deviation in path length enhancement versus the facet angle of different textures. His ray tracing study showed that almost all the textures included in the study achieved the  $4n^2$  limit. He concluded the sharp prism when it has a facet angle of  $17^\circ$  shows the least standard deviation in path length enhancement and sharp prism groove also produced highest short circuit current. His results are shown in Fig. 16.

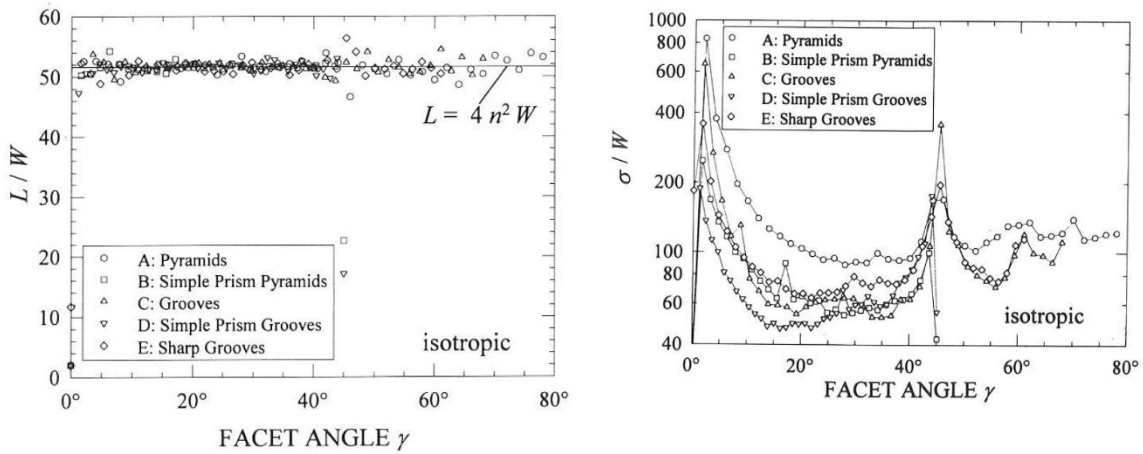


Figure 16 (left) Shows Path Length Enhancement Versus Facet Angle (Right) Shows Standard Deviation in Path Length Enhancement Versus Facet Angle [14].

Fig. 16 clearly shows while almost all textures achieve  $4n^2$  average path length enhancement limit but they have very different standard deviation for path lengths. And it has huge impact on over all light trapping and hence on short circuit current generation.

### 2.3.2 Simulation for Front Surface Reflectance Characterization

While the focus of previous section was to compare textures according to their ability to trap light rays inside the substrate once they have entered the

substrate. But, alone this is not enough to have efficient light management. Another important role that texture needs to play is to efficiently couple the light rays in to the substrate. And different textures have different capabilities to couple the light. The best way to evaluate this is by comparing the front surface reflectance.

Before some of the results are discussed, there is a need to explain how the random upright pyramid texture is constructed. First, it was presented by Rodriguez et al. in [15] and later Baker et al. in [16] adopted the same model for constructing random upright pyramids to study its reflection pattern in case of normally incident light. In this model the starting pyramid has a randomly chosen height between  $h_{\max}$  and  $h_{\min}$ . Light ray hits this pyramid and reflects toward a new pyramid in destination unit cell. The destination unit cell is defined by three parameters. First for a destination unit cell a height of the pyramid is randomly selected between  $h_{\max}$  and  $h_{\min}$ , second its center is laterally displaced by a distance  $\Delta l$  and lastly the cell is vertically displaced by a random distance of  $\Delta v$  both with respect to the previous unit cell. This way the ray keeps propagating from one cell to a new cell until it could no longer be confined due to the texture. The process is pictorially depicted in Fig. 17.

The method used for calculating the front surface reflectance involves using concepts from geometrical optics. It is argued that light rays falling on regular upright and inverted pyramid texture follow preferential paths. These paths are found using ray tracing and geometric optics. In regular upright pyramids rays follow two paths called A and B with respective probabilities of 89% ( $f_A$ ) and 11% ( $f_B$ ). Thus the total reflection from regular upright pyramids is given by Eq. 2.8.

$$R_{reg,up} = 0.8889R_A + 0.1111R_B \quad \text{Eq. 2.8}$$

Here  $R_A$  and  $R_B$  represent the reflection of path A and B respectively.

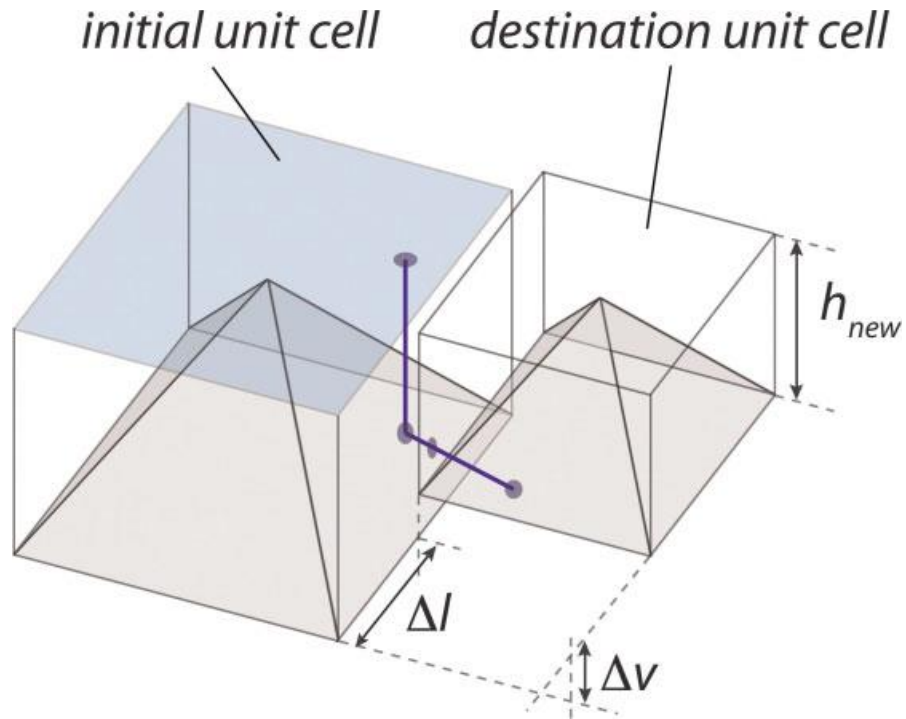


Figure 17 Random Upright Pyramidal Texture Creation. Shown is a Starting Unit Cell and Destination Unit Cell that has Random Height and is Laterally and Vertically Displaced Randomly with Respect to the Previous Cell [16].

Similarly, an expression for regular inverted pyramids is obtained which has three preferential paths (A, B, C). Two are the same as regular upright pyramid but there is a third path where ray bounces three times before escaping. These paths for regular upright and regular inverted pyramids is shown in Fig. 18. The total reflection for regular inverted pyramid is given by Eq. 2.9.

$$R_{reg,inv} = 0.5789R_A + 0.0211R_B + 0.4R_C \quad \text{Eq. 2.9}$$

The reflection of preferential paths for random upright pyramids are calculated using 3D ray tracing calculus as explained by Yun et al. in [17]. For preferential paths and reflection of each path reader is referred to [16].

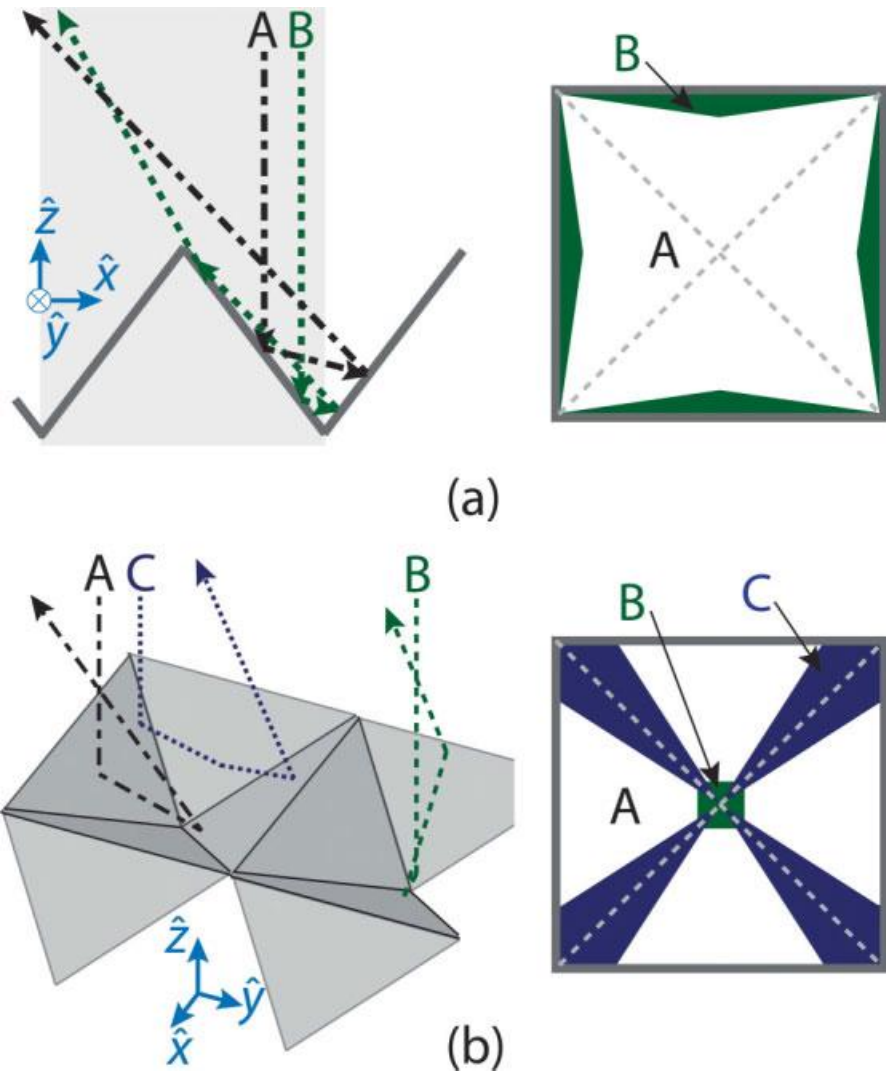


Figure 18 (a) Shows the Preferential Paths for Regular Upright Pyramids (B) Shows the Preferential Paths for Regular Inverted Pyramids [16].

Based on this model and calculation the authors of [16] have created an open source program for analysis of reflection from front surface of silicon solar cells. It is OPAL [18][19] and now in 2012 its second version was made available. It allows to change the characteristic angle of pyramids and observe the effect on front surface reflectance.

## 2.4 Experimental Characterization of Front Surface Reflectance

Experimental characterization of front surface reflectance is a little tricky because it would require that the back surface reflectance be neglected. This is not a problem for strong absorbing wavelengths but for weakly absorbed light back surface contributes to the reflection from front surface, often known as escape reflection. Generally, total reflection is measured using a spectrophotometer [20]. A layout of spectrophotometer equipped with integrating sphere is given in Fig. 19.

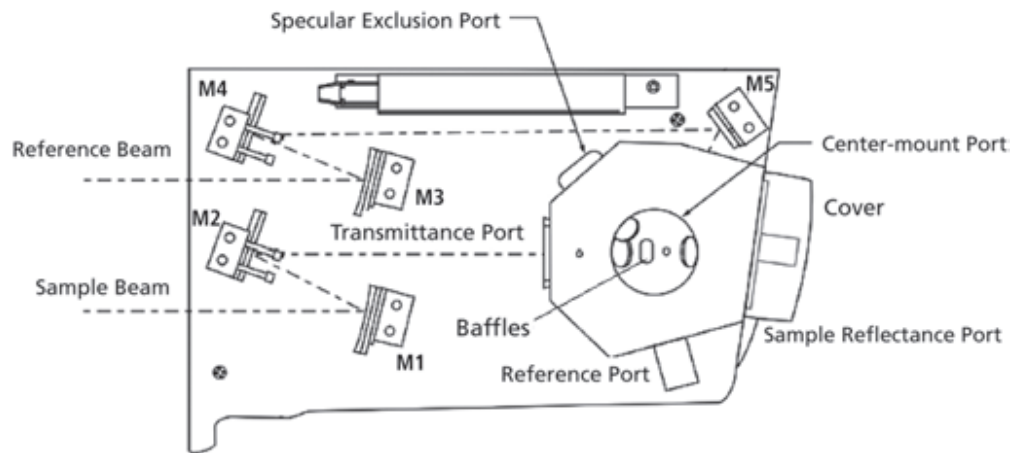


Figure 19 A Layout of Spectrophotometer with Integrating Sphere [20].

Sample is placed at the reflectance port and light is incident through the transmittance port which reflect from the sample and enters the integrating sphere and here the detector measures the total reflectance.

### 2.4.1 Angular Resolved Scattering Using Spectrophotometer

Total reflection alone doesn't fully reveal all the characteristics of the textured surface. It is important to see how the reflected light from the front surface is angularly distributed. For this purpose angular resolved scattering measurements are performed and they involve illuminating a rough sample with normally incident light which reflects from the front surface. The reflected light scatters with a distinct angular distribution often also called angular resolved reflectance (ARR). For the purpose of this measurement a detector with small opening is rotated in plane parallel to the normal of the wafer with small angular steps (e.g 2° degrees). From the opening light enters in an integrating sphere where the intensity is registered. The setup is shown in Fig. 20.

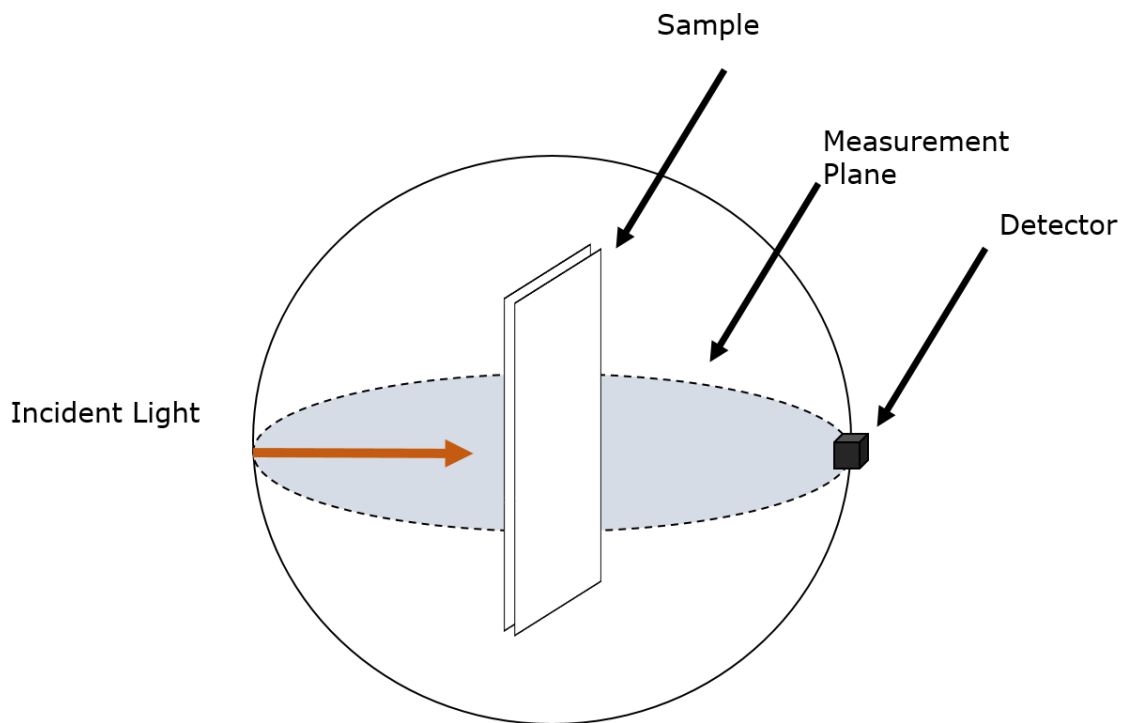


Figure 20 Angular Resolved Scattering Measurement Arrangement.

The angular resolved scattering measurement reveals knowledge about the shape of the surface morphology. If there are flat features on the surface the normally incident light doesn't scatter much and is registered back at the detector at smaller angles, whereas if the features are sharp and random the scattering would show randomization which is an indication of lambertian surface. Thus, ARR measurement has important application for solar cells.

In [22] Baker et al, used ARR measurement to find out the characteristic angle of pyramidal texture. In their earlier work they showed for regular inverted pyramidal texture normally incident light reflects along preferential paths and maximum fraction of light is reflected back along path A which makes an angle of approximately 39° degrees with the incident light for pyramids having base angle of 54.7° degrees. In ARR measurement the peak is observed at exactly the same angle. Thus, confirming ARR measurement can be used to find out the characteristic base angle of pyramidal texture. The authors also calculated the characteristic base angle of random upright pyramids using ARR measurements. Their result is shown in Fig. 21. The peak in the ARS measurement denoted as  $\theta_r$  and characteristic base angle of pyramids denoted as  $\alpha_b$  are related to each other by Eq. 2.10.

$$\theta_r = 4\alpha_b - 180 \quad \text{Eq. 2.10}$$

Using the equation above the distribution of base angle in Fig. 21b is calculated for ARR measurement shown in Fig. 21a.

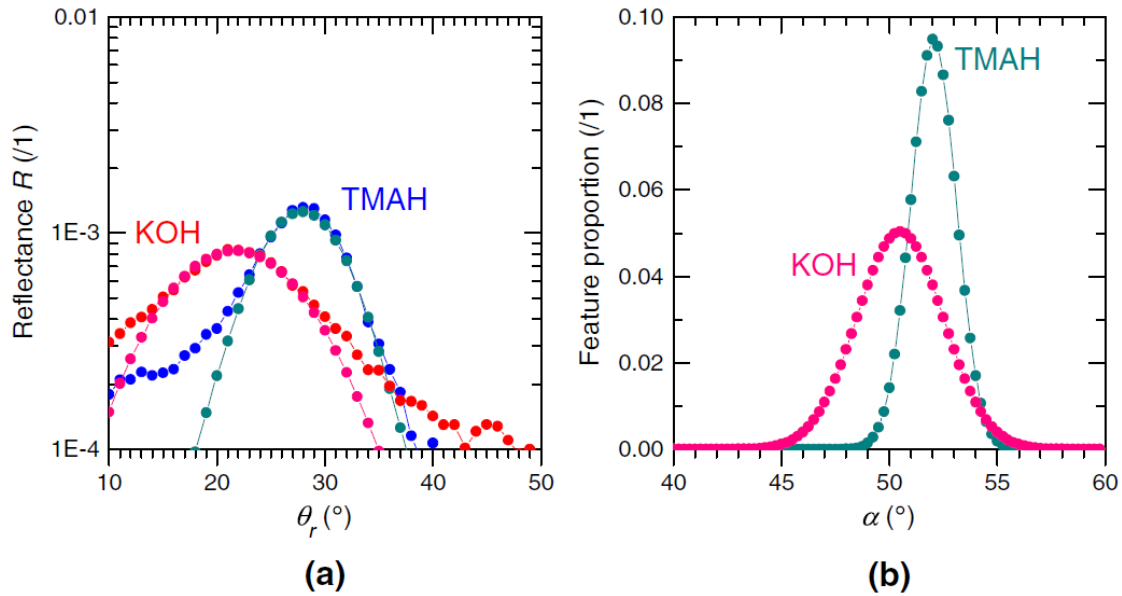


Figure 21 (a) Shows ARR Measurement for Random Upright Pyramids Textured with Two Different Chemicals (KOH And TMAH) (B) Shows the Calculated Characteristic Angle of Pyramids [22].

#### 2.4.2 Characterization of 2-D Reflection Distribution from Front Surface

2-D reflection distribution was first obtained by Rodriguez et al. in [15] but a more detailed explanation of the optical setup and obtained reflection pattern was given by Yang in [23]. The optical setup used by Yang is shown in Fig. 22. The setup consists of 532 nm green laser with power of 5mW. A photographic film or semi-transparent sheet is placed between the laser and the textured sample. In the middle of the film is a small hole through which laser hits the sample surface. The reflected light pattern is recorded on the film which is later developed and digitized or a digital camera could be used with semi-transparent sheet for taking digital photos of the reflection pattern. In [23] the 2D pattern obtained for inverted pyramid case is explained using the same nomenclature as used by Baker et al. in [16] that is rays preferentially taking path A, B or C.

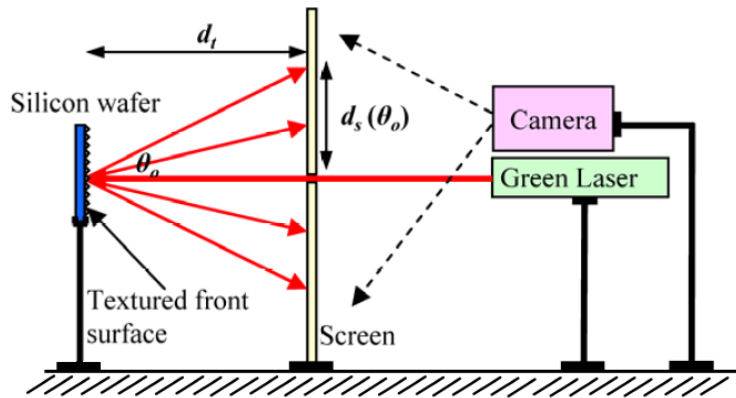


Figure 22 Optical Setup for Obtaining 2D Reflection Distribution from Front Surface [23].

The location of these rays on 2D plane as explained by Yang is shown in Fig.

23.

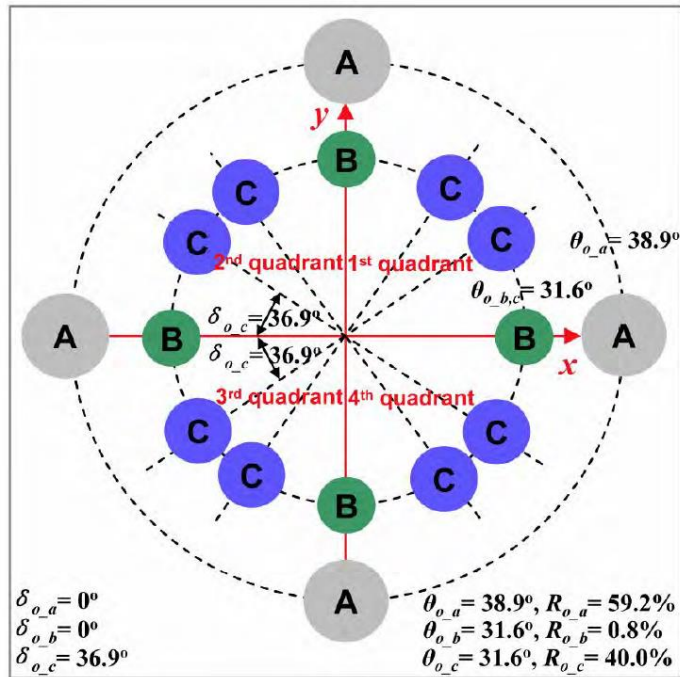


Figure 23 2D Reflection Distribution from Front Surface for Inverted Pyramid [23].

For the case of random upright pyramids the 2D reflection pattern becomes continuous and it is difficult to distinguish between different ray paths. Thus, the 2D

pattern is digitized and MATLAB is used to analyze the results. It is showed that it is possible to extract the 1-D reflection distribution which is in-line with the previous results as in [16].

## CHAPTER 3

### ATOMIC FORCE MICROSCOPY (AFM)

#### 3.1 Main Components of AFM Machine

The invention of scanning tunneling microscopy (STM) in 1981 at IBM paved way for the invention of Atomic Force Microscopy (AFM) later in 1986 by Binnig and Quate [24]. This technique is capable of 'nm' resolution in x-y and z-directions with magnification ranging from 100X to 100,000,000X. The reason it can achieve such high resolution is its ultra-sharp probe tip. AFM relies on a very sharp probe tip attached to a cantilever for high magnification. The main working principle of this instrument is to raster-scan a probe on the surface of a sample while maintaining close proximity to the surface.

The main components of a typical AFM machine are shown in Fig. 24. They broadly are: Piezoelectric sensor, Force sensor and feedback loop.

**Piezoelectric Sensor:** It is a special material (usually ceramic, PZT etc) capable of generating voltage when stressed to change shape and vice-versa. It can expand or contract and its sensitivity is 0.1nm per volt. Precise motion of AFM probe in x-y and z direction is controlled with this. In z-direction the probe is supposed to follow the surface very close and the force between the surface and the probe tip should stay constant to keep the z-distance constant. So, with the help of this piezoelectric ceramic/sensor the probe tip is moved up or down based on the voltage given to it by the feedback loop.

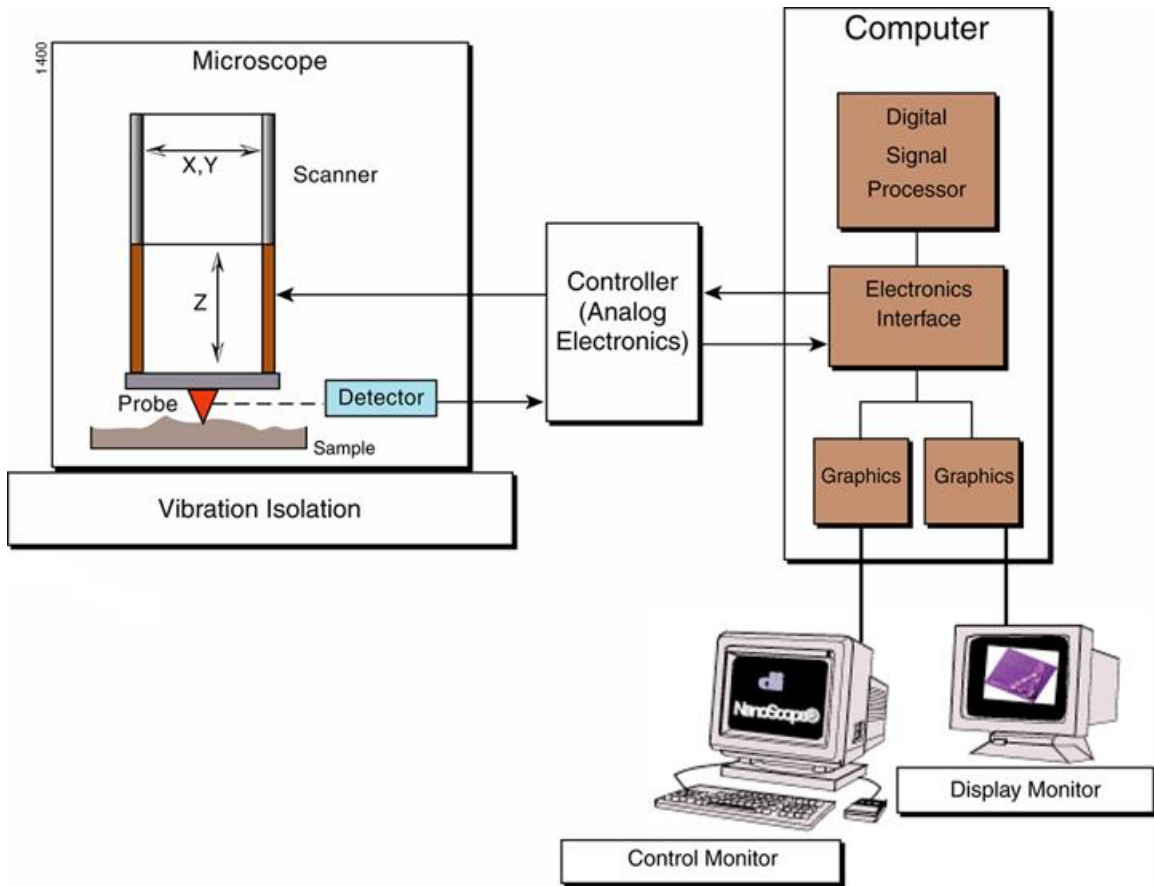


Figure 24 Typical AFM Machine [25].

Force Sensor: Next most important component of the AFM machine is its force sensor. The main job of the sensor is to detect the force being exerted at the probe. So, when the probe moves along the surface and gets deflected by the features, it bends the cantilever to which the probe is attached. This amount of deflection of the cantilever indicates the force between the surface and the tip. Usually, to sense this deflection and hence the force on the cantilever, a light lever force sensor is used. The depiction of such a sensor is shown in Fig. 25.

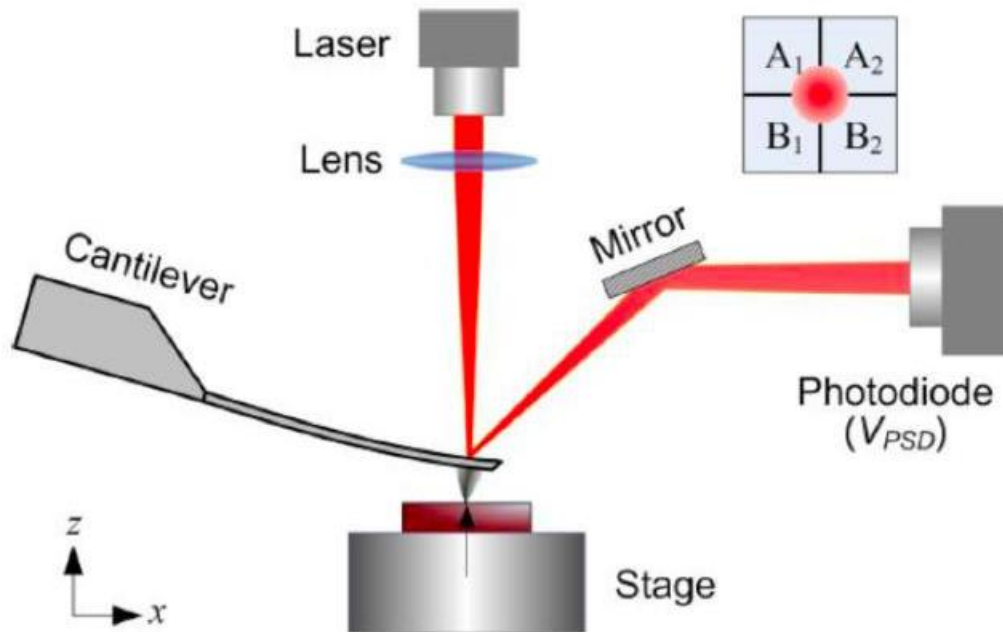


Figure 25 Light Lever Method for Cantilever Deflection Detection [26].

A laser is shun on the end of the cantilever where the probe tip is attached. Usually cantilever has a good reflecting surface, and thus the laser is reflected off from there and focused to fall on a four quadrant photodiode. As the deflection of the cantilever increases the spot made on the photodiode from reflection of the laser also moves. So, based on this movement the change in z-height of surface is registered. Typically, the force that it can detect is as low as picoNewtons.

Feedback loop: Last but not the least the feedback loop is the most important part of an AFM setup. It is very important to keep the probe at fixed height above the surface by way of sensing the force being exerted on it. Depending on the distance from the surface the tip may experience attractive or repulsive force. And this force increases or decreases as probe tip moves up or down with respect to the surface. So the main role of this loop is to constantly monitor the input from force sensor and

judge the height of the probe tip and in event of change in the reading it informs the piezoelectric sensor to move the tip up or down to keep the force constant.

### 3.2 MODES OF OPERATION

There are different modes in which AFM can be operated. Depending on the need and application one has to choose the mode. The basic principle for topographic imaging is to raster scan the probe tip over the surface. Based on distance at which tip is scanned over the sample's surface the force experienced by cantilever is either attractive or repulsive or varies between both. The relationship of force with respect to the distance between the tip and the surface is given in Fig. 26.

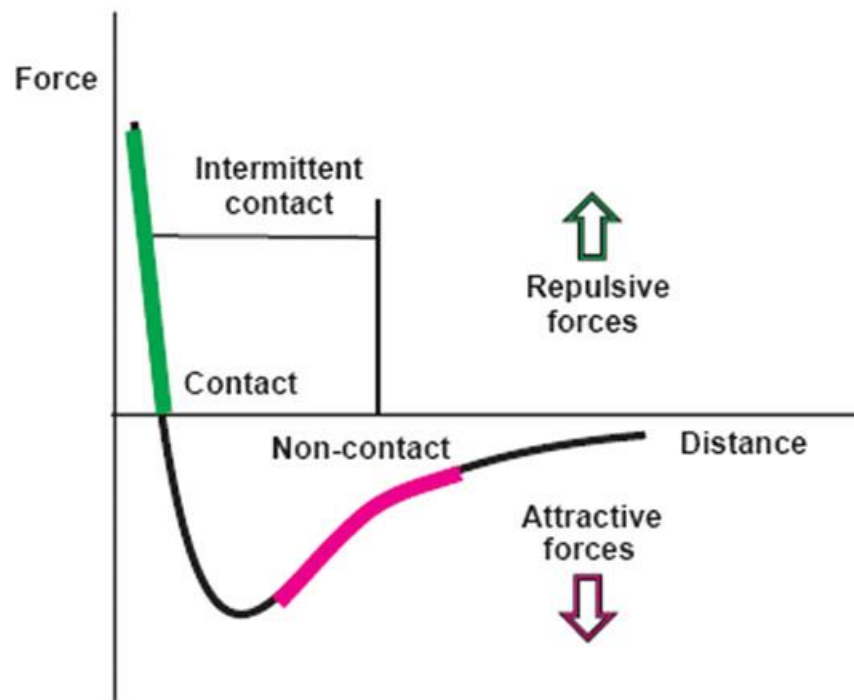


Figure 26 Forces Between Probe Tip and Surface with Respect to Distance and Different Mode [27].

When the probe is at a reasonable distance from the surface, tip experiences an attractive force. And if the tip is slowly brought closer to the surface the force reaches its maximum and then becomes repulsive and it is said that the tip has touched the surface.

### 3.2.1 Static Mode

In static mode the cantilever is stationary (non-vibrating) and touches the surface and thus the forces on the cantilever are repulsive. It is often also called contact mode. It is important to mention, it is difficult to tell when the tip touches the surface at atomic scale because there is no surface boundary as is the case in macroscopic view. But the tip glides over the surface so close that forces are repulsive. And throughout the scanning the aim is to maintain a constant force on the surface. It is judged by deflection of the cantilever which is read by noticing the movement of the laser on quadrant photodiode. As the laser moves the feedback signal is sent to the piezoelectric sensor to raise or lower the tip to keep the force exerted by the tip on the surface constant. Usually, the force exerted by the tip ranges from nN (nano-Newtons) to  $\mu$ N (micro-Newtons). The probe tip plays very vital role in contact mode. Normally contact mode AFM is done on hard samples so typically the tips for this mode are made from silicon or silicon nitride. Tips are characterized by their apex radius of curvature and their half-cone angles (which also defines the aspect-ratio of the tip).

The basis for topographic imaging with contact mode is the measurement of deflection of cantilever. The force exerted by the tip on the surface is proportional to the deflection or displacement of laser on quadrant photodiode. This proportionality is defined by the force constant 'k' of the cantilever. The movement up or down of tip

necessary to keep the force constant is registered and is used to build topographic image of the surface.

### 3.2.2 Dynamic Mode

In dynamic mode the cantilever is made to vibrate at resonance frequency or close to it. It is done with the help of an oscillator that vibrates cantilever with particular frequency and/or amplitude. Depending on the tip-sample distance the tip may touch or tap the surface of the sample at the lowest point of the vibration. In such a case the tip is said to operating in the intermittent mode or tapping mode. In this mode the tip-sample distance is such that tip experience a repulsive force. There is another possibility that the minimum distance between tip and sample be such that the tip may not touch or tap the surface. In such a case the tip is said to be in non-contact mode. And the tip may experience repulsive and attractive force or just the attractive force based on the minimum distance between the tip and sample.

For getting a topographic information these mode can be operated either with amplitude modulation (AM) or frequency modulation (FM). In AM the premise is that tip is to maintain a constant distance above the sample. But when sample comes in contact with the surface features the amplitude of vibration may decrease or increase. So, by tracking the amplitude of the vibration feedback loop tells the piezo sensor to lift or lower the tip to bring back the amplitude of the tip to the set value and thereby maintain a constant distance between tip and sample. In FM goal stays the same that is to maintain constant distance above the surface but when tip comes closer or goes farther to the surface the frequency of the oscillations change. Again, the feedback loop senses the change and informs servo system to raise or lower the tip to bring

back the frequency of the oscillations to the set value and hence maintaining the constant distance between tip and sample. Fig. 27 shows the difference between AM and FM.

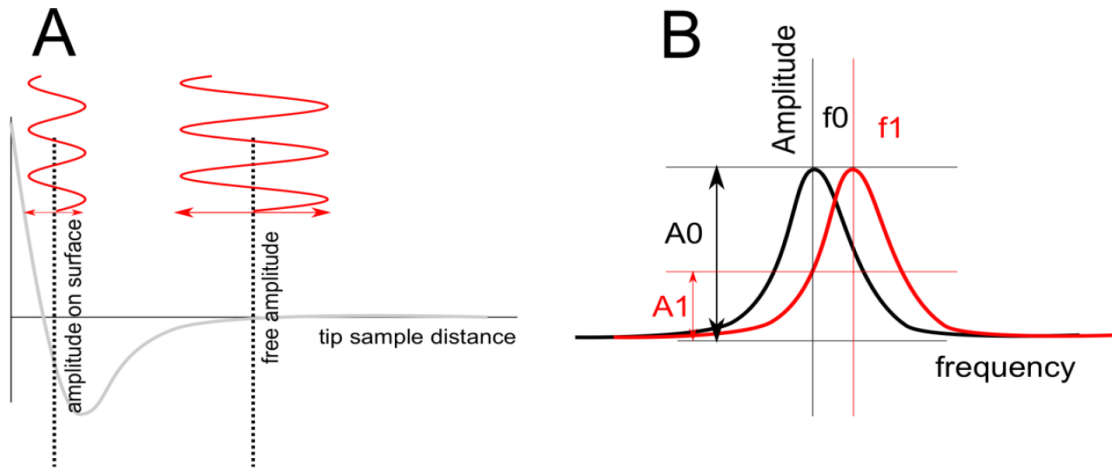


Figure 27 Amplitude and Frequency Modulation [26].

### 3.3 Comparison of Contact, Tapping and Non-Contact Modes

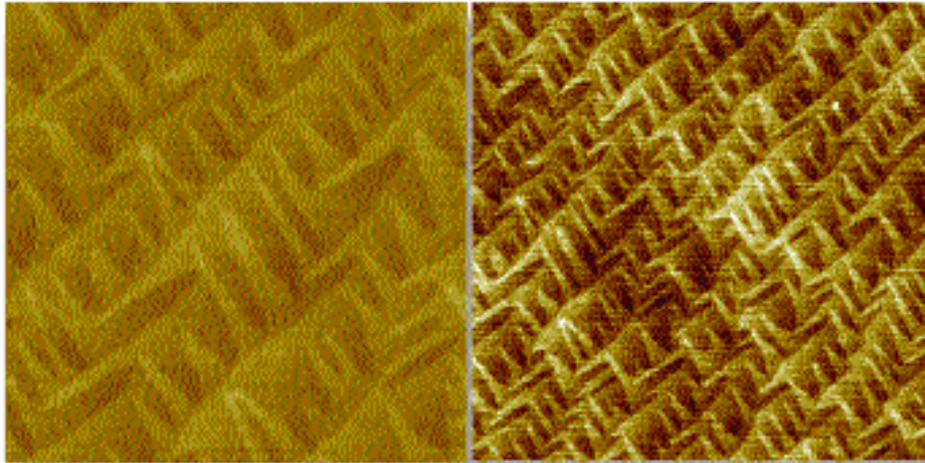
Table 1 Comparison of Contact, Tapping and Non-Contact Modes

Contact Mode	Tapping Mode	Non-Contact Mode
<b><u>Pros</u></b>		
<ul style="list-style-type: none"> <li>• High Scan Speed</li> <li>• Highest resolution (atomic resolution).</li> <li>• Rough samples with rapid changes</li> </ul>	<ul style="list-style-type: none"> <li>• High lateral resolution (1nm – 5nm).</li> <li>• No torsional forces on the cantilever.</li> </ul>	<ul style="list-style-type: none"> <li>• No force exerted on the sample. So no damage of the surface.</li> </ul>

<p>in vertical axis can relatively be easy to scan in this mode.</p>	<ul style="list-style-type: none"> <li>Doesn't damage the sample.</li> </ul>	
<p><b><u>Cons</u></b></p>		
<ul style="list-style-type: none"> <li>Torsional forces on the cantilever can bend it and distort the image.</li> <li>High tip-sample forces can result in the damage of the sample, especially soft sample, biological sample, silicon etc.</li> </ul>	<ul style="list-style-type: none"> <li>Slightly slower scan speed than contact mode.</li> </ul>	<ul style="list-style-type: none"> <li>Lowest lateral resolution.</li> <li>It has slowest scan speed of the three modes to make sure tip doesn't touch the surface.</li> <li>If the adsorbed fluid on the surface is thick, the tip can get stuck and damage the surface.</li> </ul>

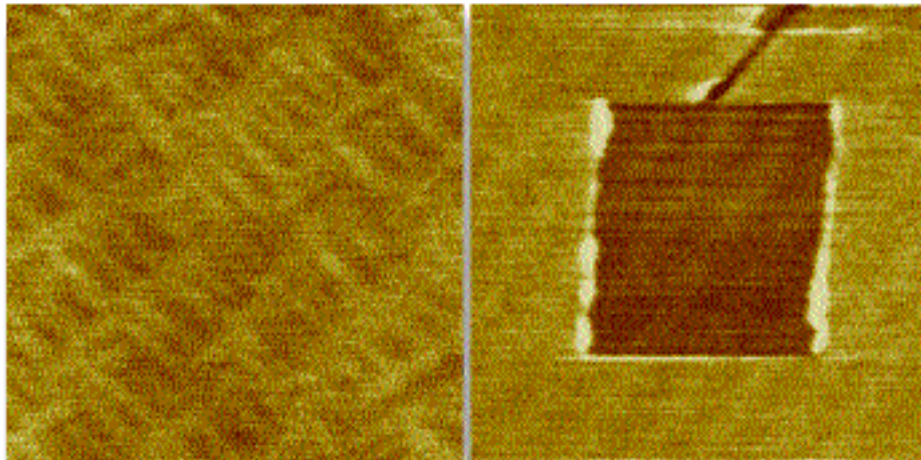
### 3.4 Selecting Mode for Topographical Imaging of Silicon

Silicon is an important material and used predominantly in the IC industry and now also in PV industry. So, the ability to scan silicon's surface correctly with AFM could have huge impact. To date numerous structures at micron and nano scale have been made with silicon. And the characterization of their shape and size is extremely important. For example, in IC industry the side wall angles, the thickness and lengths of structures made on silicon's surface effect the performance of devices. Similarly, the pyramidal texture made on silicon's surface with alkaline etching has extremely important role to play in light trapping in solar cells. Thus, the ability to accurately study these structures on silicon is essential. But, silicon is a challenging surface to scan with AFM as it has strong surface forces on  $\langle 111 \rangle$  faces due to dangling bonds. And its  $\langle 111 \rangle$  face that is exposed after etching silicon in alkaline bath. So, it is an extremely reactive surface. It has been shown by Kizuka and Hosoki in [28] that scanning silicon with silicon tip in contact mode the tip breaks and also causes damage to the surface due to strong surface force. Therefore, some non-contact method must be employed to scan silicon's surface, especially when silicon tip has to be used. As most tips available commercially are made with silicon so it is practical to use 'tapping mode' to do AFM of silicon surface. Complete non-contact mode isn't chosen as it has the lowest lateral resolution but tapping mode offers the benefit of non-contact but still maintains good lateral resolution. A good comparison of contact mode imaging of silicon and tapping mode is given in [29] where it shown while tapping mode gives better lateral resolution, the contact mode actually damages the surface, shown in Fig. 28.



a) 1  $\mu\text{m}$  scan/Tapping Mode

b) 2  $\mu\text{m}$  scan/Tapping Mode



c) 1  $\mu\text{m}$  scan/Contact Mode

d) 2  $\mu\text{m}$  scan/Contact Mode

Figure 28 Contact and Tapping Mode Images for the Same (100) Silicon Epitaxial Wafer [29].

In Fig. 28, a) and c) are the scans before increasing the scan area. And b) and d) are second scans including the area scanned during the first scan. It could be seen contact mode image has a poor resolution and it has also damaged the surface whereas the tapping mode image shows good resolution and there is no sign of

surface damage. Therefore, tapping is a suitable mode for scanning the silicon surface.

### 3.5 Common Artefacts in AFM Images

AFM is a technique that apparently seems simple in terms of the setup and materials needed to build it but in fact it is actually prone to a lot of errors. To get accurate images it requires very fine tuning of several parameters and also requires a very good knowledge of the physical machine and as well as sample to be imaged and AFM probe. There is a very strong dependence of image quality and accuracy on the forces involving the interaction of tip and sample and also the geometry of tip and features on the surface. Furthermore, AFM is based on feedback system which means it has to be calibrated to make dimensional measurements. And there are several errors and artefacts associated with AFM images if not correctly calibrated.

#### 3.5.1 Probe/Tip Artefacts

The geometry or shape of the tip has a special relationship with the geometry of the features that are to be scanned and the accuracy of measurements depend on it. Thus, it is very important to choose the right tip otherwise the AFM scan could be plagued with artefacts. Commonly, the tips are characterized by their apex radius of curvature ( $R_{\text{tip}}$ ), and aspect-ratio of the tip ( $A_r$ ) or cone/half-cone angle ( $\alpha_{\text{tip}}$ ).

As a rule of thumb, tip's radius of curvature ( $R_{\text{tip}}$ ) should be smaller than the curvature of features and aspect-ratio ( $A_r$ ) should be greater than the features. But, the constraints on these values can be relaxed depending on the application. If side-

wall angle of features that have large angles are to be measured than very high  $A_r$  value tip is required. Furthermore, the tip height should be greater than the height of features. But, if such conditions are not kept in mind then numerous artefacts could be present in the image. If the probe has a bigger  $R_{tip}$  than features, then it could dilate the features in the scan and on the other hand if the features have higher aspect-ratio than the tip's  $A_r$ , it could make features appear smaller in the image. So,  $R_{tip}$  determines the lateral resolution of the AFM. The sharper the tip the higher resolution. This is shown in Fig. 29.

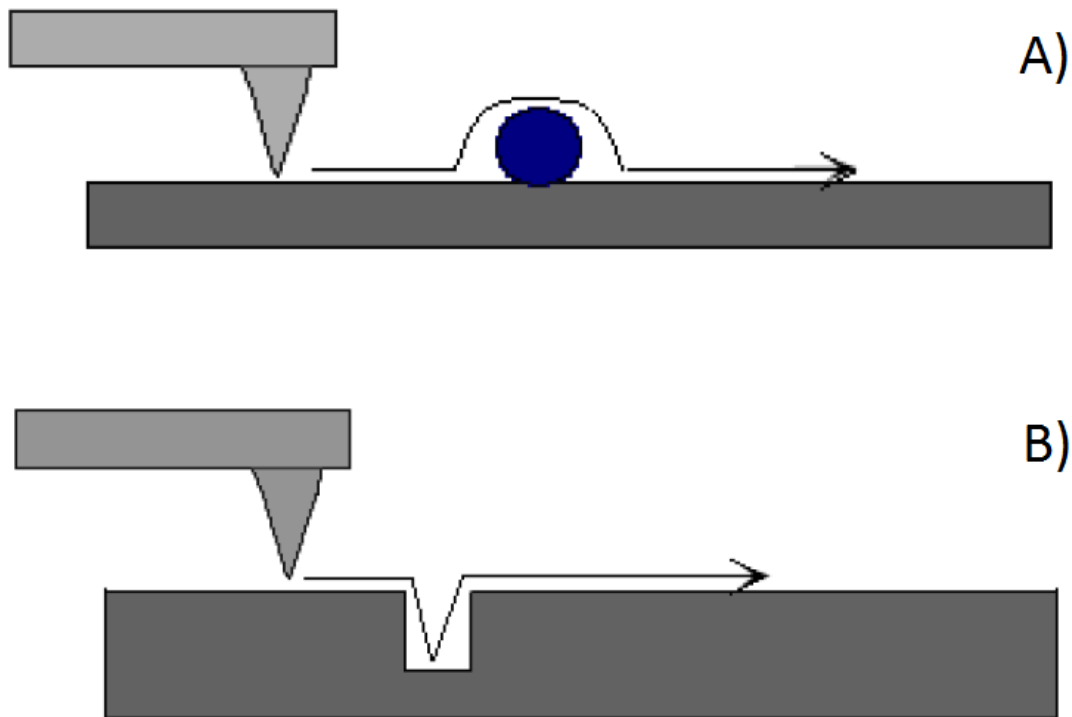


Figure 29 A) Shows that Features Dilate when Tip is not Sharp B) Shows that Features Appear Small when Tip Doesn't have high enough Aspect-Ratio [30].

The  $A_r$  of a tip effects the height measurements as well as side wall measurements. In other words the wide tip can't reach the bottom of the features. This problem is compounded especially if the features are deep like a trench, and are very close to each other as is the case of silicon surface etched in alkaline bath. Then the requirements on the tip become very stringent and the tip is needed that has ultrasharp tip (extremely small  $R_{tip}$ ) as well as very high  $A_r$ . It is illustrated in Fig. 30.

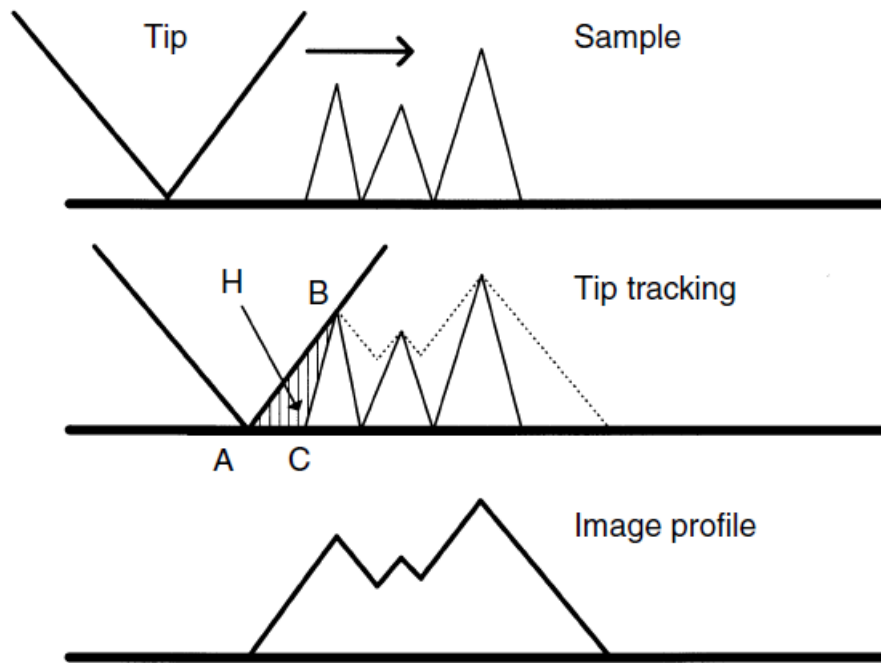


Figure 30 Effect of Aspect-Ratio and Radius of Curvature on the Profile [31].

Probe tips are fragile and with use over time undergo wear and may break down, making the tip blunt. Sometime, one tip can break into two tips. In addition to this contamination on the surface can get stuck to the tip. These things introduce artefacts in the image. Example of such an artefact is given in Fig. 31.

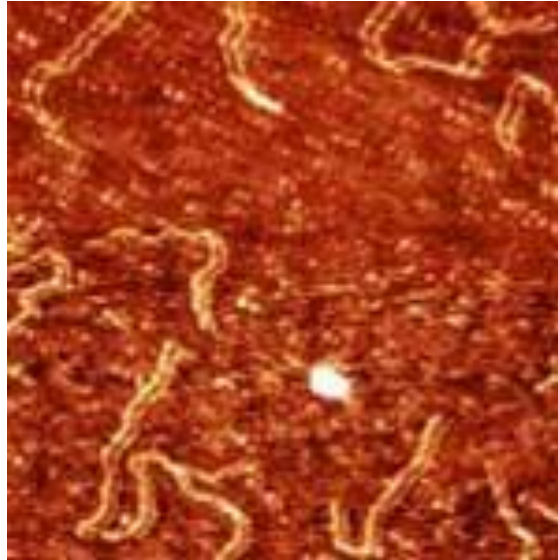


Figure 31 AFM Scan of a DNA Showing Repetition of each Feature [30].

### 3.6 Types of Probes/Tips

There are several types of probes available commercially [32][33]. Probes are categorized according to their application and then further segregated based on their material and physical parameters, which include their cantilever length, thickness, width, tip height, radius of curvature of tip, aspect-ratio of the tip etc.

## CHAPTER 4

### EXPERIMENTATION AND RESULTS

The purpose of experimentation is to get a 3 dimensional model of the surface of textured silicon wafer as accurately as possible. As explained in the previous chapter it is possible with AFM. So, once the map is obtained it is characterized by its base angle distribution. The idea is to measure it's light trapping capability by tracing rays and calculating the absorbance and short circuit current. Furthermore, since there is a limit to light trapping as explained by Yablonovitch in [9] and by Deckman et al. in [42] the comparison is performed with lambertian scatterer. To investigate the impact of having different shape of base angle distribution on the light trapping and scattering the measured map is modified. So, the comparison is performed between lambertian scatterer, measured AFM map and modified maps.

#### 4.1 Probe Tip Selection

Based on the discussion in previous chapter it is evident that to accurately measure the height and angles of the pyramids, the tip has to be selected carefully as it would determine how accurate the results could be obtained with AFM. Textured silicon surface has high density of features and in addition to that features have reasonably high angles, plus the heights of the features is also larger than the features normally scanned with AFM. So, all of these reasons put extreme constraints on the choice of the tip. Therefore, only after trying number of probe tips it was found that very high aspect-ratio, very sharp (low radius of curvature) tip and long length of high-aspect-ratio is required.

The tip ultimately used is AR10T-NCHR which is a high-aspect-ratio tip generally used for measuring large angles and measuring the depth of narrow trenches. Another reason why it is selected is because it is tilt compensated. Generally, all AFM probe holders induce certain tilt in the probe tip which can lead to wrong angle measurements.

Important probe specifications are:

- Length of high aspect ratio portion of the tip > 1.5  $\mu\text{m}$ .
- Typical aspect ratio at 1.5  $\mu\text{m}$  in the order of 12:1.
- High aspect ratio portion of the tip tilted  $13^\circ$  to the cantilever surface normal.
- Radius of curvature < 15nm.

More information is available at [32]. Fig. 32 shows this probe tip.

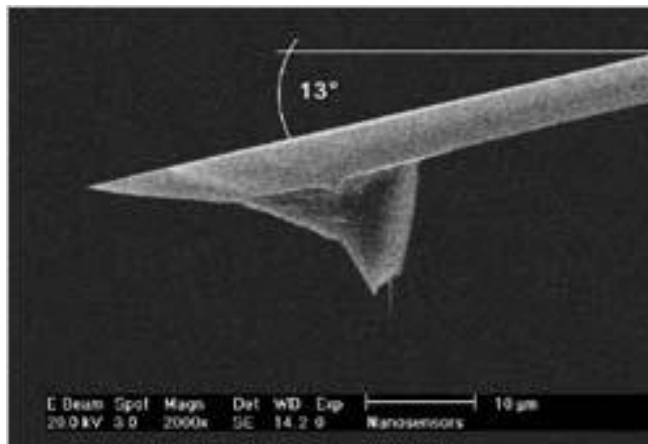


Figure 32 AR10T-NCHR High Aspect Ratio Tip Used in this Work [32].

## 4.2 Calibration of AFM

AFM is a feedback technique and rely on ceramic piezoes for motion, both of which require that AFM be routinely checked for correct measurements. The calibration needed for our purpose included checking for correctness in z height

measurements and that the tip is capable of measuring angles greater than the angles present in textured silicon wafer.

#### 4.2.1 Z-Height Calibration

For this purpose two different z-height calibration standards are used TGZ3 and TGZ4 bought from [34]. Their specification are shown in Fig. 33.

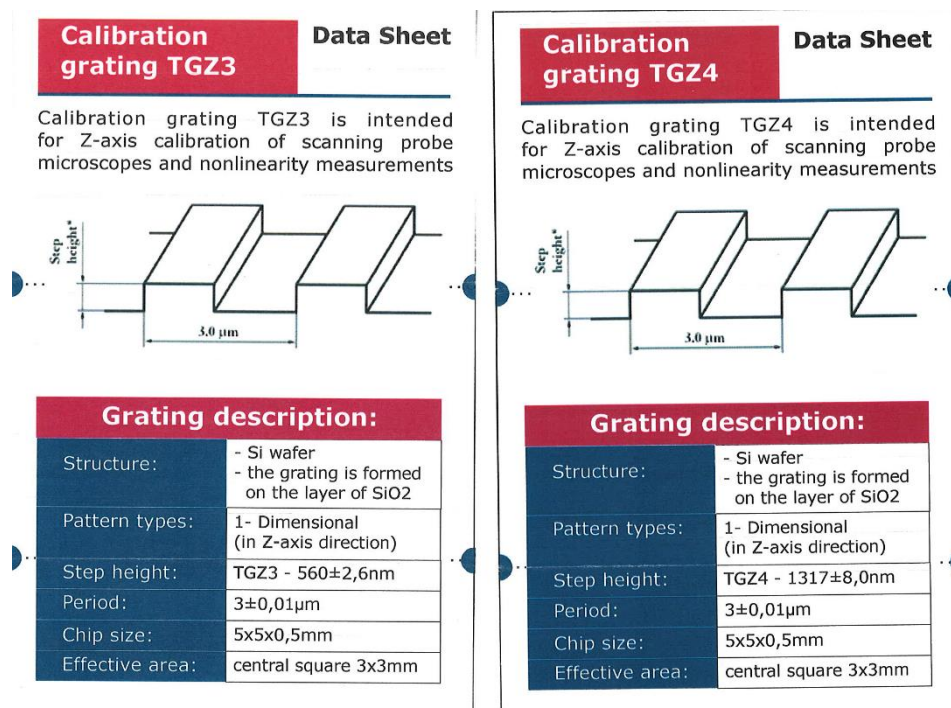


Figure 33 Z-Height Calibration Standards [34].

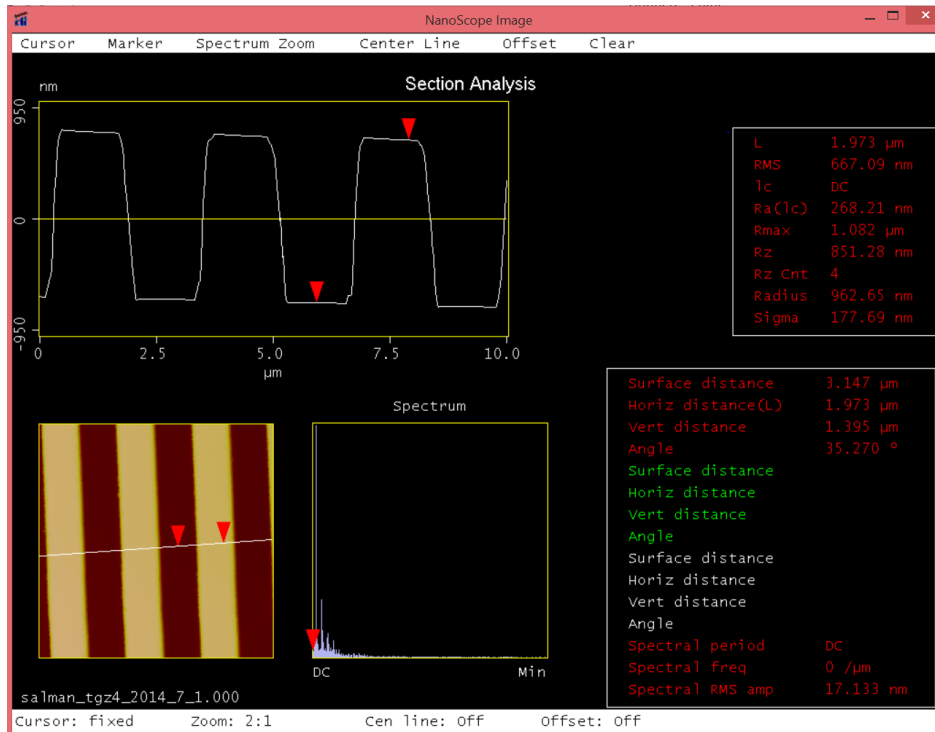


Figure 34 Section of TGZ4 Showing the Step Height = 1395 nm.

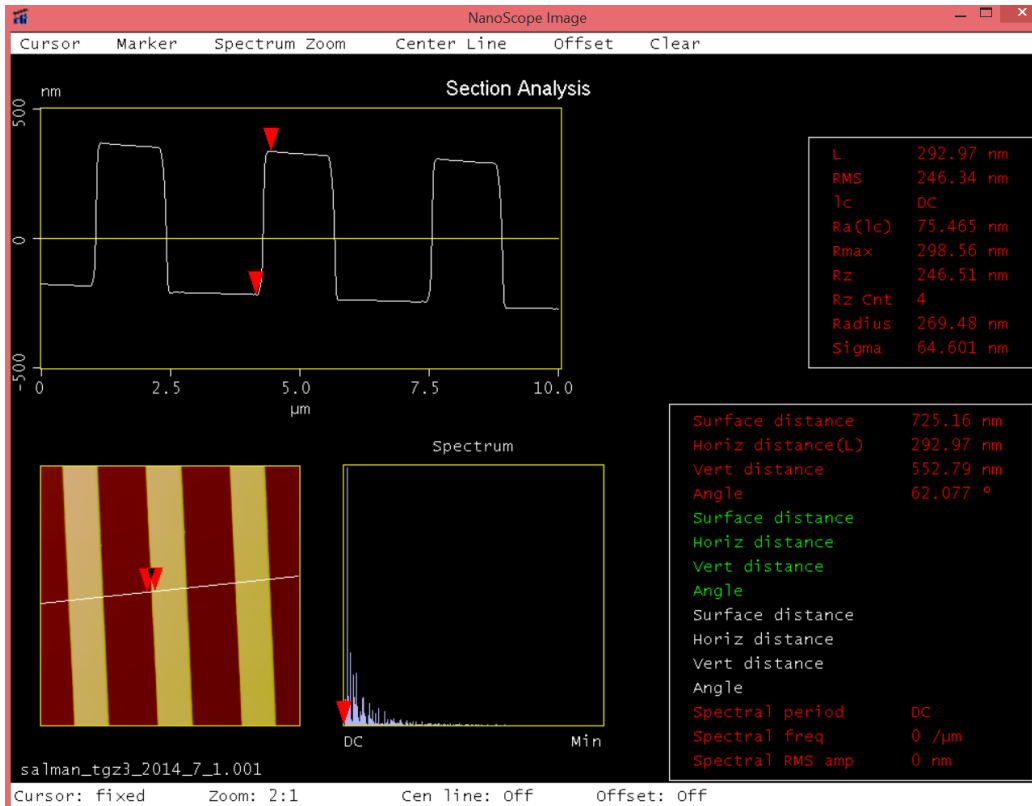


Figure 35 Section of TGZ3 Showing Step Height = 553 nm.

Fig. 34 and 35 show the section of measured AFM scan of TGZ4 and TGZ3 respectively, and it is shown that heights measured are correct.

#### 4.2.2 LARGE ANGLE MEASUREMENT

The tip used is a high aspect ratio tip, plus the features to be scanned have characteristic angle of  $54.74^\circ$  degrees, thus it is essential to be sure that with this tip it is possible to measure angles greater than this. Fig. 36 is a section of AFM scan of TGZ4 and it clearly shows the vertical edge of the step has approximately  $82^\circ$  degrees of angle, proving that with this tip we can measure considerably large angles sufficient for our application.

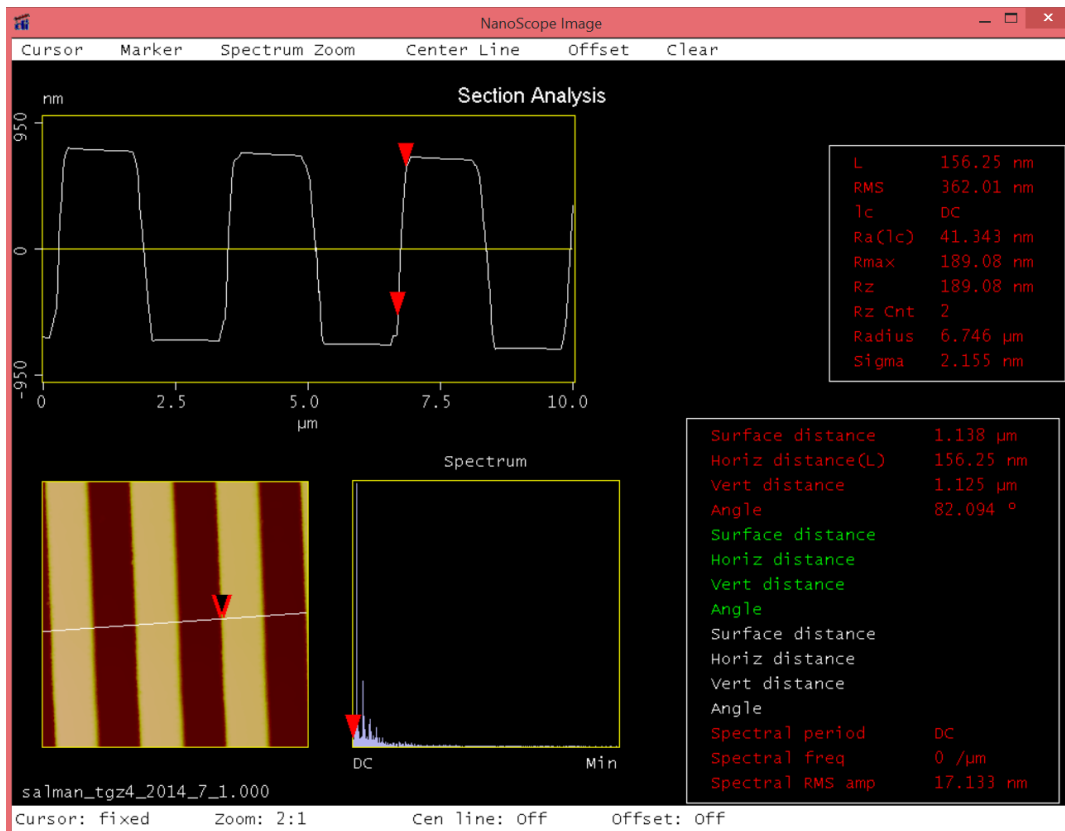


Figure 36 Section of TGZ4 Showing Angle of the Side of the Step.

### 4.3 Measured AFM Maps of Actual Textured Silicon Wafer

We have chosen a textured silicon wafer such that the z height of the pyramids doesn't exceed the z-range of the AFM machine that is used and also that the length of high aspect ratio portion of the tip is greater than the height of the pyramids. Thus, the pyramids have heights  $z < 2\mu\text{m}$ . Fig. 37 shows the scanning electron micrograph (SEM) of the textured wafer used in this work.

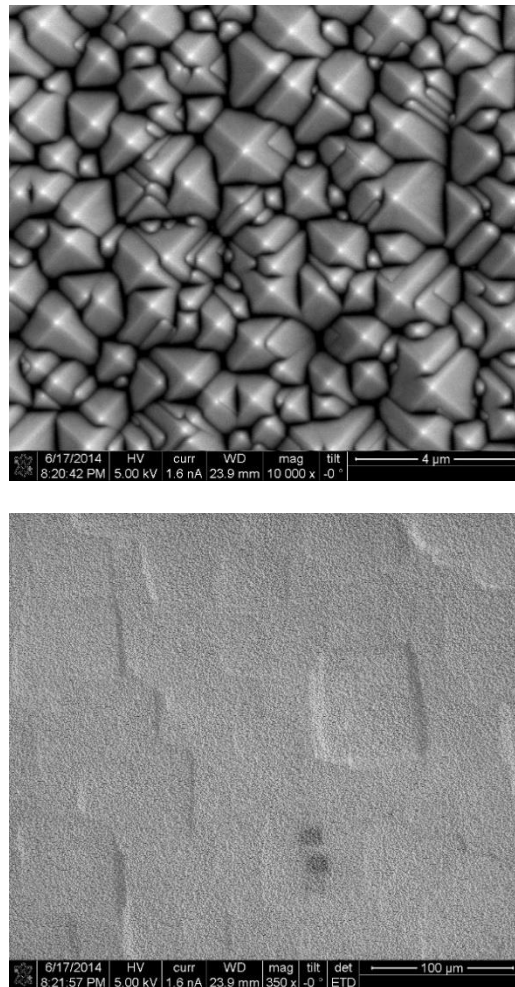


Figure 37 SEM Image of the Textured Silicon Wafer Used in this Work (Top) At High Magnification (Bottom) At Low Magnification.

Several height maps were measured with AFM of the textured wafer shown in Fig. 37, by changing the scan size and changing location to get the idea of variation in heights of pyramids and also the variation of their base angle. Fig. 38 shows two amplitude images as an example of AFM scans taken at different locations and with different size. Amplitude image is not a real height image with which topographical measurement could be performed. It is just for better visualization and to show what the texture looks like with AFM.

Actual height maps measured with AFM are shown in Fig. 39. Again, the maps are measured at different locations and also of different sizes. This is done so to get the measure of variance in height of pyramids and their base angle that comes with changing location. Only two maps are showed in Fig. 39 for which the greatest difference in base angle was observed, one is called Map 1 and other is called Map 0. For these two maps the height distribution is plotted as well as distribution of base angle of pyramids in Fig. 40. Based on the measured maps it is noticed that the height distribution looks the same in all maps whereas for the base angle distribution the peak position shifts a little and the shift is noticed to be not more than  $4^\circ$  degrees. This shift could be attributed to the small size of the map that fails to capture over all general base angle distribution but still captures the positional randomness of the pyramids' peak positions and heights. The size of the map is limited by the number of points that could be scanned per line using this AFM. So, for the AFM used in this work the map of 512-by-512 points can be constructed and that's the maximum resolution irrespective of the size of area scanned.

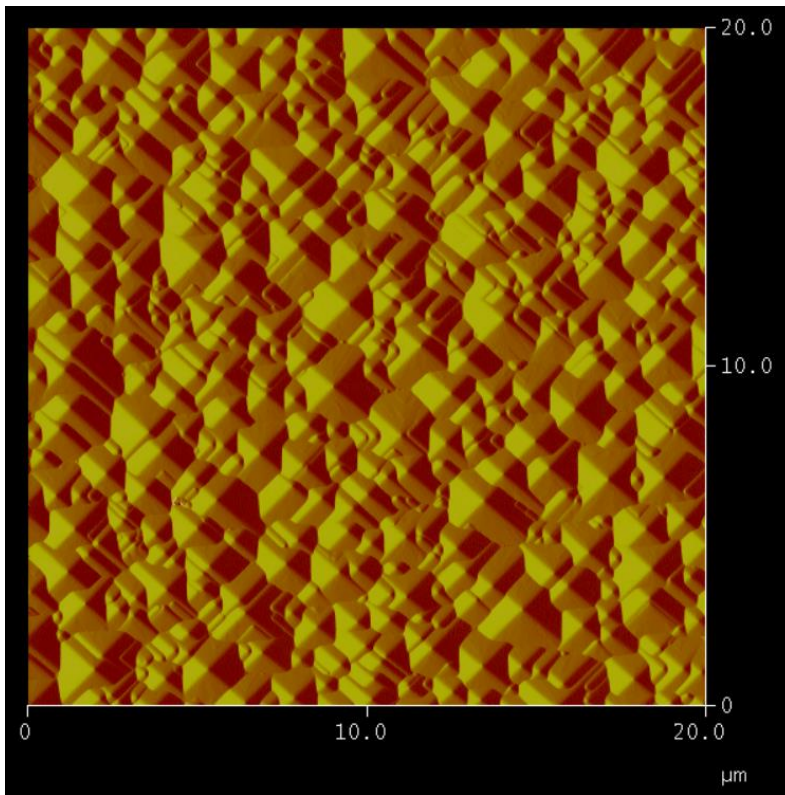
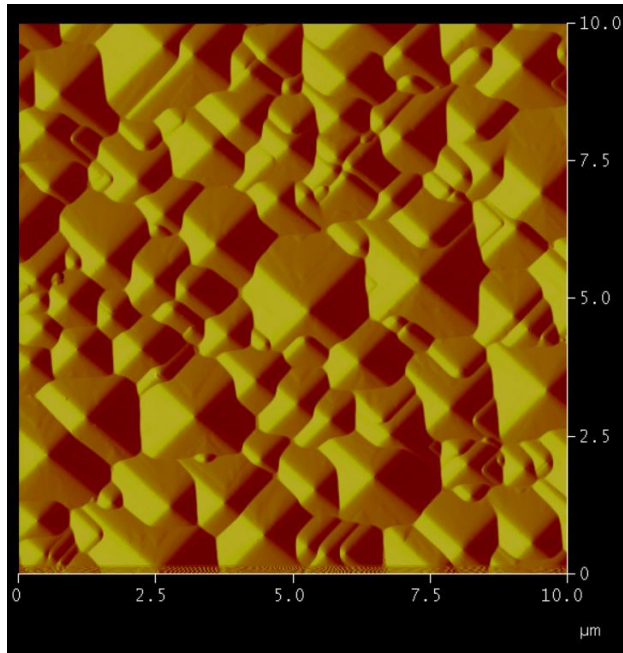


Figure 38 (top) Shows a Small Area Scan, (Bottom) Shows Large Area Scan of a Different Location.

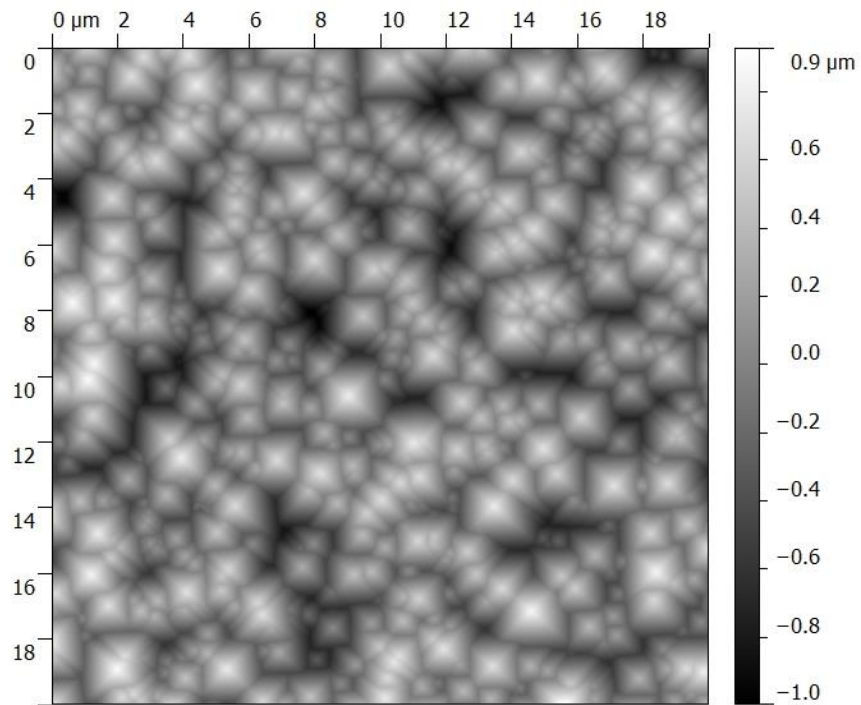
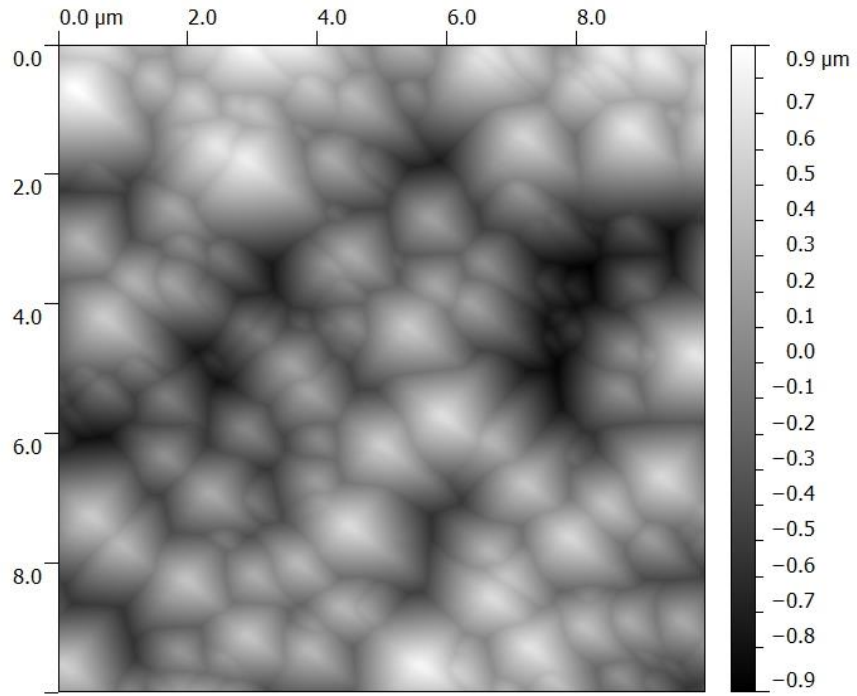


Figure 39 Measured AFM Maps, (Top) is Map 1 with Area of 10-By-10 Square Microns, (Bottom) is Map 0 and it's Area Is 20-By-20 Square Microns.

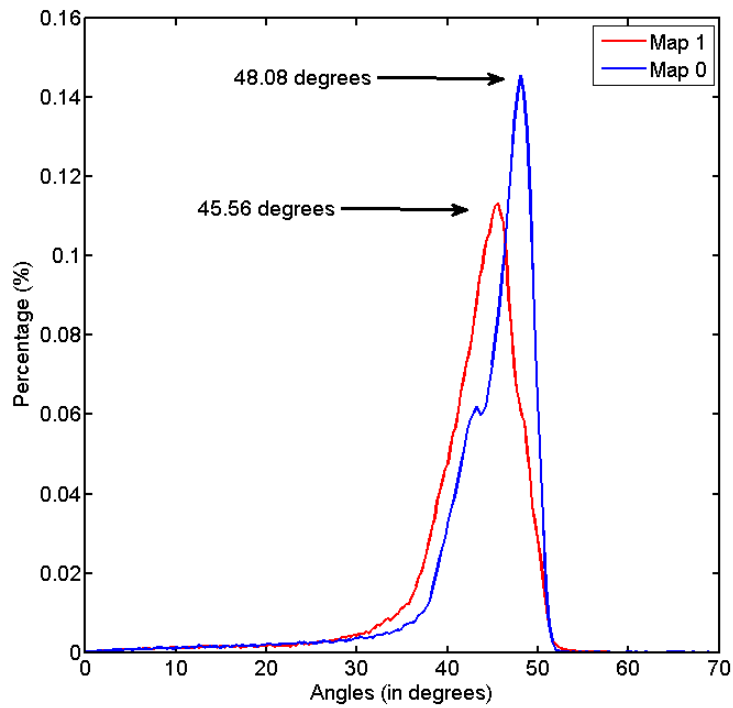
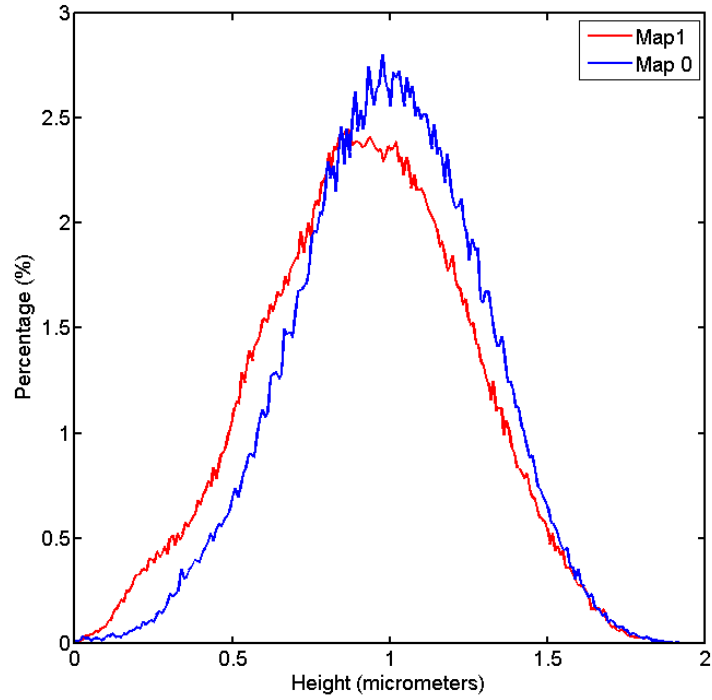


Figure 40 (Top) Graph Shows the Comparison of Height Distribution, (Bottom) Graph Shows the Comparison of Base Angle Distribution.

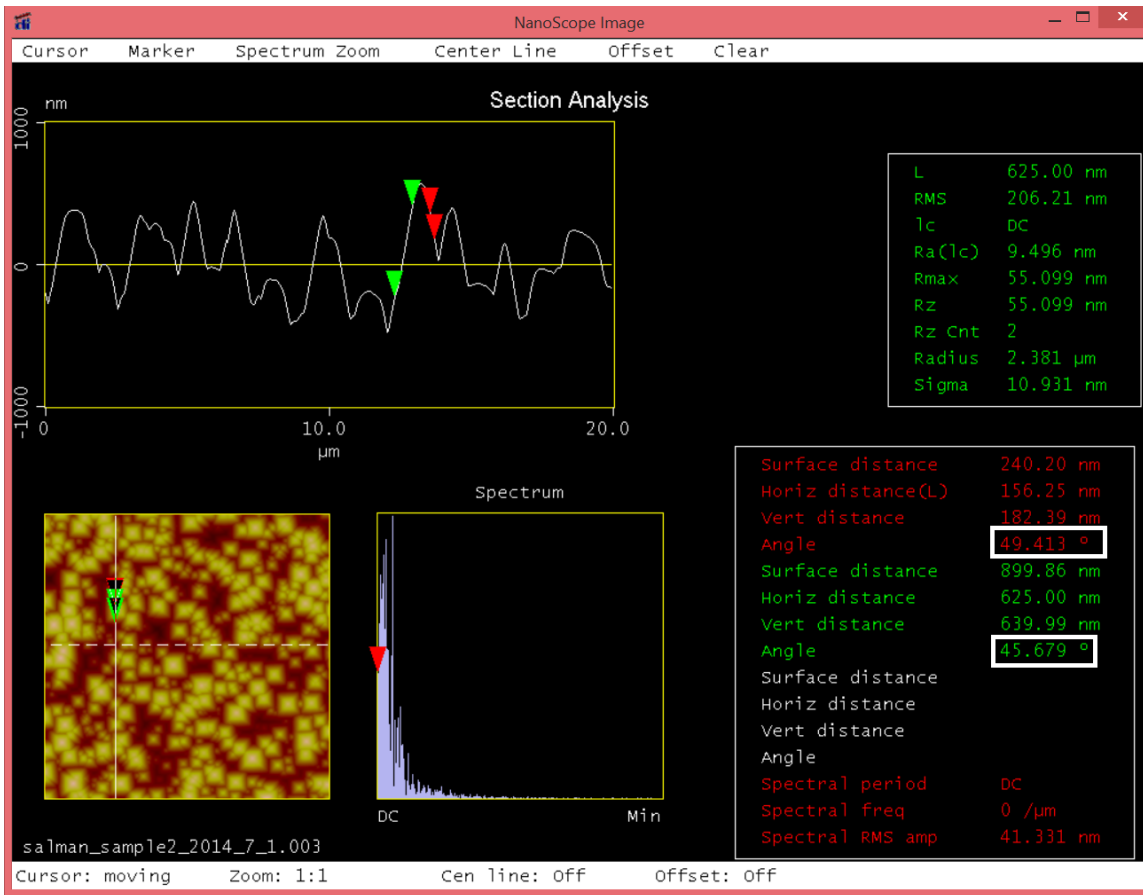


Figure 41 Angle Comparison of Pyramid Facets.

The second peak in the base angle distribution of Map 0 in Fig. 40 could be explained using Fig. 41. A sample section of the Map0 is shown. The angles of two facets of the same pyramid are shown with the help of markers. One facet has red markers and the other has green markers. The calculated angles are shown in the right bottom corner inside the white rectangles. The angle between the red markers is 49.41 degrees and between the green markers is 45.68 degrees. This is approximately the same position as the two peaks of base angle distribution of Map0. This could be the result of a tilt of sample during the AFM measurement.

#### 4.3.1 Validation of Measured AFM Maps

There are two ways of judging that the measured AFM maps accurately represent the actual texture. The first method is to actually compare the density of peaks (that is peaks per unit area) in the AFM map with an SEM image. For this comparison the total number of peaks are found using a MATLAB code and then divided by the size of the map in microns. For comparison purpose a test texture is also included to show that for a different texture the metric, peaks per unit area gives a completely different value. For comparison AFM Map 1 (shown in Fig. 39) is selected. Fig. 42 shows the measured AFM Map 1 before peak detection and after, and similarly for the same sample (the sample that is used to get AFM Map 1) its SEM image before detected peaks and after and lastly it shows the test texture.

Table 2 Validation of AFM Maps by Calculating Density of Peaks.

	Peaks per unit area (peaks per micron)
AFM (Map 1)	1.4
SEM (of wafer used in this work)	1.3701
Test texture	0.1694

Clearly, the values for density of peaks in Table 1 show that the AFM map indeed is a correct map of textured wafer under study.

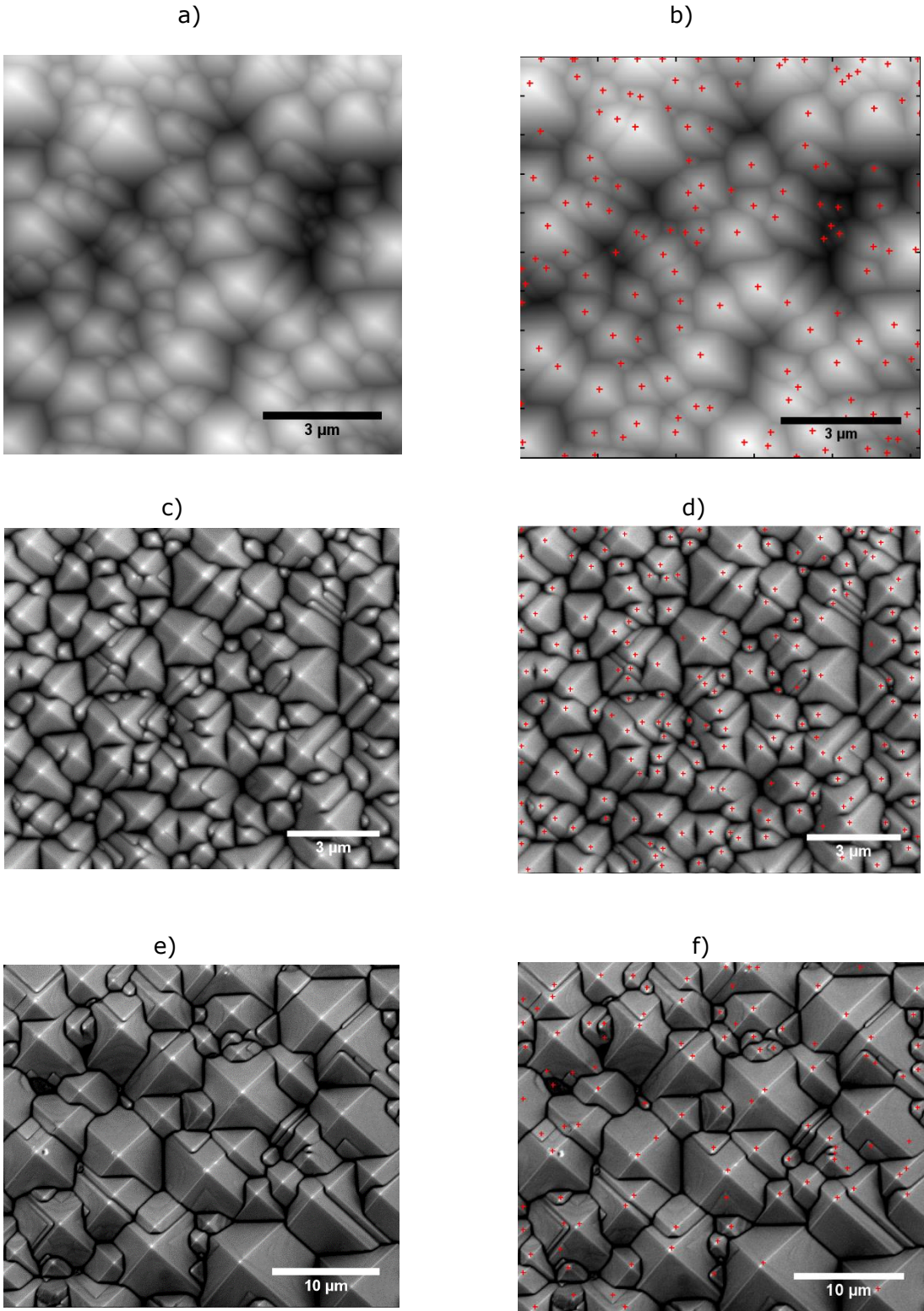


Figure 42 a) is Measured AFM Scan (Map1) b) AFM Scan with Peak Detection c) it is the SEM of Wafer Used for AFM, before Peak Detection D) SEM Image After Peak Detection E) SEM of Test Texture F) Test Texture After Peak Detection.

Second, method used for validation involves using the angular resolved reflectance (ARR) from the front surface obtained with spectrophotometer for the actual wafer that is used to get the AFM maps. It is shown by Baker et al. in [32] that the peak of the angular resolved reflectance distribution ( $\theta_r$ ) is related to the characteristic angle or base angle ( $\alpha_b$ ) of pyramids according to Eq. 4.1.

$$\theta_r = 4\alpha_b - 180 \quad \text{Eq. 4.1}$$

The angular resolved scattering from front surface of textured wafer is experimentally found using the Automated Reflectance and Transmittance Analyzer (ARTA) built by OMT Solutions [31]. It is shown in Fig. 43.

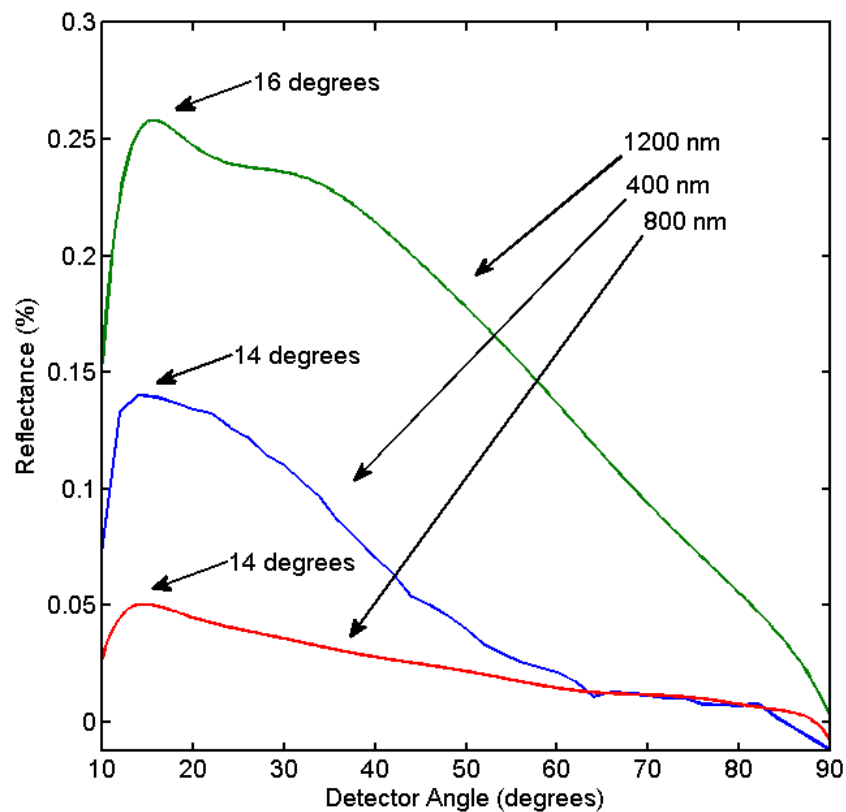


Figure 43 Angular Resolved Scattering Distribution from Front Surface of Textured Wafer.

The peak of ARR distribution for textured wafer occurs at detector angle of approximately at  $14^\circ$  degrees. Putting this value in the Eq. 4.1 gives the dominant base angle ( $\alpha_b$ ) of pyramids for texture considered in this work to be equal to  $48.5^\circ$  degrees. This is a perfect match with the base angle of Map 0 (shown in Fig. 39) for which its  $\alpha_b$  distribution is shown in Fig. 40. It is also within  $4^\circ$  degrees as mentioned before for Map 1. This validates that the maps measured with AFM are correct in terms of positional randomness, height and accurately capture the base angles. For further analysis Map 1 is chosen as it gives lower base angle and should have poorer reflectance than Map 0, so the argument is if Map 1 achieves lambertian limit, surely Map 0 would too.

Third, and last validation method involves milling the sample using focused ion beam of Gallium ions. It was done with FIB-SEM dual beam Nova 200 Nanolab by FEI. It has two beam chambers, one for electrons that renders SEM images and second is for Gallium ions used for milling the substrate. On this machine sample can be engaged eucentrically which means Gallium beam and electron beam can point at the same point of the wafer. Therefore, milling and imaging of the same point is easily accomplished. To reach eucentric point the stage on which the sample rests is tilted for  $52^\circ$  degrees at which point the Gallium and electron beams become coincident and are at  $45^\circ$  degrees to each other. It is shown in Fig. 44.

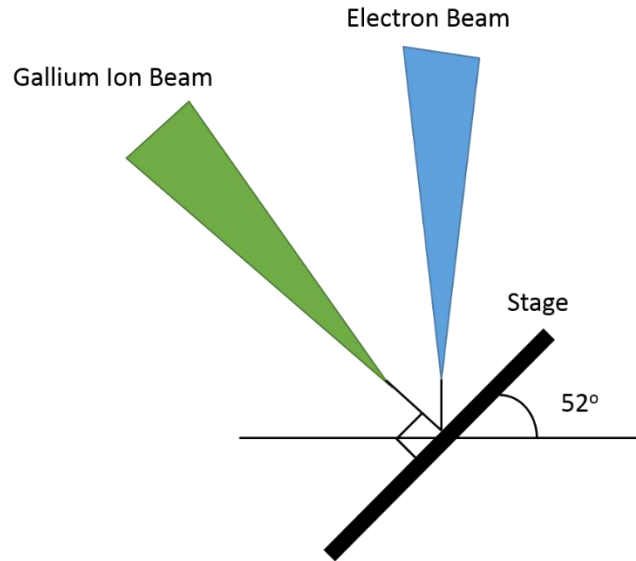


Figure 44 Eucentric Tilting.

Once eucentric tilting is achieved then a pattern is defined to deposit platinum to protect the edges of the sample that would get exposed after milling. After that a new pattern is defined to mill the desired area. The example of this process is shown in Fig. 45.

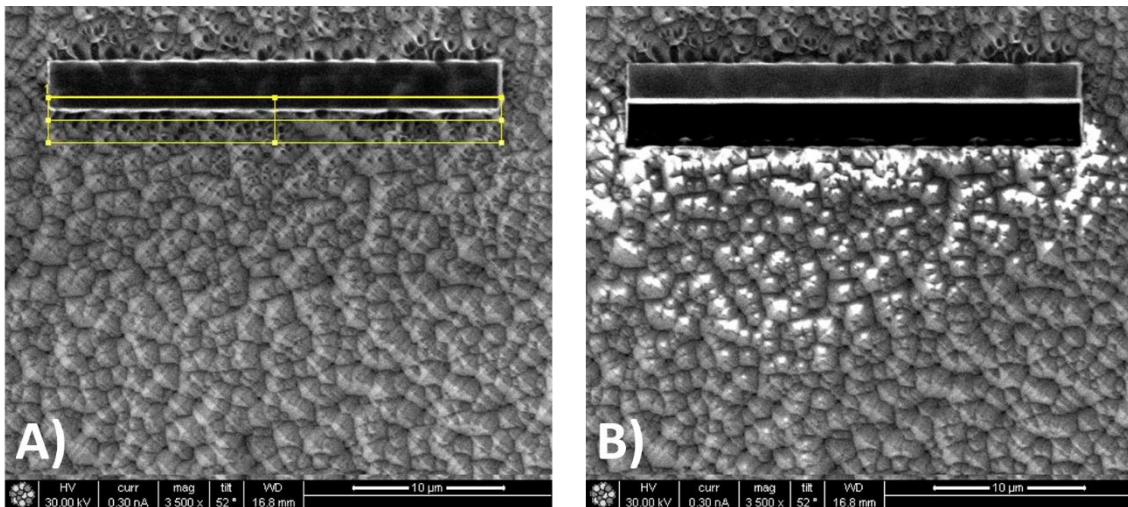


Figure 45 It is an Ion Image. A) Shows the Deposited Platinum and Yellow Rectangle Shows the Pattern for Milling, B) It Shows the Image After Milling.

After milling using an electron beam SEM image of the milled area is taken. It must be remembered that electron beam is not perpendicular to the stage but at a certain tilt. So, after milling the profile of pyramids is exposed and deposited platinum provides a nice contrast for viewing the profile. It is shown in Fig. 46.

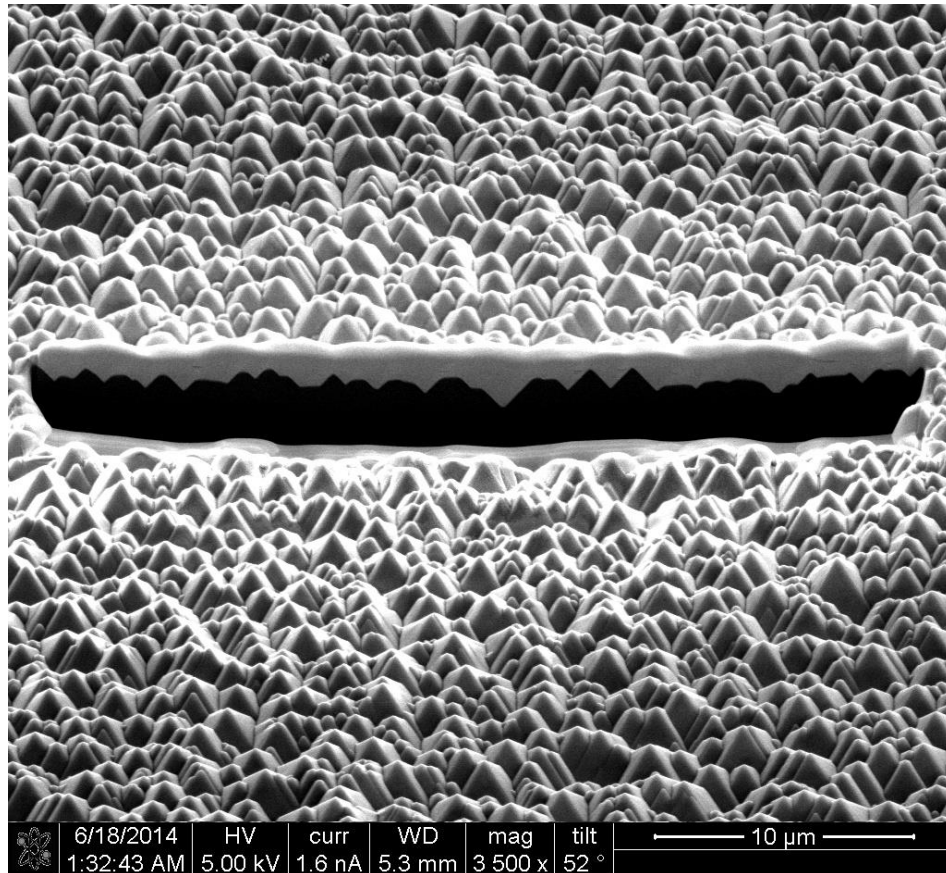


Figure 46 SEM Micrograph After Milling. Dark Area is the Cross Section that has been Exposed due to Milling. White Area Above the Dark Area is the Deposited Platinum.

After this at high magnification several pictures are taken of the cross section. Using small steps moving left to right at high magnification the SEM images of whole of cross section are recorded. This is done so because it is a digital image and calculating directly from Fig. 46 gives back very few pixels for the pyramids' boundary and thus the error in angle calculation is large. Example of high

magnification pictures are shown in Fig. 47. In the next step a code written in Matlab is used to detect these boundaries and angles are calculated. Fig. 48 shows the detected boundaries. In Fig. 49 for the profiles detected the dominant angles are shown.

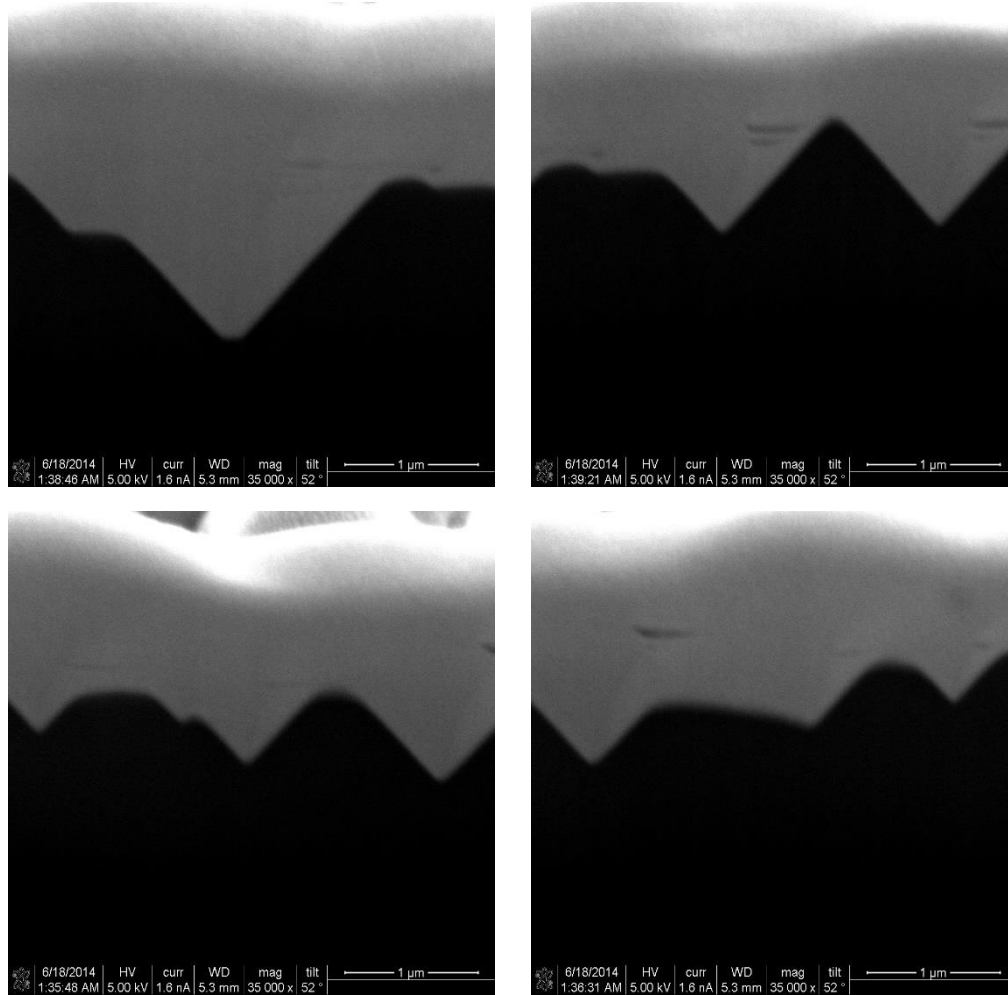


Figure 47 SEM Micrograph of the Cross Section at High Magnification.

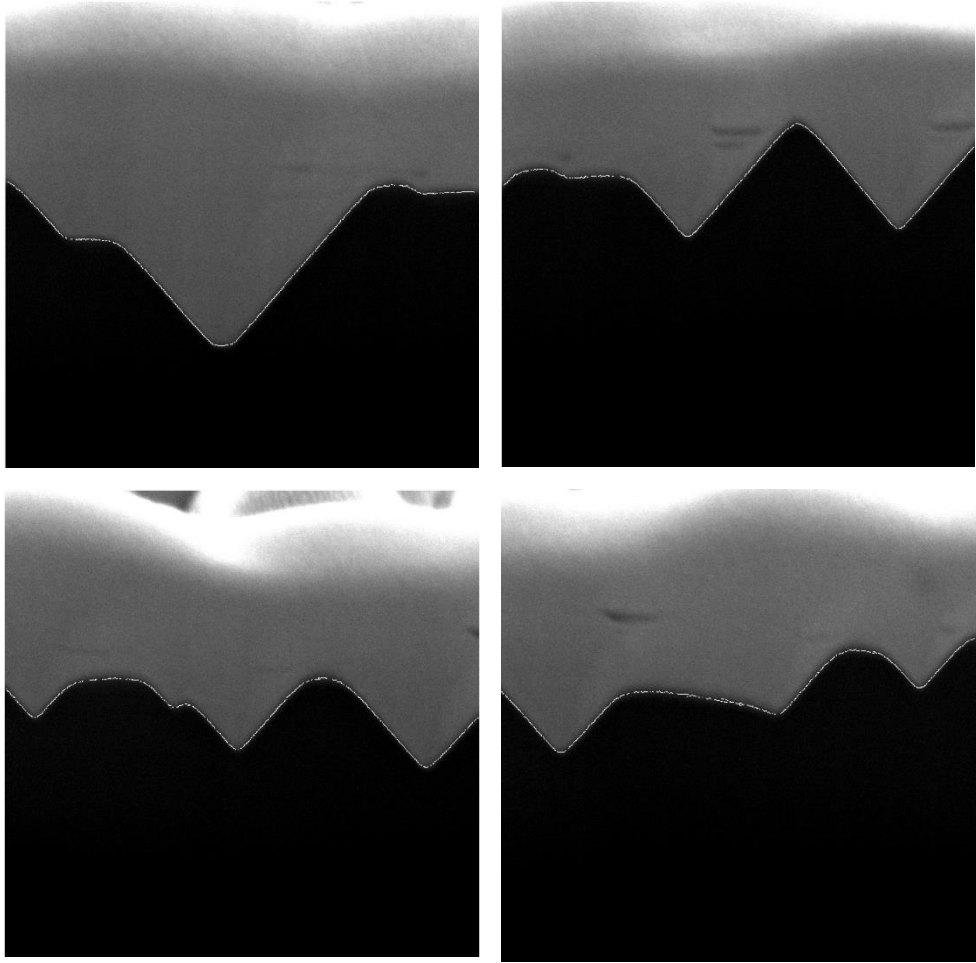


Figure 48 Detected Profiles in the SEM Micrographs shown in Fig. 47.

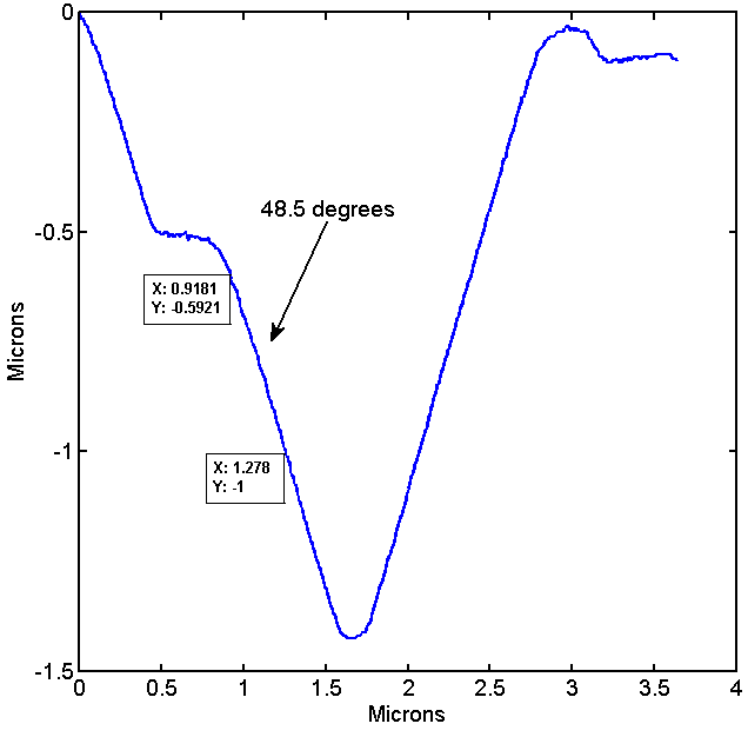
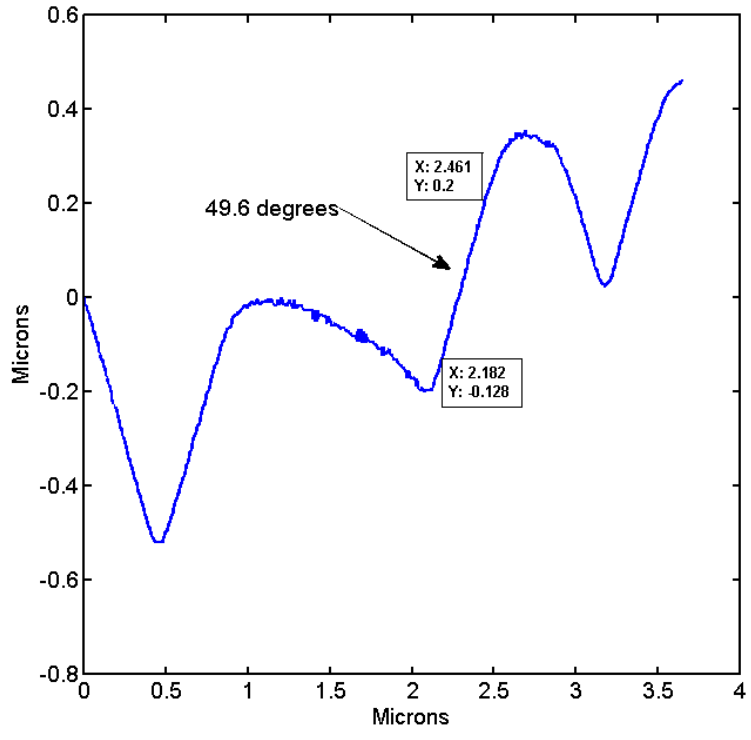


Figure 49 Dominant Angle shown as an Example from Profiles from Fig. 48.

So, numerous slices such as shown in Fig. 46 are milled and the profiles extracted but first the flat portions in the profiles are taken out. They are then put together to calculate the angle distribution. Fig. 50 shows the base angle distribution calculated with FIB versus calculated from AFM maps. For FIB the distribution is centered at 50 degrees which is in good agreement with AFM distribution considering it is calculated from a digital image that has quantization error.

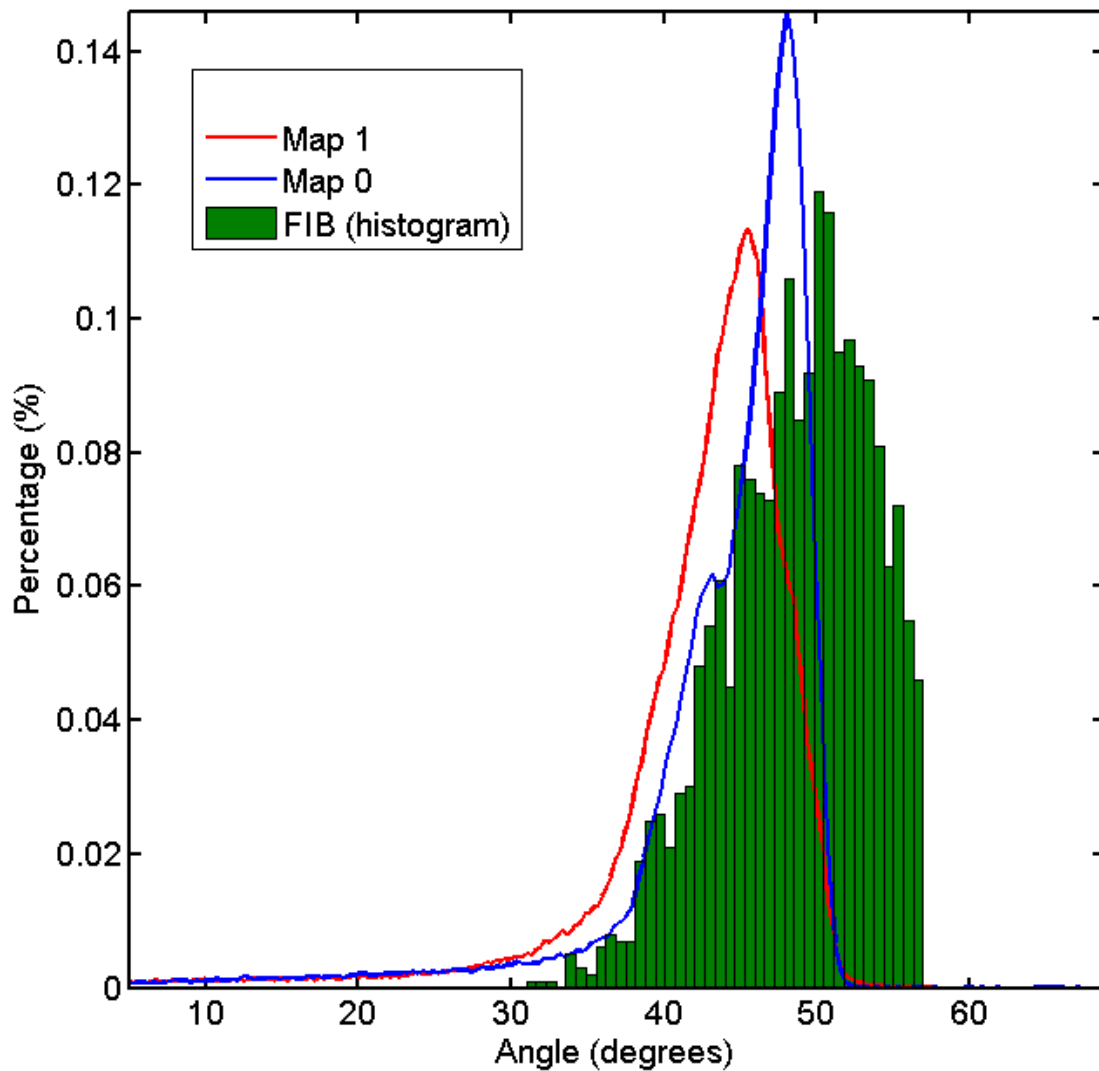


Figure 50 Shows Base Angle Distribution Calculated with FIB Versus AFM.

#### 4.4 Manipulation of Measured AFM Map to Get a Map with Arbitrary Angular Distribution of Base Angles

In order to investigate the effect of base angle distribution on reflection, absorption, transmission and angular resolved scattering it is important to be able to modify the obtained AFM map shown in previous section. The purpose is to compare the light trapping of measured AFM map versus the modified maps that have different base angle distributions. Furthermore, the comparison of measured and modified maps is to be performed with lambertian scatterer. The modification has to be such that it retains the positional randomness of the peaks and as well as their heights. So, that alone the effect of changing the base angle distribution could be investigated. For this purpose the strategy is to design an algorithm that could first identify the peaks in the current AFM map and store their peak positions. Then, the heights of those peaks are read and saved along with their peak positions. After that to construct new pyramids with different facet angle, the strategy is to first read the position and the height of the peak ( $z$ ), after that  $dx$  and  $dy$  are found using the physical size of the map which is known and the resolution of the map that is 512-by-512 points. Size of the map divided by 512 gives the distance between each grid point called  $dx$  or  $dy$  depending on the direction. Now, we already have a starting  $z$  height which is the height of the peak, and we need to calculate the  $dz$  (change in height at each point as we move away from peak position) using the required base angle already given by the user. So, the formula becomes  $dz/dx = \tan(\alpha_b)$ . Once  $dz$  is found, then to construct a pyramid, eight neighboring points to peak position are selected and the height value to be placed there is  $dz$  less than the peak height. After this next outer ring of grid points is selected and the value of height to be placed there is  $2*dz$  less the peak height. In this fashion the pyramid of arbitrary

facet angle can be constructed. This process is carried out for all the peak positions in their respective 512-by-512 planes. Then all these planes are projected onto a final plane of size 512-by-512 and the condition is for final plane is that the height value to be placed at any grid point would be the maximum value of height at that point in all the separate planes of peaks. Using this method a map could be constructed where all pyramids have a same base angle. In this work such a map is referred to as fixed angle map. To create a map with normal distribution of base angles, the strategy is to define each pyramid as having a different base angle and thus by controlling the number of pyramids for each base angle, a normal distribution is constructed. Such a map in this work is referred to as normal distribution map centered at a particular angle.

Using this approach several maps are constructed using an AFM Map 1.

Table 3 contains the names of maps constructed and their description.

Table 3 List and Description of Maps

Name of Map	Description	Resolution (points)	Area of a Map ( $\mu\text{m}^2$ )
Map 1	It is the original AFM Map 1.	512-by-512	100
Map 2	Fixed angle = 45.54 degrees	512-by-512	100
Map 3	Fixed angle = 50 degrees	512-by-512	100
Map 4	Fixed angle = 54.7 degrees	512-by-512	100
Map 5	Fixed angle = 45.54	1024-by-1024	400
Map 6	Fixed angle = 50	1024-by-1024	400
Map 7	Fixed angle = 54.7	1024-by-1024	400

Map 8	Normal distribution, center = 44.82 degrees	1024-by-1024	400
Map 9	Normal distribution, center = 50 degrees	1024-by-1024	400
Map 10	Normal distribution, center = 54.7 degrees	1024-by-1024	400

To make maps with normal distribution of  $\alpha_b$  requires large number of pyramids so that there are pyramids of each angle in the map. This requires that Map 1 which is 100 sq. microns in size be replicated in such a way that there are no discontinuities and there be no change in positional randomness. So, to build bigger map from a small map (that is Map1) the peak positions and their height and their relative positions with respect to each other are copied in a fashion shown in Fig. 51. After that the pyramids are grown into each other removing discontinuity due to copying.

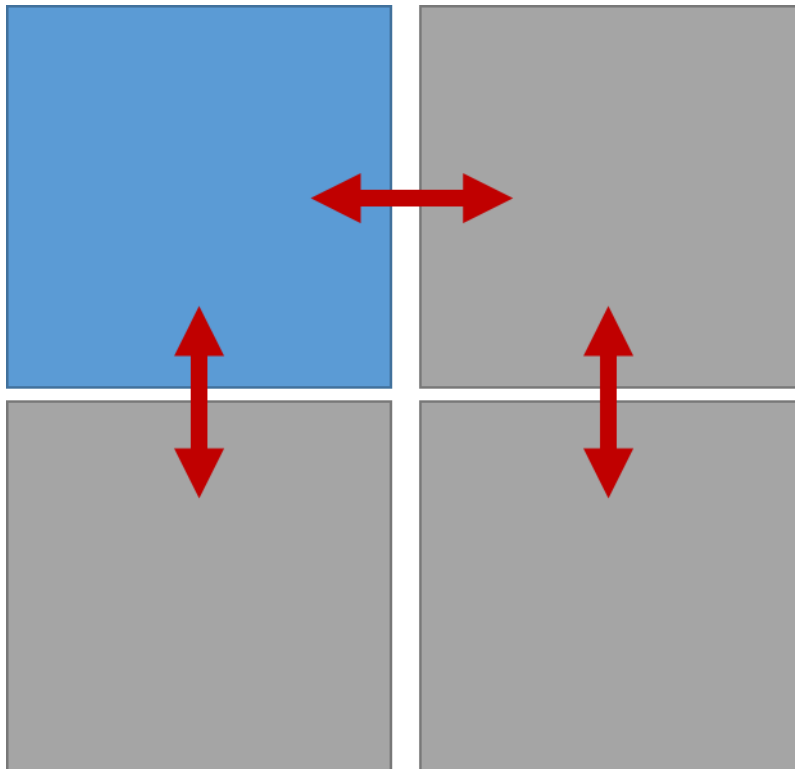


Figure 51 Process Shows how a Bigger Map is made from Small Map. Blue Square Represents Original Map. The Grey Ones Show they are copies of Blue. After, that Pyramids are Let to grow into each other Removing Boundaries.

So, these maps differ from each other in terms of their angular distribution of base angles. For the sake of clarity and reasons explained in the next section they are grouped as maps with fixed angle distribution (Map 2, 3 and 4) and maps that have bigger area ( $400 \mu\text{m}^2$ ) (Map 5, 6, 7, 8, 9, 10, 11). Fig. 52 shows the angular distributions of all the maps that have fixed angles and Fig. 53 is for all the maps with area of  $400 \mu\text{m}^2$ .

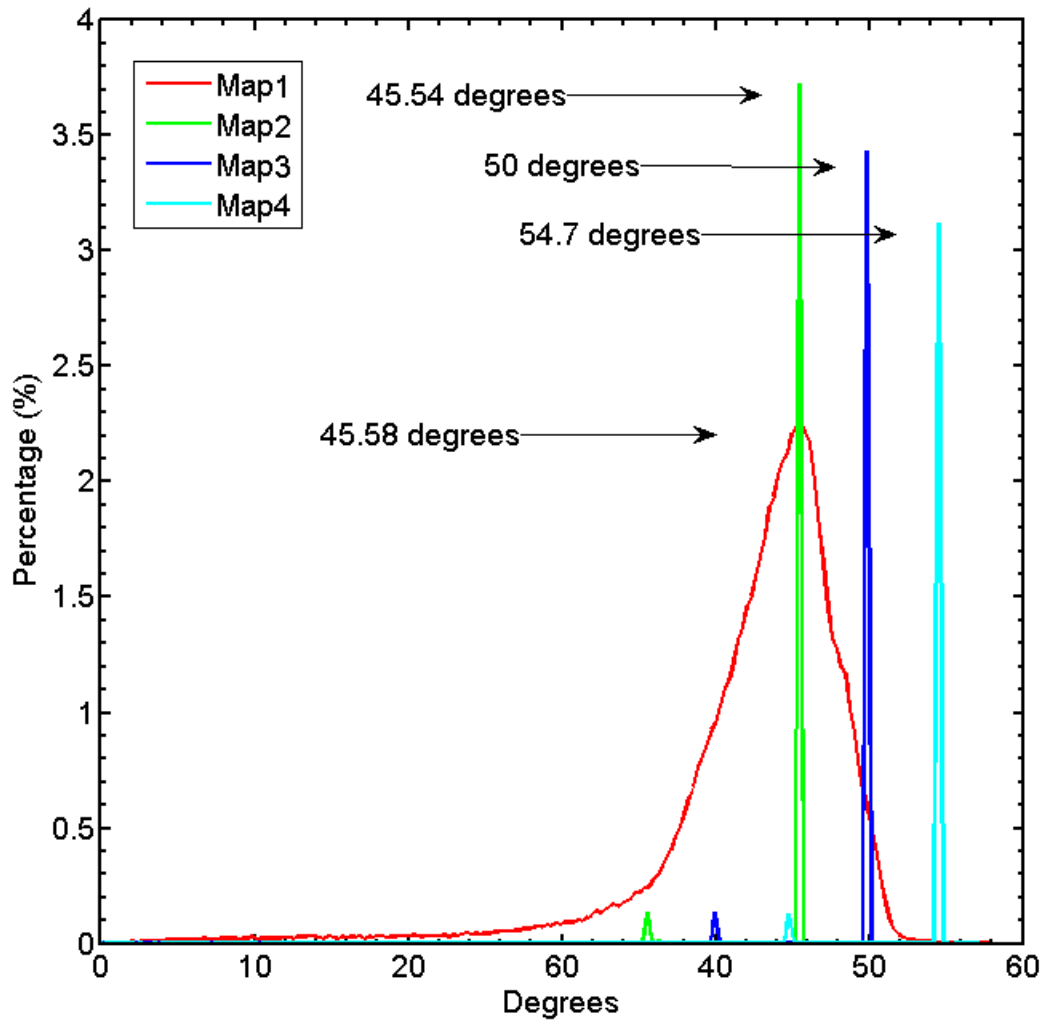


Figure 52 Angular Distribution of Base Angles for Fixed Angle Maps. Map 5, 6 and 7 are not Represented in the Plot because they have same Curve as Map 2, 3 and respectively. Map1 is the Distribution for Measured AFM Scan.

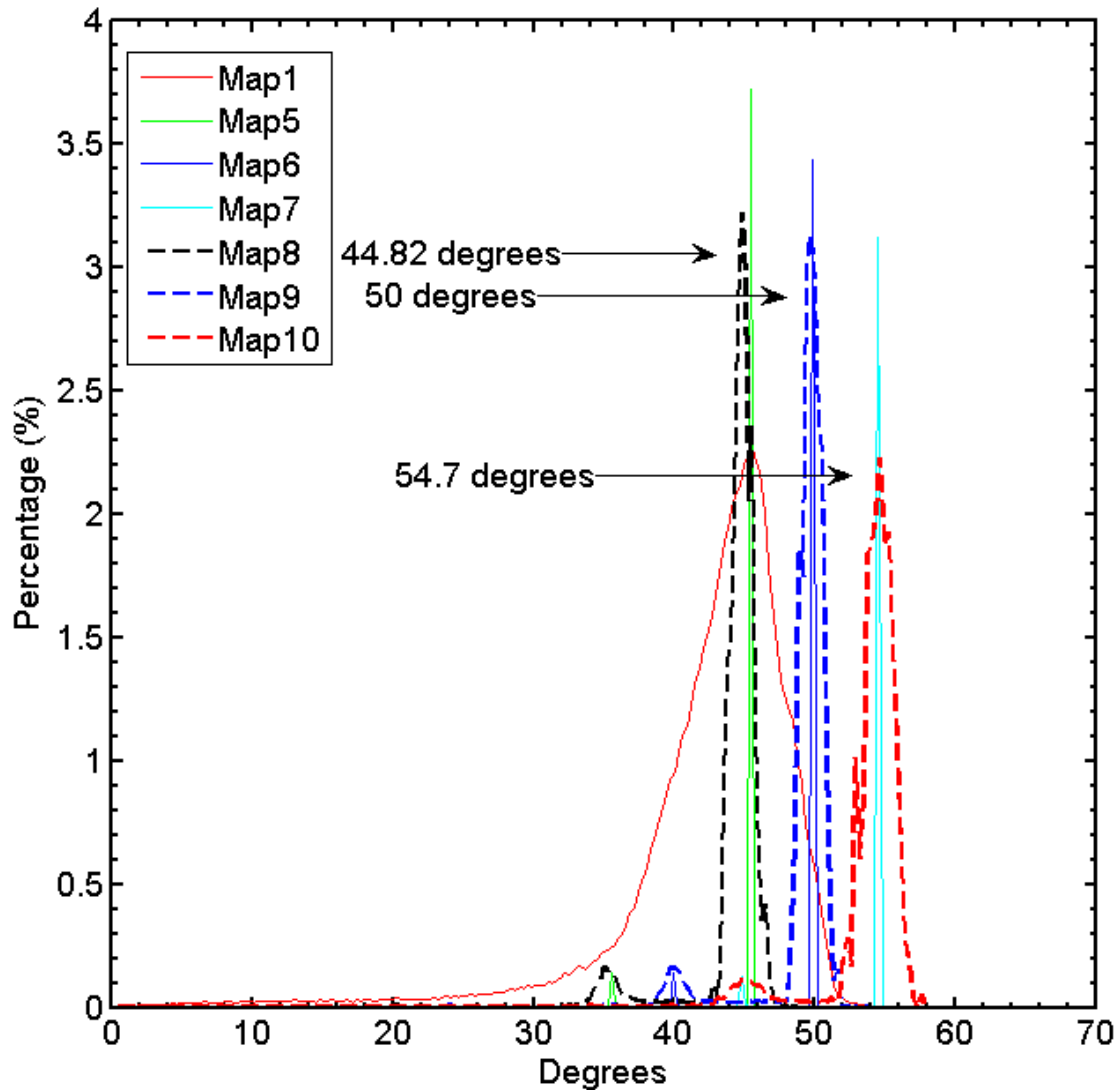


Figure 53 Angular Distribution of Base Angles for all the Maps with Area = 400 Square Microns. Plot shows Fixed Angle and Normally Distributed Base Angle Distributions. Map1 is the Distribution for Measured AFM Scan.

Finally, the maps are shown in Fig. 54, 55 and 56. They are shown in three different figures for the reason it is difficult to fit them in one figure. Plus, they are grouped. Fig. 54 shows Map 1, 2, 3 and 4, and as mentioned before Map 1 is measured AFM map, and the map 2, 3 and 4 maintain the peak heights and positions but change the  $\alpha_b$  of all the pyramids so that all of them have the same fixed base angle.

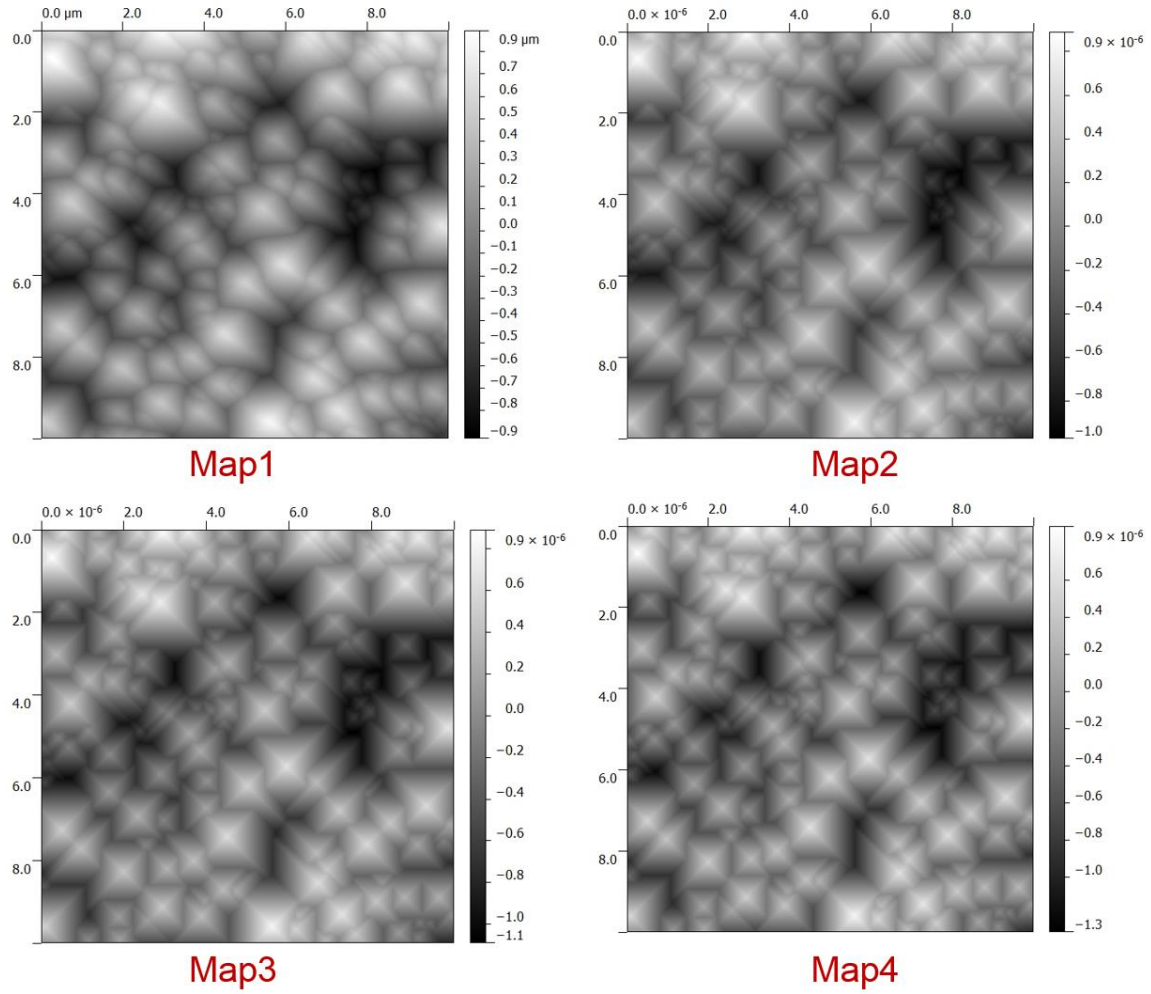
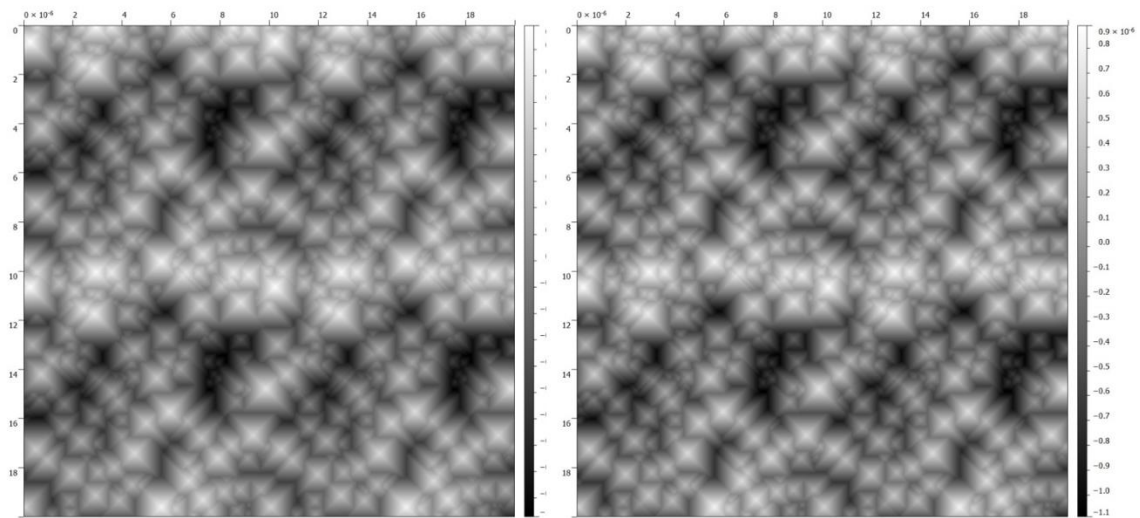
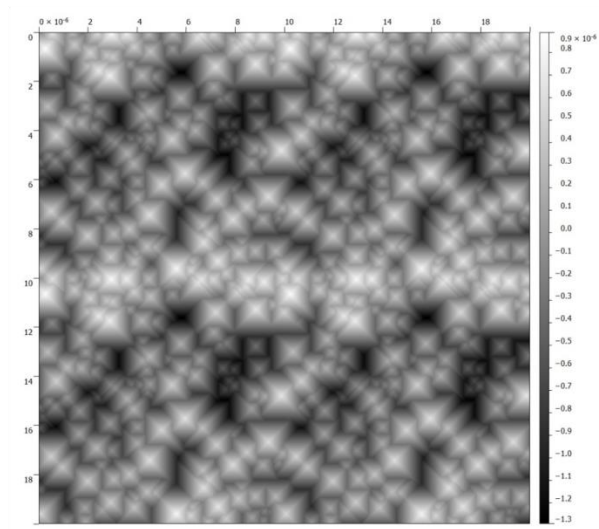


Figure 54 Measured AFM Map and Modified Fixed Angle Maps. All Maps are 512-by-512 in Resolution and have Area Size 100 Sq. Microns.



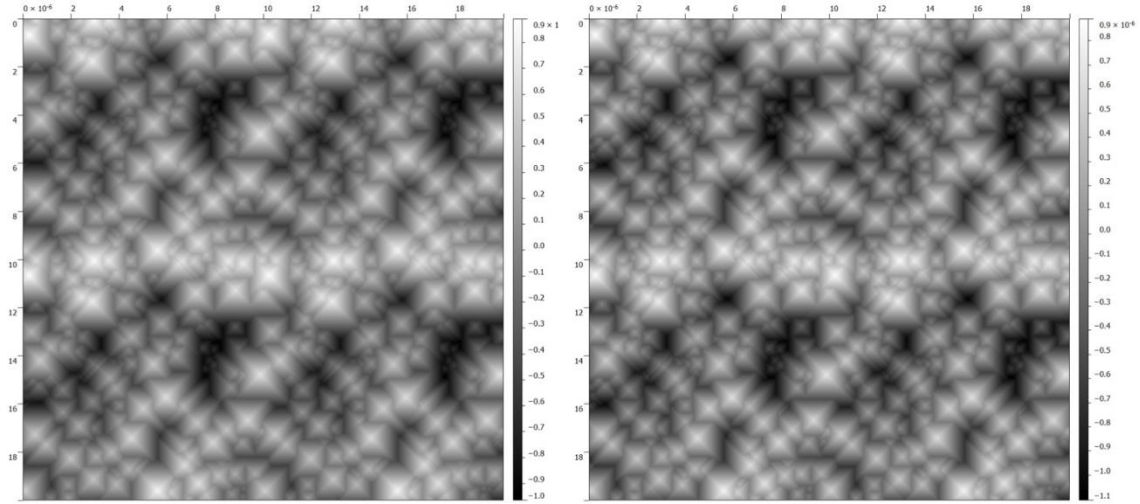
Map5

Map6



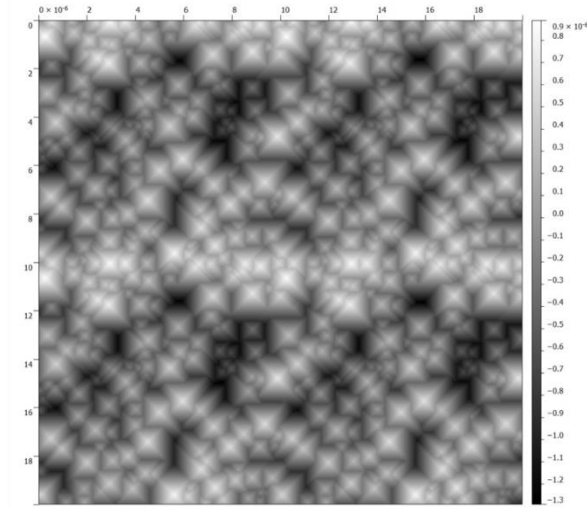
Map7

Figure 55 Modified Fixed Angle Maps with Increased Area Size. Map 5 has same Fixed Angle as Map 2. Same is the Relationship between Map 6 and Map 3, Map 7 and Map 4. All Maps are 1024-by-1024 in Resolution and have Area Size 400 Sq. Microns.



Map8

Map9



Map10

Figure 56 Modified Maps with Normally Distributed Base Angle Distribution. All Maps are 1024-by-1024 in Resolution and have Area Size 400 Sq. Microns.

The large versions of all the maps are given in Appendix A at the end.

#### 4.4.1 Roughness Comparison of the Maps

The most popular way of comparing roughness of surfaces is by calculating their average roughness ( $R_a$ ) and root mean square roughness ( $R_q$ ).

Roughness average ( $R_a$ ) is basically the arithmetical mean average. The average deviation of all points' roughness profile from a mean line over the evaluation length. Eq. 4.2 shows the formula for calculating  $R_a$ .

$$R_a = \frac{1}{N} \sum_{j=1}^N |r_j| \quad \text{Eq. 4.2}$$

Root mean square roughness ( $R_q$ ) is the average of the measured height deviations taken within the evaluation length and measured from the mean line. It is given by Eq. 4.3

$$R_q = \sqrt{\frac{1}{N} \sum_{j=1}^N r_j^2} \quad \text{Eq. 4.3}$$

These roughness parameters were calculated for all the maps using Gwyddion [35] which is an open source software available freely online. Table 4 shows the results for roughness. It can be seen that changing the base angle changes the roughness while normally distributing the base angle has little effect on the roughness.

Table 4 Evaluation of Roughness of the Maps.

Name of the map	Roughness Average ( $R_a$ ) (in microns)	Root mean square roughness ( $R_q$ ) (in microns)
Map1	0.260	0.321
Map2	0.250	0.311
Map3	0.269	0.333
Map4	0.293	0.364
Map5	0.252	0.312
Map6	0.271	0.335
Map7	0.296	0.366
Map8	0.250	0.310
Map9	0.271	0.335
Map10	0.296	0.366

## 4.5 Optical Simulations

Optical simulations for these maps were done in an optical simulator called CROWM [36] that previously has been used to study the optical properties of solar cells [37][38]. CROWM is capable of doing three dimensional incoherent ray tracing based on geometric optics. CROWM is used in this work for ray tracing to obtain angular distribution of reflection from the front surface and as well as total reflection from the front, transmission and absorption in the bulk, also obtained are results for angular distribution of light that enters the silicon substrate from the front surface. All these simulations were done with the structure air-silicon-air and same texture (the maps) were applied to the top and back surface. The thickness of silicon was assumed to be 180 microns.

### 4.5.1 Effect of Map Area on Reflection from Front Surface

The first thing investigated using CROWM is the effect of changing the size that is area of the map while keeping the base angles fixed. As mentioned earlier, Map 2 and Map 6 have the same base angle for all the pyramids (the base angle is 45.54 degrees – details of all the maps are given in Table 3) but the maps vary in size. Map 2 has an area of 100 sq. microns and Map 6 has an area of 400 sq. microns. In previous section it has been explained how the area of the map is increased. Similarly, Map 3 and Map 7 are related and base angle of pyramids is 50 degrees. Pyramids in Map 4 and Map 8 have base angle of 54.7 degrees. The results for total reflection from them maps is given in Fig. 57. Between Map 2 and 5, there is a difference of about 1.14 % in reflection (calculated at 1000nm wavelength) and for Map 3 and Map 6 the difference is about 0.66% (calculated at 1000nm wavelength)

and when base angle is 54.7 that is for Map 4 and Map 7, the difference in reflection is almost zero. It is concluded when base angle becomes large it dominates the effect of changing the area of the maps. Since, large area maps show lower reflectance than small area maps so for further simulations only large area maps are used that is Map 5, 6 and 7.

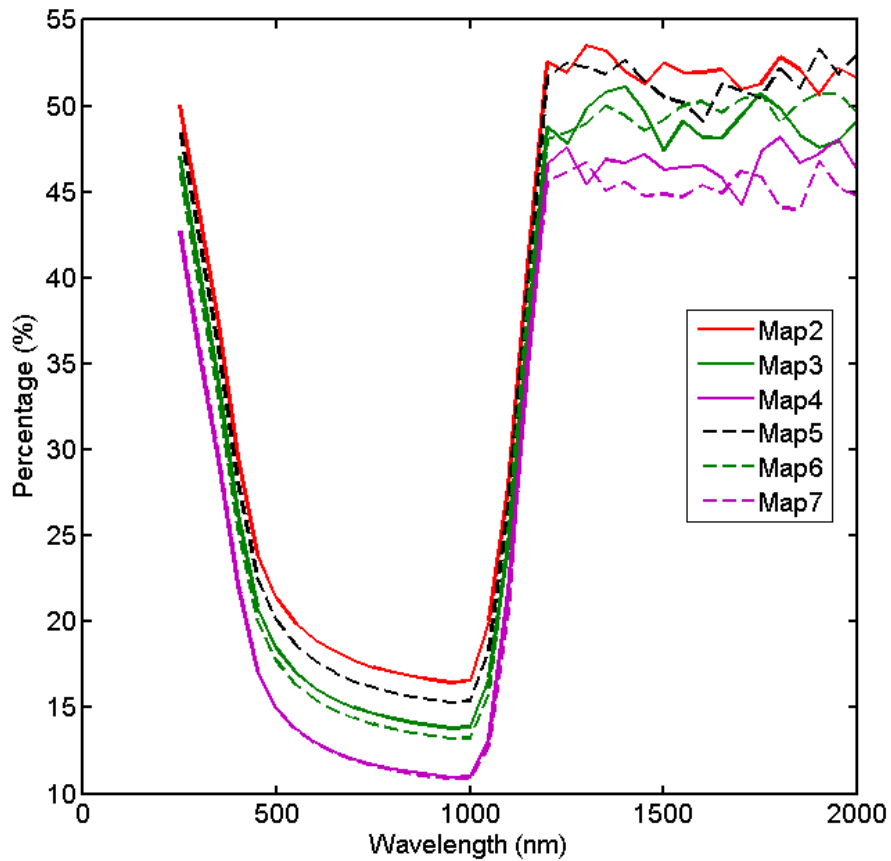


Figure 57 Total Reflection Calculated Using CROWM to Investigate the Effect of Area.

#### 4.5.2 Effect of Changing Base Angle and Its Distribution on Reflection, Transmission and Absorption (RTA) of the Maps

Map 1, 5, 6 and 7 have different base angle pyramids. While Map 8, 9 and 10 all have normal distribution of base angle and the distributions are centered at exactly the same angle as the base angle of Map 5, 6 and 7 respectively. The angular distribution of these maps is given in previous section in Fig. 53. The total reflection calculated by CROWM for these maps is given in Fig. 58.

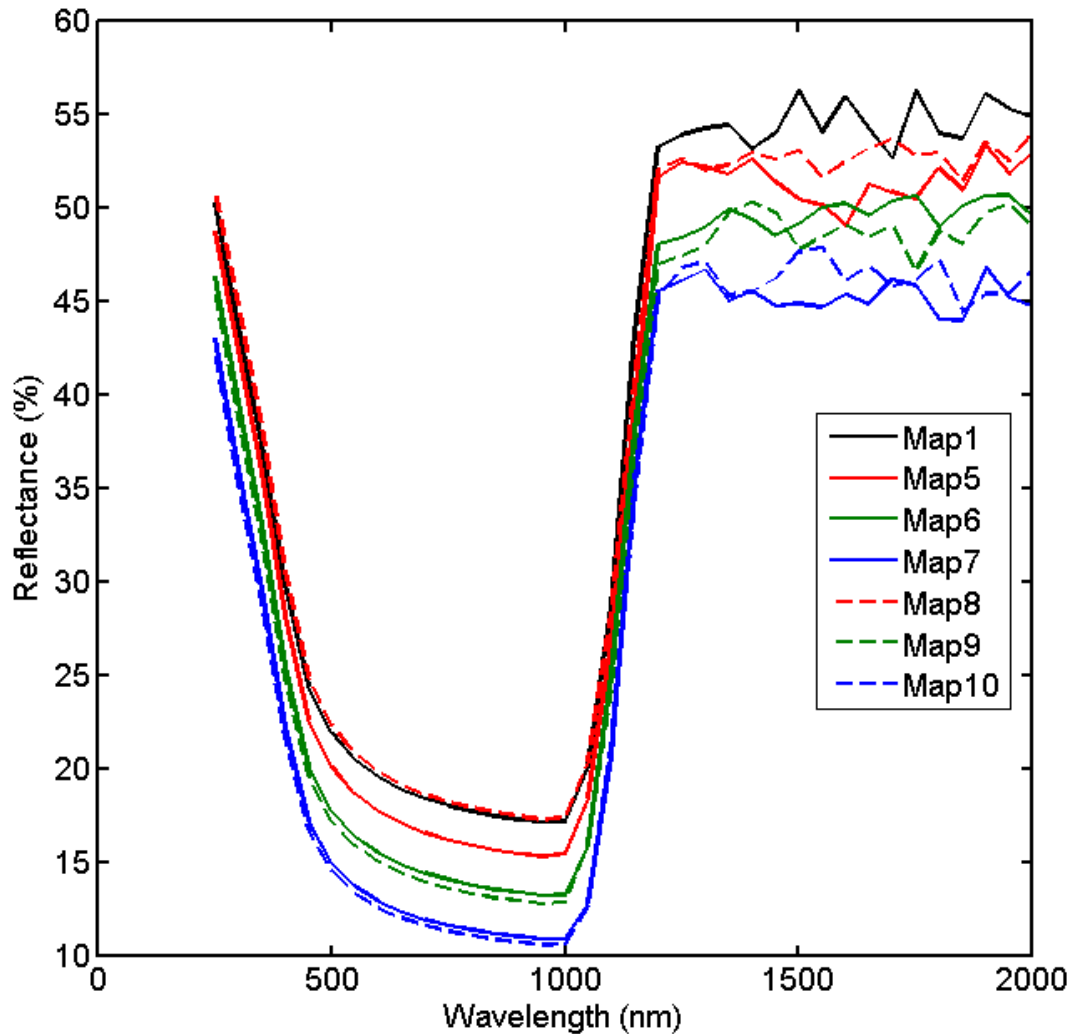


Figure 58 Reflection Distributions of Map1, Map5 - Map10.

Looking at reflection results shown in Fig. 58 it is concluded that increasing the base angle of pyramids decreases the reflection as it should since the light rays are reflected at steeper angles from the front surface and so have higher chance to

strike another pyramid and it could go on for multiple strikes, thus lowering the reflection. The decrease in reflection is proportional to the increase in base angle. It is found from the Fig. 58 that changing base angle from 50 degrees (Map6) to 54.7 degrees (Map7) results in decrease of about 2.39 % in reflection at 1000nm wavelength. And change in reflection per unit change in base angle is approximately equal to 0.48%.

The effect of having a normal distribution of base angles is that it lowers the reflection for the case of Map 6 – Map 9 and Map 7 – Map 10. It is observed broadening the distribution decreases the reflection and it makes sense because broadening means there are larger angles that are being included in the texture which decreases the reflection.

The transmittance and absorbance curves for each map are shown in Fig. 59.

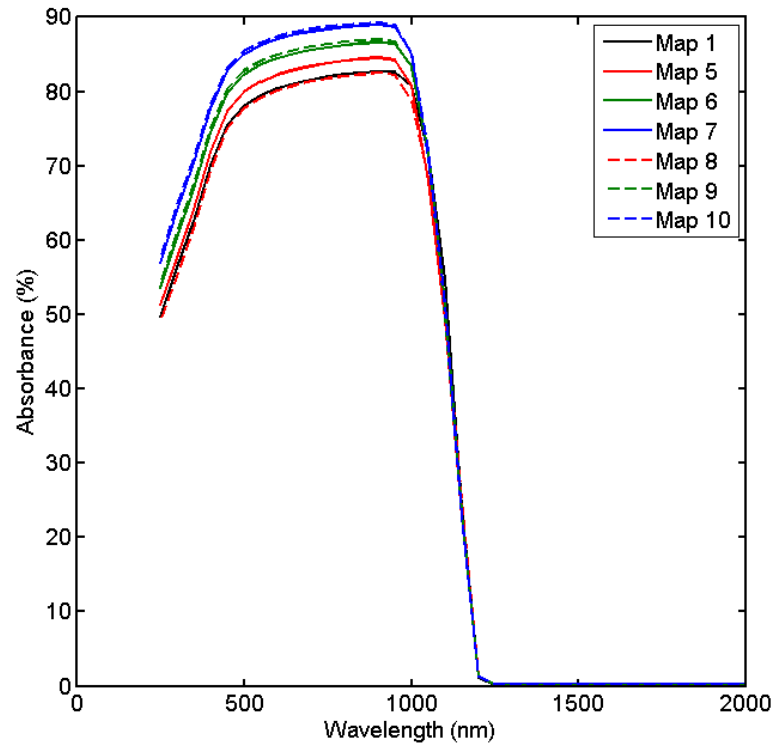
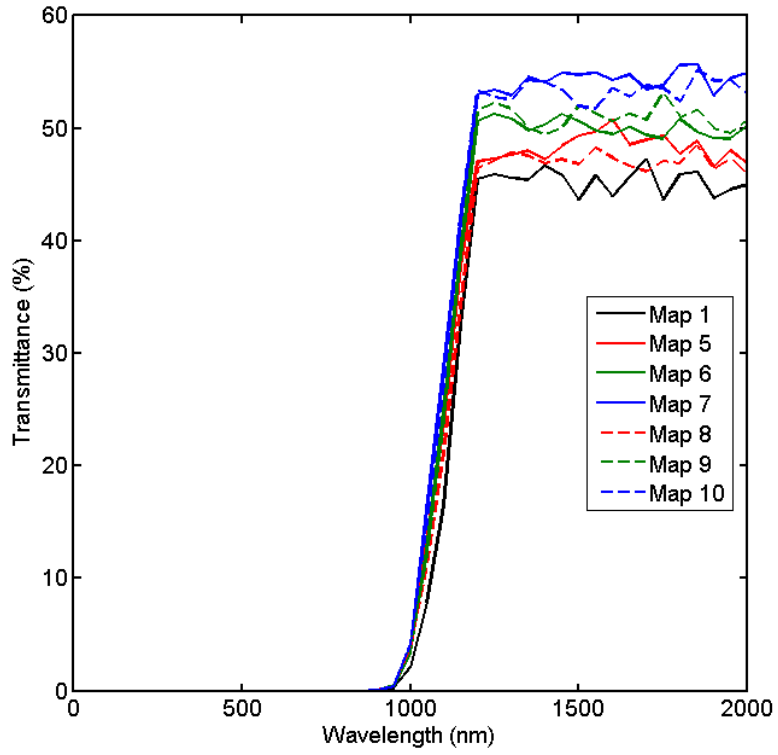


Figure 59 (Top) Shows the Transmittance of the Maps as Calculated by CROWM  
 (Bottom) Absorbance of the Maps Calculated by CROWM

### 4.5.3 Front Surface Reflectance Comparison - CROWM Versus OPAL2

To validate the front surface reflectance results obtained with CROWM ideally a comparison with a software of similar capabilities is desired. The closest is OPAL2 that is available online for use for free [18][19]. OPAL2 is capable of calculating front surface reflectance for regular and random upright pyramidal texture among other textures. It also allows for the change in base angle ( $\alpha_b$ ) of pyramids one of the things tried in modified maps. OPAL2 like CROWM relies on ray tracing when it comes to simulating random upright pyramids. But, one major difference is that OPAL2 first finds out the unique preferential paths the light rays take and then calculates the fraction of rays that follow each path and then using the approach described in [22] calculates the total reflection. Fig. 60 shows the comparison of front surface reflectance of OPAL2 versus CROWM for random upright pyramids for three different facet or base angles that is 45.54, 50, 54.7 degrees.

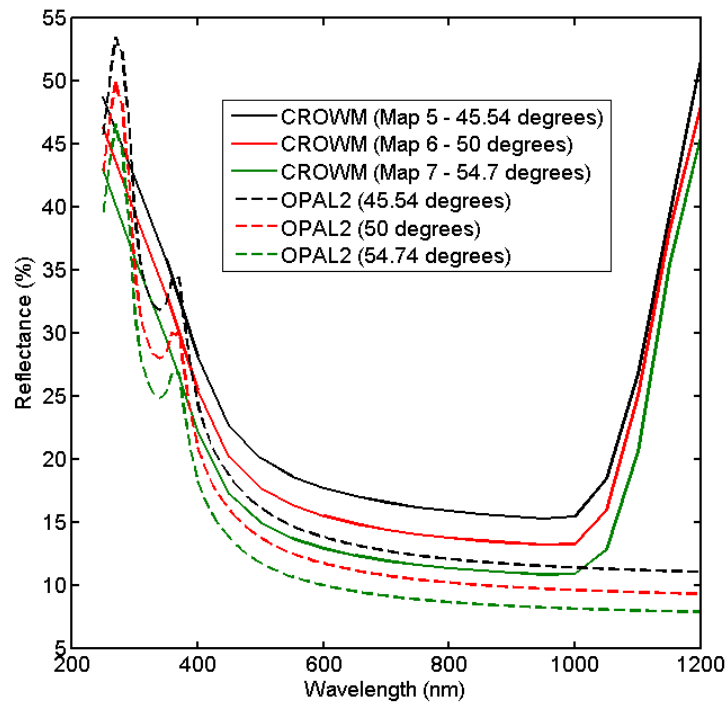


Figure 60 CROWM Versus OPAL2 Reflectance Comparison.

There is a noticeable difference in reflectance values for the same base angle pyramids between OPAL2 and CROWM. Table 5 shows the difference in reflectance values at 900 nm wavelength between the two.

Table 5 Difference in Reflectance Values at 900 nm, CROWM Versus OPAL2.

Facet/Base Angle ( $\alpha_b$ )	CROWM (%)	OPAL2 (%)	Difference (%)
45.54 degrees	15.44	11.67	3.71
50 degrees	13.36	9.839	3.521
54.7 degrees	10.99	8.334	2.656

It is also important to compare the reflectance of the actual textured wafer measured with spectrophotometer with the reflectance that CROWM gives for measured AFM map of the sample. The reflectance for these two case are plotted together with OPAL2 results in Fig. 61.

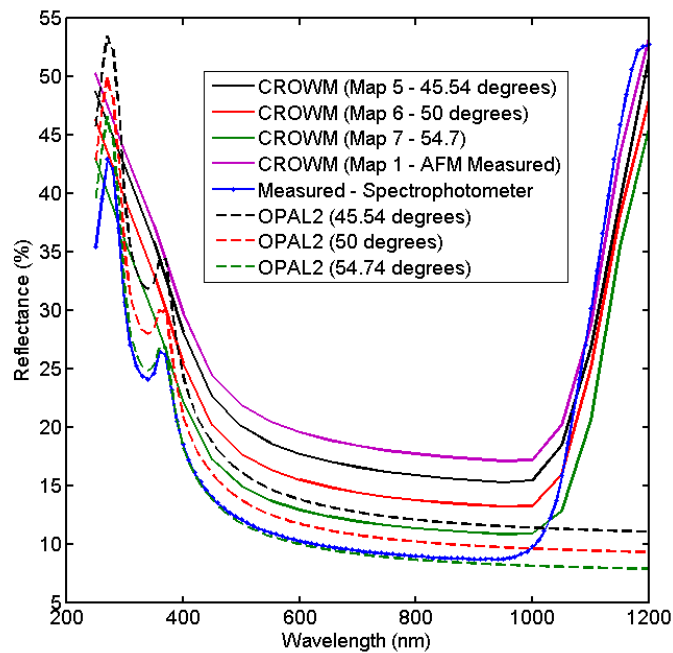


Figure 61 Reflectance Comparison of Actual Textured Wafer Obtained with Spectrophotometer with CROWM.

The difference in reflectance values at 900 nm between what CROWM gives for measured AFM map and measured reflectance with spectrophotometer is 8.56 % (17.27 – 8.71). For the measured AFM map the base angle distribution is centered at 45.54 degrees and if CROWM can match the reflectance with OPAL2 then the reflectance at 900 nm would be 11.67% (can be read from Table 5). With that the difference would just be 2.96% (11.67 – 8.71).

#### 4.5.4 Angular Transmittance Scattering from Front Surface into the Silicon

Angular transmittance scattering results were obtained using ray tracing with CROWM. For each map front surface angular resolved transmittance is calculated. It shows how the light scatters as it couples into silicon through the front surface. It has important consequence as it has direct consequence on light trapping inside the silicon. It is also important to understand because it could help in the design of back reflector. Fig. 62 illustrates the idea of angular resolved transmittance from front surface.

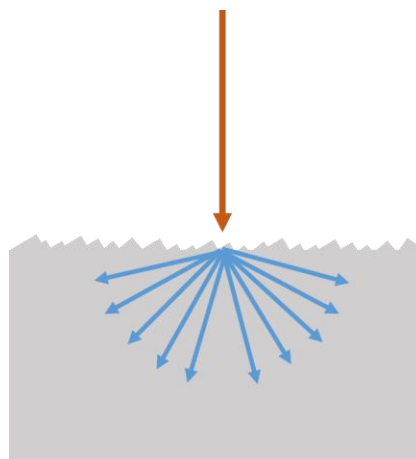


Figure 62 Shows what is meant by Angular Transmittance from Front Surface.

So, for this simulation a wavelength of 1200 nm is chosen. The structure is that we have 180 microns thick silicon and the maps act as a texture for front side and back side is flat and act as a perfect reflector (that is it has 100% reflectivity). The scattering distribution of light rays entering the silicon from front surface gives an idea how randomly the light rays are scattered. The more randomly they scatter more close the texture would be to lambertian scatterer. The angular scattering from lambertian scatterer could be approximated [39][40] using an Eq. 4.4.

$$ADF = \frac{1}{2} \cos \theta \quad \text{Eq. 4.4}$$

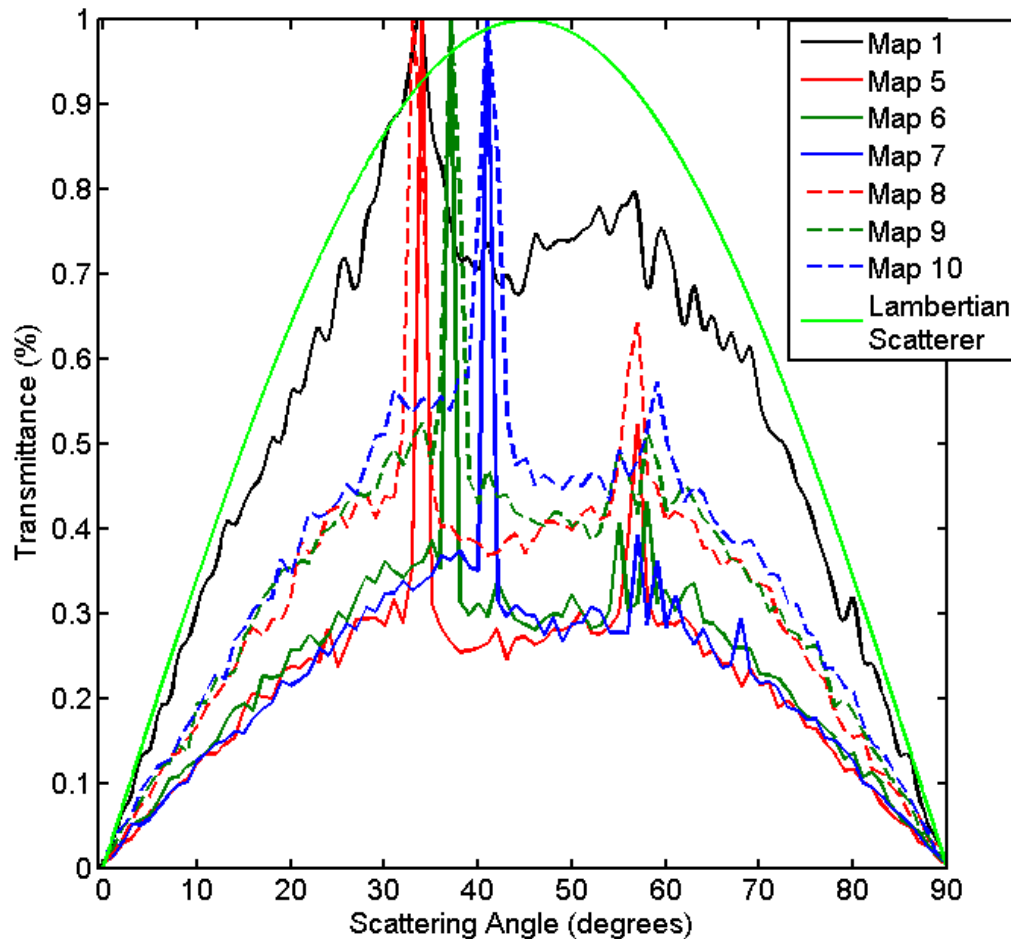


Figure 63 Angular Transmittance of Maps and Lambertian Scatterer at 1200 nm.

Fig. 63 shows the results obtained from CROWM. Map 1 scatters light closer to lambertian scatterer than any other map does. It is not surprising because the base angle distribution for Map 1 shows Gaussian distribution. It is an important result as it has direct impact on the absorbance of weakly absorbed light as would become evident in the next section.

#### 4.5.5 Comparison with Lambertian Scatterer

Throughout in this thesis the maximum effort is given to keep the positional randomness as accurate as possible to the real texture. First, by making sure that with AFM the measured map is error free. After, that in the modified maps the positions and heights of the pyramids were kept the same and just the base angles were changed. Angular changes were done in two ways; one keeping the base angle the same for all the pyramids in the map, second having an angular distribution of base angle and tried to achieve a Gaussian distribution. The first approach would afford the opportunity to investigate the effect of changing the base angle and second type of maps would allow to probe the effect of having an angular distribution of base angles on the light trapping ability of the texture.

Path length enhancement has been used in literature as a measure of texture's light trapping capacity. For comparison a worst case is defined that is the top surface is assumed to transmit normal incident light with 100% transmittance. The back surface is flat and act as perfect reflector, which reflects the light back to the top surface where it escapes the substrate, thus giving a path length of  $2W$  ( $W$  is the thickness of the substrate). The situation is depicted in Fig. 64. In case where there is a texture at the top surface the light rays take a longer path through the

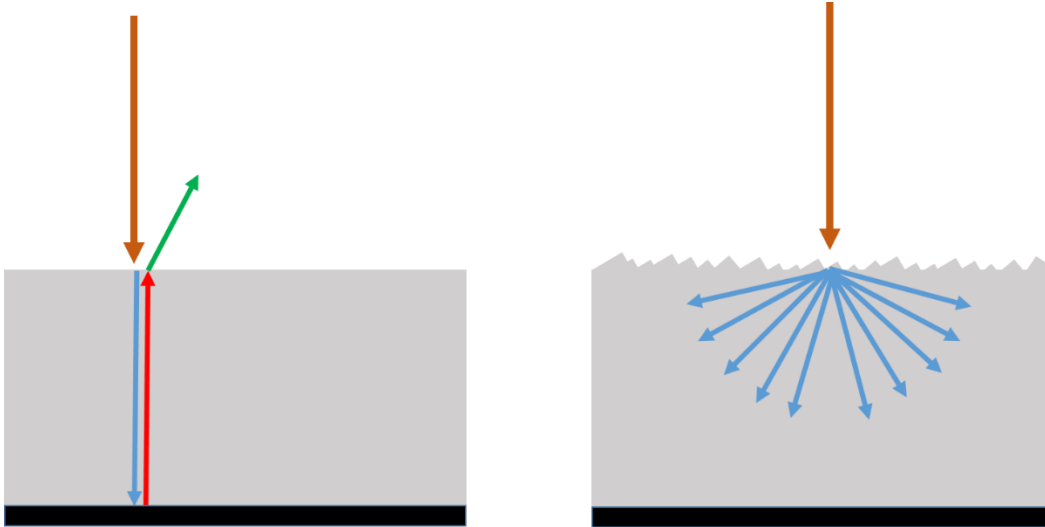


Figure 64 (Left) Shows the Worst Case where Substrate has no Texture at the Top (Right) Shows the Wafer has Texture at the Top. The Back Surface is a Perfect Reflector shown in Black.

substrate thus experiencing a path length enhancement and having a greater chance of getting absorbed. And after reflecting from the back reflector and reaching the top depending on local angle at the surface the rays either get totally internally reflected or escape out of the substrate if they fall within the escape cone. Fig. 65 shows if the pyramids are formed in such a way that their centers are in line, then the trapped ray after hitting the back surface has a greater chance to hit the top surface at the pyramid face that is opposite to the face from where it coupled in and fall within the escape cone. But, if the pyramids are positioned randomly so that their centers are not in line but randomly placed then the light ray has a higher probability of hitting the faces adjacent to the face where it got coupled in and wouldn't fall within the escape cone thus they would get internally reflected. So, having randomness in the positions of pyramids is essential for path length enhancement. Since, the texture considered in this work is produced with alkaline etching of silicon wafer and it results in a random texture. Therefore, it is of great interest to know its performance comparison with lambertian surface.

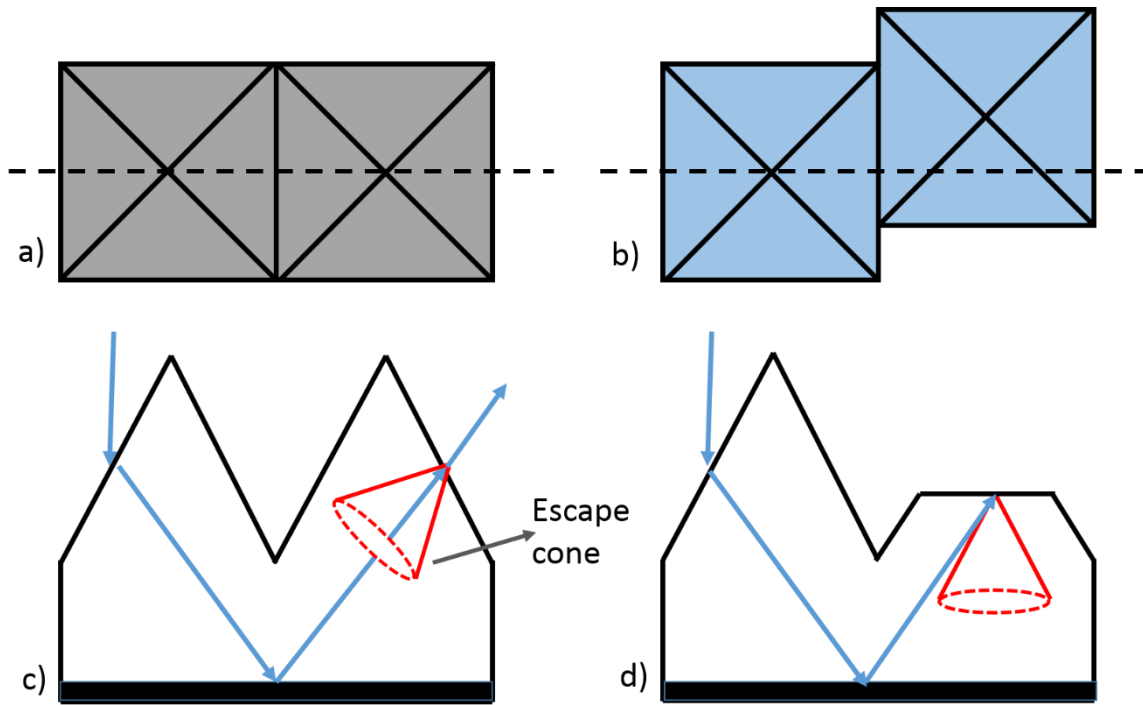


Figure 65 a) and b) Show Two Different Ways in which Pyramids could be formed on Silicon Surface. b) Shows the Pyramids are not in line as a) Thus having Positional Randomness. c) and d) Show the 2D View of a) and b) and Show how situation in b) increases the Chance of Total Internal Reflection, while in c) the Ray falls within the Escape Cone.

The structure assumed for this experiment is shown in Fig. 64. The flat case (worst case in terms of trapping) is compared to the maps for enhanced light trapping. First, the comparison is performed between the textures using path length as a metric. Essentially it is the absorbance of weakly absorbed light that reveals the lambertian behavior of a texture. The reflection losses, both front surface and intrinsic reflection are assumed to be zero. It means all the light is coupled into the substrate and only way of loss is then if the light rays escape the structure depicted in Fig. 64. In this way, the texture that is capable of trapping light better would keep the light inside the substrate by total internal reflection, hence the comparison would be just.

The chosen wavelength is 1200 nm as it is very weakly absorbed by silicon and normal incidence is assumed. At this wavelength silicon's absorption coefficient is  $2\text{m}^{-1}$ . The thickness of the wafer is 180 microns. The simulation included maps 1, 5, 6, 7, 8, 9, and 10. The results were obtained using CROWM.

Table 6 Path Length Enhancement Results from CROWM.

<b>Map</b>	<b>Path length (in terms of substrate thickness - W) (at <math>\lambda = 1200</math> nm)</b>
Map1	55.59
Map5	57.06
Map6	59.71
Map7	59.83
Map8	58.0581
Map9	57.20
Map10	59.11
Worst Case (Flat)	2

The path length enhancement result for flat case is twice the thickness of the wafer because top surface is assumed to have unit transmittance. Table 6 reveals that all the textures achieve greater path lengths than the lambertian surface (which would have a path length enhancement of 49). It is not too surprising to see that the textures perform better than lambertian surface as already in literature [24][20] it

has been shown even with periodic feature as well as using computer generated random pyramidal texture that path length enhancement better or close to lambertian is achievable. But, it is for the first time that the path length enhancement is measured with an actual texture obtained with alkaline etching. The reason the textures achieve better average path lengths could be attributed to the fact that these textures can randomize light rays as they couple in to the substrate very well and therefore the rays escaping through the front surface after first and second reflection from the back reflector is greatly reduced. Furthermore, it has been shown by Campbell et al. in [10] that under normal incidence with increasing number of passes even the regular texture starts to randomize rays better than lambertian scatterer. But in the same paper [10] and [14] it is shown that when the light has non-normal incidence it doesn't always exceed lambertian limit. Therefore, further examination is needed under isotropic illumination and non-normal incidence to justly compare these textures and lambertian scatterer.

There are some important lessons that could be inferred from these results. Although, all of these textures have performed really close in terms of path length enhancement at normal incidence of 1200 nm light, but Map 6 and 7 are highest. Map 6 has all the pyramids at base angle of 50 degrees and Map 7 has pyramids at 54.7 degrees. And large base angle pyramid transmits the light inside substrate at larger angle therefore longer the path of rays. And once the light enters the substrate the random position of pyramids ensures the internal reflection. Thus, it is concluded that having a large base angle is needed for long path lengths.

Another important thing to notice in Table 6 is that path lengths for Map 9 and 10 decrease from their corresponding Map 6 and 7. It is concluded that since in

Map 9 and 10 pyramids have Gaussian distribution centered around 50 degrees and 54.7 degrees respectively, it introduces small base angle pyramids which reduce the initial transmittance angle into the substrate thus reducing the path length.

Therefore, it is concluded that having a distribution of base angles doesn't necessarily help in lengthening the path lengths. But, overall there is not a drastic change in path lengths for all of the maps therefore, it is concluded the positional randomness is the most important factor to get long path lengths.

For a complete picture of behavior of these textures it is important to look at their response for the whole solar spectrum, especially for intermediately absorbed light below 1200 nm till 1000 nm. The  $4n^2$  limit that is applied to weakly absorbed light is not a very good approximation for intermediately absorbed light for lambertian scatterer. This is so because the material is absorbing in this regime and  $4n^2$  is an upper limit on absorption that can never be reached. But, for comparison purposes it is included in this work. The absorbance with  $4n^2$  path length enhancement is given by Eq. 4.5.

$$A = 1 - e^{-4n^2\alpha_a W} \quad \text{Eq. 4.5}$$

In this work limit of absorption due to  $4n^2$  is referred to as LLY (lambertian limit by Yablonovitch).

There are numerous approximations for lambertian limit for light trapping that are applicable not just to weakly absorbed light but also to intermediately absorbed light [41][42][43][44]. For this work the approximation presented by Deckman et al. in [41] is adopted. It has been mentioned before in Eq. 2.7. Absorbance according to [41] is given by,

$$A = \frac{1 - e^{-4\alpha_a W}}{1 - e^{-4\alpha_a l} + \frac{e^{-4\alpha_a W}}{n^2}}$$

For further analysis this approximation is used and referred in this work as LLD (Lambertian Limit by Deckman et al.). Same setup is used as depicted in Fig. 63 and also the assumptions stay the same.

Map 7 is chosen as a representative of modified maps (only one is chosen to avoid cluttering on the plot). The thickness of the wafer is 180 microns. The results were obtained using CROWM as shown in Fig. 66.

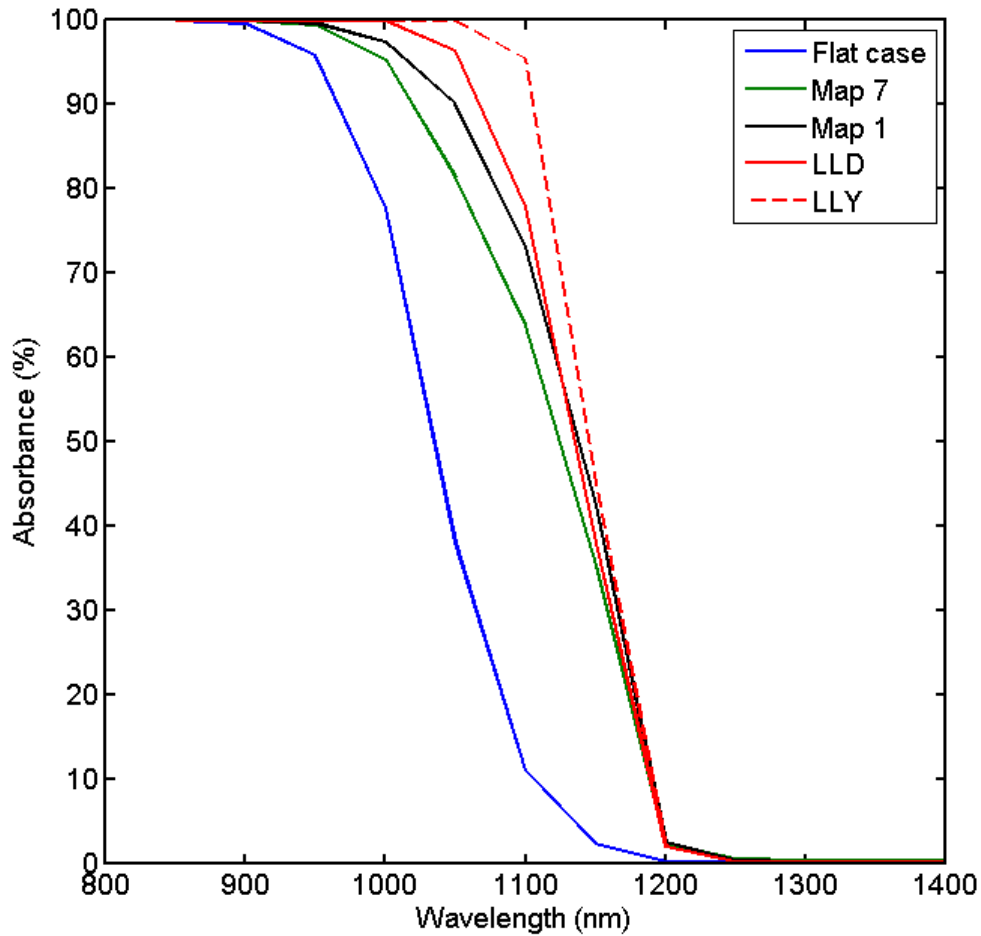


Figure 66 Comparison of Absorbance of Flat Case, Lambertian, Measured AFM Map And Modified Maps.

Fig. 67 shows the absorbance for all the maps.

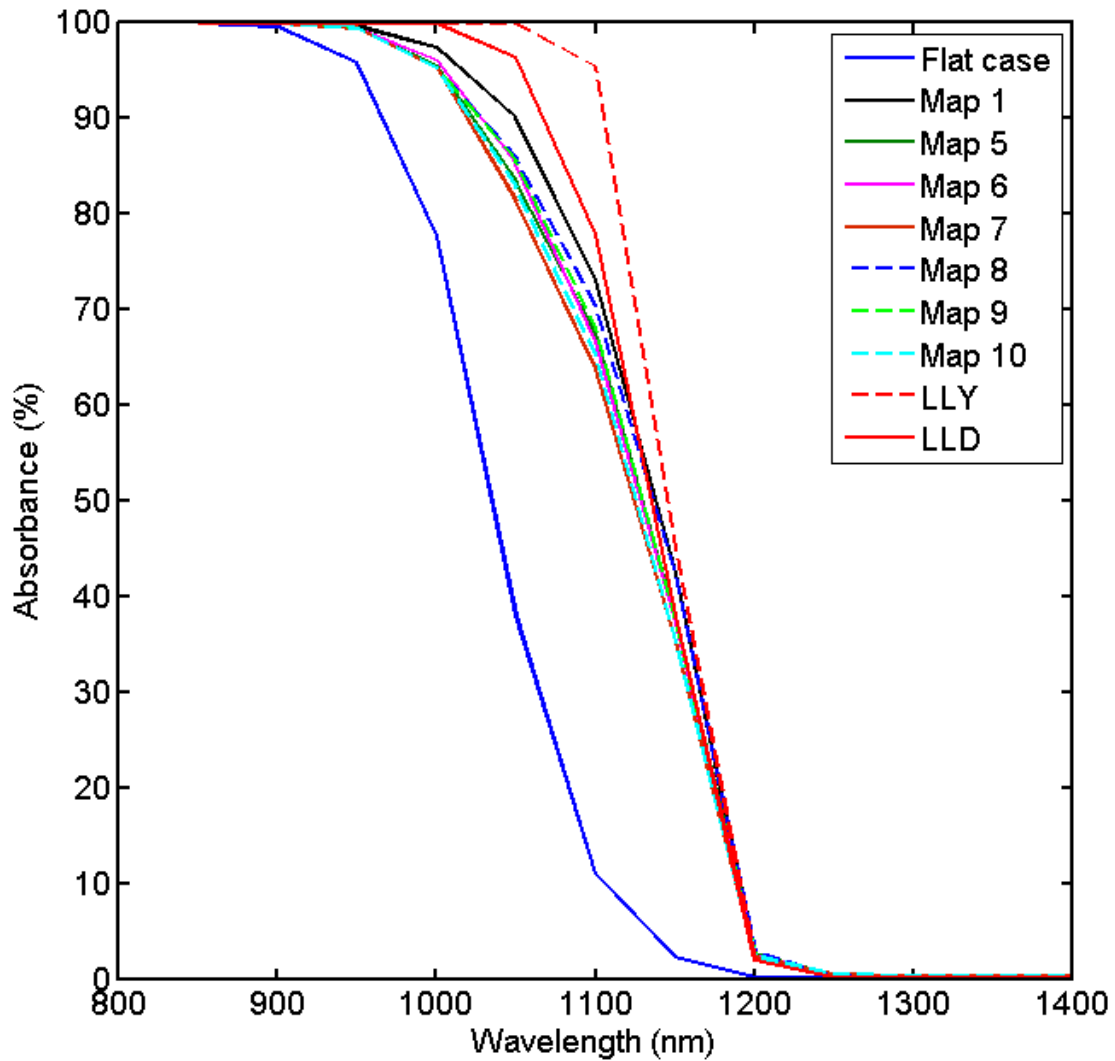


Figure 67 Absorbance for All the Maps.

From Fig. 66 and 67 the trend is clear, away from the band edge of silicon in the weak absorbing regime (beyond 1150 nm wavelength) the textures perform equally well as lambertian limit LLD and almost as good as LLY but in the intermediate absorbing (less than 1150 nm wavelength) regime the textures perform poor than LLD and LLY. It should be noted these results are only true for normal

incidence of light and can't be generalized for non-normal incidence. The trend can be explained in terms of randomization that rays experience due to texture. Since, in the weak absorbing regime the rays don't get absorbed immediately, so the textures have chance to randomize the rays better than lambertian scatterer and therefore, absorb them equally good. While on the other hand in intermediate absorbing regime the ratio of rays that escape to those absorbed is greater for the textures than for lambertian scatterer. It is because textures can't randomize the rays as quickly and as much as lambertian and therefore, the loss due to transmission of rays out of the front surface is greater for the textures being tested.

Second best is Map 1 which is a measured AFM map. It is concluded since it has a large variation in base angle ( $\alpha_b$ ) distribution so it leads to better randomization of light rays inside the silicon as concluded from its angular resolved transmittance curve in Fig. 63, thus reducing the escape of rays. Similarly, Map 9 and 8 outperform the rest of the maps clearly showing the variation in base angle distribution leads to randomization of light rays inside the silicon which leads to better absorbance.

Another important metric for comparison of light trapping is short circuit current density. During this calculation black body radiation is assumed, unity internal quantum efficiency is assumed and as already mentioned zero reflection loss is assumed that means all the light gets coupled into the substrate and also there is no loss when light bounces around inside the substrate. Therefore, we can use the absorbance curves given in Fig. 67 to calculate the short circuit current density. It can be calculated using Eq. 4.6.

$$J_{sc} = e \int_{E_g}^{\infty} A(E) \frac{dN}{dE} dE \quad \text{Eq. 4.6}$$

Here A(E) is the absorbance curve, N is the photon flux and  $E_g$  is the bandgap. For photon flux the spectrum AM 1.5 given in [45] is assumed. The range of wavelength considered is from 300 nm to 2000 nm.

Short circuit current for each map is calculated separately and also calculated relative to the flat case. It means flat case short circuit current is assumed to be zero and for the rest of the maps current values are measured using this as a reference.

Table 7 shows the results.

Table 7 Short Circuit Current values for the Maps.

Map	Short circuit current, $J_{sc}$ (mA/cm <sup>2</sup> ) ( $\lambda = 300$ nm – 2000 nm) (AM 1.5)	Short circuit current, $J_{sc}$ (relative to flat case) (mA/cm <sup>2</sup> )
LLY	44.47	4.50
LLD	43.95	4.07
Map 1	43.69	3.81
Map5	43.29	3.41
Map 6	43.34	3.46
Map 7	43.16	3.28
Map 8	43.47	3.59
Map 9	43.36	3.48
Map 10	43.22	3.34
Flat case	39.88	0

## CHAPTER 5

### CONCLUSION

#### 5.1 Summary

In this work the focus was to investigate the true light trapping capability of an actual texture obtained with alkaline etching. For this purpose an AFM map of the surface of textured silicon wafer was obtained with emphasis to capture the positional randomness, true heights and base angles of pyramids as accurately as possible. To validate the accuracy of AFM map it is matched for peak density with SEM micrograph of the texture. Further validation is done by matching base angle obtained from angular resolved reflectance curve of actual texture with base angle obtained with AFM. And the last method of validation was to use Focused Ion Beam to mill the pyramids and obtained base angle distribution from there. So, with this an actual random pyramidal map was obtained. Later, to investigate the effect of changing base angle or having a distribution of base angle on light trapping the actual map is modified. During the process of modification the positions and height of pyramids are kept the same only the base angles are changed.

The simulation results show that the base angles effect the front surface total reflectance strongly. Higher base angles give lower reflectance. It means high base angle pyramids couple the light more effectively into the substrate. It is because the higher the base angle more bounces the ray would have between pyramids before escaping the surface. Thus, light has greater chance of coupling into the substrate. It is estimated that reflectance changes about 0.48% per unit change in base angle.

Having a broad distribution of base angle slightly reduced the reflection because it introduced pyramids with smaller base angles.

From the angular transmittance results in Fig. 62 it becomes evident that the measured AFM Map 1 scatters light better than any of the modified maps. It is close to lambertian scatterer in terms of scattering but still randomization of light is less than lambertian. This becomes clear from absorbance curves plotted in Fig. 66 where zero reflection losses were assumed. Map 1 shows the highest absorbance after lambertian scatterer than any other modified texture. It is estimated that lambertian scatterer with LLD limit produces  $4.07 \text{ mA/cm}^2$  more than the flat case and with LLY limit produces  $4.50 \text{ mA/cm}^2$  more than the flat case and measured AFM Map 1 produces  $3.81 \text{ mA/cm}^2$  more (assumption is that all the light gets coupled into the substrate) for normal incidence of light. Furthermore, as we move into the weak absorbing regime under normal incidence, the maps absorb as good as lambertian limit defined by Deckman et al. and Yablonovitch. Before, that in intermediate absorbing regime the maps absorb poorly than lambertian limits LLD and LLY. It is emphasized that the path length results are obtained for normal incidence of light at 1200 nm wavelength, where it seems the textures outperform the lambertian scatterer but these structures have not been tested for isotropic illumination or for light of non-normal angle of incidences. In [10][14] it has been shown that pyramidal textures under normal incidence are capable of lambertian scattering but fail to achieve it for all the non-normal incidence cases. Therefore, there is a need for further investigation for path length enhancement under isotropic illumination and using various angle of incidence for complete comparison between these textures and lambertian scatterer.

Map 1 shows poor front surface reflection but yet achieves good light trapping as evident from its absorbance comparison, so it is concluded to have over all best performance across the whole of spectrum it is essential to have good light coupling as well as good light trapping texture in order to reach the lambertian limit and Shockley-Queisser limit [3].

## 5.2 Future Work

Future work would be to evaluate the performance of these maps for various non-normal incidence of light and also under isotropic illumination. Further work is needed to optimize these textures for lower front reflection for efficient light coupling by changing height distribution and applying background texturing schemes to achieve lambertian limit as well as Shockley-Queisser limit.

## REFERENCES

- [1] <http://www.eia.gov/forecasts/ieo/world.cfm>
- [2] [http://www.eia.gov/forecasts/aeo/pdf/0383\(2014\).pdf](http://www.eia.gov/forecasts/aeo/pdf/0383(2014).pdf)
- [3] Shockley, William, and Hans J. Queisser. "Detailed balance limit of efficiency of p-n junction solar cells." *Journal of applied physics* 32.3 (1961): 510-519.
- [4] <http://www.ise.fraunhofer.de/en/renewable-energy-data>.
- [5] <http://www.greentechmedia.com/articles/read/top-chinese-manufacturers-will-produce-solar-panels-for-42-cents-a-wat>
- [6] [http://commons.wikimedia.org/wiki/File:Solar\\_Spectrum.png](http://commons.wikimedia.org/wiki/File:Solar_Spectrum.png)
- [7] De Vos, Alexis. *Thermodynamics of solar energy conversion*. John Wiley & Sons, 2008.
- [8] <http://pveducation.org/pvcdrom/pn-junction/absorption-coefficient>
- [9] Yablonovitch, Eli. "Statistical ray optics." *JOSA* 72.7 (1982): 899-907.
- [10] Campbell, Patrick, and Martin A. Green. "Light trapping properties of pyramidally textured surfaces." *Journal of Applied Physics* 62.1 (1987): 243-249.
- [11] Cotter, J. E. "RaySim 6.0: a free geometrical ray tracing program for silicon solar cells." *Photovoltaic Specialists Conference, 2005. Conference Record of the Thirty-first IEEE*. IEEE, 2005.
- [12] Smith, A. W., A. Rohatgi, and S. C. Neel. "Texture: a ray tracing program for the photovoltaic community." *Photovoltaic Specialists Conference, 1990., Conference Record of the Twenty First IEEE*. IEEE, 1990.
- [13] Brendel, R. "Sunrays: a versatile ray tracing program for the photovoltaic community." *Proceedings of the 12th European Photovoltaic Solar Energy Conference*. Vol. 1994. 1994.
- [14] Brendel, R. "Coupling of light into mechanically textured silicon solar cells: A ray tracing study." *Progress in Photovoltaics: Research and Applications* 3.1 (1995): 25-38.
- [15] Rodriguez, J. M., I. Tobias, and A. Luque. "Random pyramidal texture modelling." *Solar Energy Materials and Solar Cells* 45.3 (1997): 241-253.

- [16] Baker-Finch, Simeon C., and Keith R. McIntosh. "Reflection of normally incident light from silicon solar cells with pyramidal texture." *Progress in Photovoltaics: Research and Applications* 19.4 (2011): 406-416.
- [17] Yun, Garam, Karlton Crabtree, and Russell A. Chipman. "Properties of the polarization ray tracing matrix." *Optical Engineering+ Applications*. International Society for Optics and Photonics, 2007.
- [18] Baker-Finch and K.R. McIntosh, "A freeware program for precise optical analysis of the front surface of a solar cell," 35th IEEE Photovoltaic Specialists Conference, Honolulu, pp. 2184–2187, 2010.
- [19] K. R. McIntosh and S.C. Baker-Finch, "OPAL 2: Rapid optical simulation of silicon solar cells," Proceedings of the 38th IEEE Photovoltaic Specialists Conference, Austin, in-press, 2012.
- [20] Taylor, Jeffrey L. "Reflectance Measurements of Materials Used in the Solar Industry." *PerkinElmer Technical Note* (2009).
- [21] Van Nijnatten, P. A. "An automated directional reflectance/transmittance analyser for coating analysis." *Thin Solid Films* 442.1 (2003): 74-79.
- [22] Baker-Finch, Simeon C., and Keith R. McIntosh. "Reflection distributions of textured monocrystalline silicon: implications for silicon solar cells." *Progress in Photovoltaics: Research and Applications* 21.5 (2013): 960-971.
- [23] Yang, Yang. *Light Management for High Efficiency Silicon Solar Cells*. Diss. The University of New South Wales, 2012.
- [24] Martin, Y., C. C. Williams, and H. Kumar Wickramasinghe. "Atomic force microscope–force mapping and profiling on a sub 100-Å scale." *Journal of Applied Physics* 61.10 (1987): 4723-4729.
- [25] Notebook, Scanning Probe Microscopy Training. "Version 3.0." *Digital Instruments, Veeco Metrology Group* (2000).
- [26] [http://lben.epfl.ch/files/content/sites/lben/files/ABML%20%20AFM%20module%20-%20on%20templ\\_rev1h.pdf](http://lben.epfl.ch/files/content/sites/lben/files/ABML%20%20AFM%20module%20-%20on%20templ_rev1h.pdf)
- [27] Yacoot, Andrew, and Ludger Koenders. "TOPICAL REVIEW: Aspects of scanning force microscope probes and their effects on dimensional measurement." *Journal of Physics D Applied Physics* 41.10 (2008): 3001.
- [28] Kizuka, Tokushi, and Kazue Hosoki. "In situ high-resolution transmission electron microscopy of direct bonding processes between silicon tips with oxide surfaces at room temperature." *Applied physics letters* 75.18 (1999): 2743-2745.

- [29] Prater, C. B., et al. "Tappingmode imaging applications and technology." *Digital Instruments Nanonotes, Santa Barbara, California, USA* (1995).
- [30] West, Paul E. *Introduction to atomic force microscopy: Theory, practice, applications*. Pacific Nanotechnology, 2007.
- [31] Gibson, C. T., G. S. Watson, and S. Myhra. "Scanning force microscopy—calibrative procedures for 'best practice'." *Scanning* 19.8 (1997): 564-581.
- [32] <http://www.nanoandmore.com/USA/home.php>
- [33] <https://www.brukerafmprobes.com/>
- [34] <http://kteknano.com/>
- [35] <http://gwyddion.net/>
- [36] Lipovšek, Benjamin, Janez Krč, and Marko Topič. "Optical model for thin-film photovoltaic devices with large surface textures at the front side." *Informacije Midem* 41.4 (2011): 264-271.
- [37] Holman, Zachary C., et al. "Infrared light management in high-efficiency silicon heterojunction and rear-passivated solar cells." *Journal of Applied Physics* 113.1 (2013): 013107.
- [38] Holman, Zachary C., et al. "Parasitic absorption in the rear reflector of a silicon solar cell: simulation and measurement of the sub-bandgap reflectance for common dielectric/metal reflectors." *Solar Energy Materials and Solar Cells* 120 (2014): 426-430.
- [39] Andreani, L., et al. "Towards the lambertian limit in thin film silicon solar cells with photonic structures." *27th European Photovoltaic Solar Energy Conference and Exhibition: Material Studies, New Concepts and Ultra-High Efficiency Fundamental Material Studies*. 2012.
- [40] Battaglia, Corsin, et al. "Light trapping in solar cells: When does a Lambertian scatterer scatter Lambertianly?." *Journal of Applied Physics* 112.9 (2012): 094504.
- [41] Deckman, H. W., et al. "Optically enhanced amorphous silicon solar cells." *Applied Physics Letters* 42.11 (1983): 968-970.
- [42] Deckman, H. W., C. B. Roxlo, and E. Yablonovitch. "Maximum statistical increase of optical absorption in textured semiconductor films." *Optics letters* 8.9 (1983): 491-493.
- [43] Green, Martin A. "Lambertian light trapping in textured solar cells and light-emitting diodes: analytical solutions." *Progress in Photovoltaics: Research and Applications* 10.4 (2002): 235-241.

[44] Bozzola, Angelo, Marco Liscidini, and Lucio Claudio Andreani. "Photonic light-trapping versus Lambertian limits in thin film silicon solar cells with 1D and 2D periodic patterns." *Optics express* 20.102 (2012): A224-A244.

[45] Gueymard, Christian. *SMARTS2: a simple model of the atmospheric radiative transfer of sunshine: algorithms and performance assessment*. Cocoa, FL: Florida Solar Energy Center, 1995.

APPENDIX A

MAPS

